Waterbelt scenario for the Cryogenian glaciations questioned by uncertain mixed-phase clouds

Zur Erlangung des akademischen Grades eines
DOKTORS DER NATURWISSENSCHAFTEN
von der KIT-Fakultät für Physik des
Karlsruher Instituts für Technologie (KIT)

angenommene

DISSERTATION

von

M. Sc. Christoph Braun
aus Buchheim

Tag der mündlichen Prüfung:	20. Mai 2022
Referent:	Prof. Dr. Joaquim Pinto
Korreferent:	Prof. Dr. Aiko Voigt

Abstract

Geological evidence of active tropical glaciers reaching sea level during the Cryogenian (720 - 635 Million years ago), suggesting a global ocean completely covered in ice, was the key observation in the development of the hard Snowball Earth hypothesis. These conditions are hard to reconcile with the survival of complex marine life through Snowball Earth glaciations, which led to alternative waterbelt scenarios where a large-scale refugium was present in the form of a narrow ice-free strip in the tropical ocean. Among the proposed waterbelt scenarios, the so-called Jormungand hypothesis is particularly attractive as it proposes an entire life cycle of the glaciations and rests on well-established atmospheric dynamics and physics. According to the Jormungand hypothesis, the waterbelt climate is stabilized by a weakening of the ice-albedo feedback in the subtropical region. In the subtropics, subsidence associated with the Hadley circulation suppresses precipitation and promotes evaporation of high-albedo snow deposited on sea ice. Hence, subtropical sea ice is snow-free and relatively dark. We here investigate whether a Jormungand-waterbelt scenario is a viable explanation for the Cryogenian glaciations.

In a first step we investigate whether Jormungand-waterbelt states are a robust feature of Earth's past climate using idealized aquaplanet simulations from two climate models run with a variety of cloud treatments in combination with an energy balance model. Our simulations show that geologically relevant waterbelt states are not a robust and naturally emerging feature of climate. Intense shortwave reflectivity by mixed-phase clouds, in addition to a low albedo of bare sea ice, is needed for geologically-relevant waterbelt states. However, the high uncertainty associated with representing mixed-phase clouds in general circulation models prohibits us to assess whether shortwave cloud reflectivity was high and thus whether a waterbelt climate prevailed during the Cryogenian period.

The uncertainty associated with representing clouds in general circulation models was shown to primarily arise from convection parameterizations and aerosol-cloud interactions. Therefore, in a second step, we investigate whether reducing the required model assumptions associated with the treatment of convection in atmospheric models helps us to assess the plausibility of a waterbelt scenario. First, we show that unresolved sub-grid scale processes generate substantial differences in Cryogenian subtropical cloud reflectivity among general circulation models. Second, we conduct a hierarchy of simulations using the ICOsahedral Nonhydrostatic (ICON) modeling framework, ranging from coarse-scale general circulation model simulations to large-eddy simulations that explicitly resolve atmospheric convective-scale motions. Our hierarchy of simulations supports the existence of highly reflective subtropical clouds if we apply moderate ice nucleating particle concentrations. Third, we test the sensitivity of cloud reflectivity to the abundance of ice nucleating particles. In the presence of high but justifiable ice nucleating

particle concentrations, cloud reflectivity is strongly reduced. Hence, the existence of stable waterbelt states does critically depend on the abundance of ice nucleating particles. We conclude that explicitly resolving convection can help to constrain Cryogenian cloud reflectivity, but limited knowledge concerning Cryogenian aerosol conditions hampers strong constraints.

Overall, given the large uncertainty in mixed-phase clouds and their interaction with radiation, waterbelt states remain an uncertain feature of Earth's climate. Our results strongly question the idea that waterbelt scenarios can explain the Cryogenian geology. Thus, we conclude that Cryogenian life likely faced the harsh conditions of a hard Snowball Earth.

Zusammenfassung

Geologische Funde deuten auf Gletscher hin, die im Kryogenium (vor 720 - 635 Millionen Jahren) in den tropischen Ozean flossen. Diese Funde werden klassischerweise durch die Schneeball-Erde Hypothese erklärt, in welcher ein vollständig mit Eis bedeckter Ozean angenommen wird. Es ist jedoch schwierig, diese Bedingungen mit fossilen Funden in Einklang zu bringen, welche auf das Überdauern komplexer mariner Lebewesen während der Eiszeiten im Kryogenium hindeuten. Daher wurden alternative Szenarien vorgeschlagen, die ein großflächiges Refugium in Form eines eisfreien Wassergürtels im tropischen Ozean beinhalten. Ein besonders attraktives Szenario mit einem Wassergürtel-Klimazustand ist die sogenannte Jormungand-Hypothese, da sie einen umfassenden Lebenszyklus für den Ablauf der Eiszeiten vorschlägt und auf gut verstandenen atmosphärischen Prozessen beruht. Der Jormungand-Hypothese zufolge wird das Klima im Wassergürtel-Zustand durch eine Abschwächung des Eis-Albedo-Feedbacks in den Subtropen stabilisiert. In den Subtropen sind die Niederschlagsraten an der Erdoberfläche aufgrund der Hadley-Zirkulation geringer als die Verdunstungsraten. In Summe führt das zur Verdunstung von Schnee, der sich zuvor auf Meereis abgelagert hat. Daher ist das Meereis in den Subtropen schneefrei. Im Gegensatz zu Schnee, der eine hohe Albedo aufweist, ist schneefreies, blankes Meereis relativ dunkel. In dieser Arbeit untersuchen wir, ob ein auf der Jormungand-Hypothese basierendes Wassergürtel-Szenario sich als mögliche Erklärung für die Eiszeiten des Kryogeniums eignet.

Wir untersuchen zunächst, ob auf der Jormungand-Hypothese basierende Wassergürtel-Zustände eine robuste Eigenschaft des Klimas der Erde sind. Hierzu führen wir idealisierte Simulationen mit zwei Klimamodellen durch, die einen Wasserplaneten repräsentieren. Zusätzlich führen wir Simulationen mit modifizierten Eigenschaften der simulierten Wolken durch. Wir interpretieren die Ergebnisse aus den Klimamodellen mit einem eindimensionalen Energiebilanzmodell. Unsere Simulationen zeigen, dass geologisch relevante Wassergürtel-Zustände keine robuste Eigenschaft des Klimas sind. Damit Wassergürtel-Zustände geologisch relevant sind, ist es notwendig, dass in den Subtropen neben schneefreiem Meereis mit einer niedrigen Albedo Mischphasen-Wolken existieren, die viel solare Einstrahlung reflektieren. Weiterhin zeigen unsere Ergebnisse, dass die hohe Unsicherheit, die mit der Abbildung von Mischphasen-Wolken in Klimamodellen verbunden ist, eine Beurteilung verhindert, ob die Mischphasen-Wolken tatsächlich viel solare Einstrahlung reflektiert haben und damit auch, ob die Erde während des Kryogeniums in einem Wassergürtel-Zustand war.

Es ist weithin bekannt, dass die Unsicherheit, die mit der Abbildung von Wolken in Klimamodellen verbunden ist, hauptsächlich aus den Parametrisierungen für Konvektion und Aerosol-Wolken-Wechselwirkungen resultiert. Daher untersuchen wir in einem zweiten Schritt, ob die Reduktion der

erforderlichen Modellannahmen für die Abbildung von Konvektion in atmosphärischen Modellen uns hilft, die Plausibilität eines Wassergürtel-Szenarios zu beurteilen. Wir gehen hierbei in drei Schritten vor.
1) Wir zeigen, dass in Klimamodellen nicht explizit aufgelöste Prozesse einen erheblichen Einfluss darauf haben, wie viel solare Einstrahlung durch Mischphasen-Wolken in Wassergürtel-Zustand reflektiert wird.
2) Wir führen eine Reihe von Simulationen mit dem Atmosphärenmodell ICOsahedral Nonhydrostatic (ICON) durch, die von Simulationen mit grobskaligen Klimamodellen bis hin zu Large-Eddy-Simulationen reichen, welche die atmosphärische Konvektion explizit auflösen. Wir verwenden für diese Simulationen moderate Konzentrationen von Aerosolpartikeln, die als Eiskeime fungieren können. Diese Simulationen deuten darauf hin, dass stark reflektierende Wolken in den Subtropen während des Kryogeniums existiert haben können.
3) Wir testen, wie stark sich die Reflektivität der Wolken ändert, wenn wir die Konzentration an Aerosolpartikeln, die Eiskeime bilden können, erhöhen. Bei hohen, aber vertretbaren Konzentrationen von Aerosolpartikeln ist die Reflektivität der Wolken stark reduziert. Daraus schließen wir, dass die Existenz stabiler Wassergürtel-Zustände durch die Konzentration dieser Partikel bestimmt werden kann.
Aus dem zweiten Teil dieser Arbeit schlussfolgern wir, dass das explizite Auflösen von konvektiven atmosphärischen Prozessen helfen kann, die Reflektivität von Mischphasen-Wolken während des Kryogeniums genauer zu bestimmen. Allerdings ist eine Eingrenzung der Reflektivität von Mischphasen-Wolken dennoch nur bedingt möglich, da unser begrenztes Wissen über die damalige Konzentration und Zusammensetzung von Aerosol stark begrenzt ist.

Insgesamt schlussfolgern wir, dass Wassergürtel-Zustände angesichts der großen Unsicherheit, die mit der Abbildung von Mischphasen-Wolken und ihrer Wechselwirkung mit Strahlung in atmosphärischen Modellen einhergeht, weiterhin eine unsichere Eigenschaft des Klimas der Erde bleiben. Die Idee, dass Szenarien mit einem Wassergürtel-Zustand die geologischen Befunde des Kryogeniums erklären können, wird durch unsere Ergebnisse stark in Frage gestellt. Die damaligen Lebewesen waren daher mit hoher Wahrscheinlichkeit den harschen Bedingungen eines vollständig mit Eis bedeckten Ozeans ausgesetzt.

Preface

The PhD candidate confirms that the research presented in this thesis contains significant scientific contributions by himself. This thesis reuses material from the following publications.

Braun, C., J. Hörner, A. Voigt, and P. Joaquim, 2022a: Ice-free tropical waterbelt during Snowball Earth events questioned by uncertain clouds. *Nature Geoscience*, **15**, 489–493, https://doi.org/10.1038/s41561-022-00950-1.

Braun, C., A. Voigt, C. Hoose, A. M. L. Ekman, and J. G. Pinto, 2022b: Controls on subtropical cloud reflectivity during a waterbelt scenario for the Cryogenian glaciations. *Journal of Climate*, https://doi.org/10.1175/JCLI-D-22-0241.1.

The abstract, chapters 1, 2, 4, 5, 7 and appendix A reuse material from Braun et al. (2022a). ©The Authors. The abstract, chapters 1, 2, 4, 6, 7 and appendix B reuse material from Braun et al. (2022b). ©American Meteorological Society. Used with permission. This preliminary version has been accepted for publication in the Journal of Climate and may be fully cited. The final typeset copyedited article will replace the EOR when it is published.

The research leading to the results was funded by the Deutsche Forschungsgemeinschaft (DFG) under the grant agreement VO 1765/5-1. The research proposal of the DFG grant was written by Prof. Dr. Aiko Voigt, IMG, University of Vienna. The ICON-NWP 2.6.1, ICON-LEM and CAM 3.1 simulations and the analyses in Braun et al. (2022a) and Braun et al. (2022b) were solely performed by the candidate. The ICON-AES 1.3.00 simulations with reduced efficiency of the Wegener-Bergeron-Findeisen process and the Winton sea-ice model were performed by M. Sc. Johannes Hörner, IMG, University of Vienna with advise from the candidate. All other ICON-AES simulations were performed solely by the candidate. The candidate also wrote the text with advice from Prof. Dr. Aiko Voigt, Prof. Dr. Joaquim G. Pinto and, for Braun et al. (2022b), from Prof. Dr. Corinna Hoose from IMK-TRO, KIT, and Prof. Dr. Annica M. L. Ekman, Department of Meteorology and Bolin Center for Climate Research, Stockholm University, Stockholm, Sweden. All modifications of ICON-AES, ICON-NWP, ICON-LEM and CAM were implemented by the candidate except linking ICON-AES with the Winton sea-ice model, which was implemented by Johannes Hörner with advise from the candidate.

The candidate confirms that appropriate credit has been given within the thesis where reference has been made to the work of others. This copy has been supplied on the understanding that this is copyright material and that no quotation from the thesis may be published without proper acknowledgment.

Contents

1. Introduction

Studying the evolution of the Earth system allows us to discover our past and to calibrate and test the tools that we use to project our future (Harrison et al., 2015; Kageyama et al., 2017). The Earth system evolves through the tight coupling of climate, geology, and life, which are entangled via a great variety of pathways that we just have started to discover (Lenton and Watson, 2013; Lovelock, 2016). Based on the ideas proposed by Charles Darwin in 1859 (Darwin, 2004), the evolution of life is driven by the climatic conditions (Hawkins et al., 2003). Recently, Earth's long-term climate was suggested to be stabilized by clouds, which may have helped to maintain surface temperatures within life-sustaining ranges by adjusting their reflectivity to the brightening sun (Goldblatt et al., 2021).

This thesis explores the stabilizing role of clouds during the Cryogenian, which lasted from 720 million years ago (Ma) to 635 Ma. The Cryogenian climate was characterized by major glaciation events (Pierrehumbert et al., 2011; Hoffman et al., 2017). These glaciation events imply drastic changes of Earth's climatic conditions that potentially paved the way for the intense diversification of life forms during the Cambrian explosion (541 to 488 Ma) (Erwin et al., 2011; Hoffman et al., 2017).

The geological evidence for the Cryogenian glaciations is classically interpreted based on the Snowball Earth hypothesis, which postulates globally ice-covered oceans and aligns Cryogenian proxies with an entire life cycle of the glaciations (Kirschvink, 1992; Hoffman et al., 1998; Pierrehumbert et al., 2011; Hoffman et al., 2017). However, the fossil evidence for the existence of advanced marine photosynthetic species, such as algae and especially sponges, challenges the Snowball Earth scenario because these species require habitats that provide near-surface liquid water (Love et al., 2009; Hoffman et al., 2017). Thus, alternative scenarios considering a permanent equatorial ice-free waterbelt were suggested to provide a robust hospitable habitat for Cryogenian life throughout the glaciations (Hyde et al., 2000; Abbot et al., 2011; Rose, 2015).

Among these waterbelt scenarios the so-called Jormungand hypothesis proposed by Abbot et al. (2011) is particularly attractive as it also proposes an entire life cycle for the glaciations. Moreover, the central mechanism of the Jormungand hypothesis that stabilizes the waterbelt climate is based on well-established atmospheric dynamics and physics. Similar to the Snowball Earth hypothesis, the Jormungand hypothesis considers the Cryogenian glaciations to be initiated by a runaway ice-albedo feedback (Kirschvink, 1992; Hoffman et al., 1998, 2017). However, according to the Jormungand hypothesis, the climate stabilized in a waterbelt state instead of a Snowball state because the runaway ice-albedo feedback weakened when the sea-ice edge entered the subtropical region (Abbot et al., 2011). In the original formulation of the Jormungand hypothesis by Abbot et al. (2011) the weakening of the ice-albedo feedback was considered to solely rely on the exposure of relatively dark bare sea ice. In the subtropical region, subsidence associated with the Hadley circulation suppressed precipitation, and promoted evaporation of high-albedo snow deposited on sea ice (Abbot et al., 2011). Hence, subtropical sea ice was snow-free and relatively dark. Abbot et al. (2011) demonstrated the Jormungand hypothesis in two general circulation models in idealized aquaplanet setups and a one-dimensional energy balance model.

Studies following the work of Abbot et al. (2011) investigated the validity of the Jormungand hypothesis in a variety of comprehensive coupled atmosphere-ocean models (Voigt and Abbot, 2012; Rose, 2015; Pollard et al., 2017). Yet, no comprehensive and robust understanding of the climatic impacts governing the waterbelt climate has emerged from these efforts. Thus, the question whether a waterbelt scenario is a viable explanation for the Cryogenian glaciations has remained unanswered.

This thesis provides a new perspective on the Cryogenian waterbelt scenario by elucidating the role of clouds in the central stabilizing mechanism of the Jormungand hypothesis. We focus on the impact of clouds on the subtropical weakening of the ice-albedo feedback by reducing the model complexity in terms of the considered Earth system components compared to previous modeling studies (Voigt and Abbot, 2012; Rose, 2015; Pollard et al., 2017). More specifically, we investigate the robustness of the Jormungand hypothesis in idealized aquaplanet setups, i.e., under the assumption of a global ocean and neglecting dynamical processes of the ocean and sea ice. To do so, we apply three-dimensional prognostic atmospheric models reaching from coarse-scale global general circulation models with horizontal grids spacings beyond 100 km to a fine-scale local large-eddy model with a horizontal grid spacing of several hundred meters. For the interpretation of the simulation results obtained from the three-dimensional atmospheric models we apply a one-dimensional energy balance model.

Our results reveal a critical role of clouds for the stability of waterbelt climate states. The corresponding analysis explains the underlying mechanism, which allows us to revisit the interpretation of previous studies. However, our results also demonstrate that the well-known uncertainty associated with the representation of clouds in atmospheric models (Boucher et al., 2013; Sherwood et al., 2014; McCoy et al., 2016; Zelinka et al., 2020) hampers stringent cloud-based arguments for or against the plausibility of a Cryogenian waterbelt scenario. Nevertheless, the new understanding of the impact of clouds on the central mechanism of the Jormungand hypothesis provides a new basis for future studies of waterbelt climate states both on Earth and on extrasolar planets.

The outline of this thesis is as follows. We start by reviewing the current state of knowledge regarding the Cryogenian glaciations with a focus on the Jormungand hypothesis and clouds in chapter 2, which motivates our research questions formulated in chapter 3. We further describe the applied atmospheric models and simulations in chapter 4 and present our results in chapters 5 and 6. Finally, we provide concluding remarks and an outlook in chapter 7.

2. Climate, Clouds, and Aerosols during the Cryogenian

The Cryogenian is an era in Earth's history that lasted from about 720 Ma to 635 Ma. The Cryogenian climate is characterized by two major glaciation events, the Sturtian (about 717 to 659 Ma) and the Marinoan (at least about 639 to 635 Ma) (Hoffman et al., 2017). We here review previous work exploring the Cryogenian glaciation events that provides the basis of this thesis and motivates our research questions presented in chapter 3. We first provide insight into the geological and fossil record, which form the basis to draw conclusions regarding Cryogenian climate (section 2.1). Afterwards we review the Snowball Earth hypothesis and its limitations regarding the explanation of the fossil record in section 2.2. The sections 2.1 and 2.2 are largely based on the reviews by Pierrehumbert et al. (2011) and Hoffman et al. (2017) as well as references therein. We further review Cryogenian waterbelt scenarios as an alternative to the Snowball Earth hypothesis in section 2.3. We particularly focus on the Jormungand-waterbelt scenario proposed by Abbot et al. (2011), which we review in section 2.4. Finally, we review previous work regarding cloud and aerosol impacts on Cryogenian climate in sections 2.5 and 2.6.

2.1. Cryogenian geology and biology

We here outline the characteristic features of the Cryogenian Earth by providing an overview of the geological and fossil record. We briefly summarize the key aspects at the end of this section.

Break-up of the super-continent Rodinia

Reconstructions based on paleomagnetic data and lithological information for sedimentary basins indicate that the Cryogenian paleogeography was characterized by the breakup of the supercontinent Rodinia (Li et al., 2013). At the beginning of the Cryogenian, Rodinia mostly covered low and mid latitudes and no land masses were located at the poles (Hoffman and Schrag, 2002; Pierrehumbert et al., 2011; Hoffman et al., 2017). The breakup of Rodinia coincides with the onset of the Sturtian glaciation event ($\sim$ 720 Ma) and was caused by the installation of the Franklin large igneous province (LIP) (Li et al., 2013). During the formation of the Franklin LIP wide-spread basaltic crust formation due to magma deposition at Earth's surface took place (Li et al., 2013).

Active tropical land glaciers at sea level

The geological record further indicates that land glaciers discharged into the ocean at tropical paleolatitudes over long periods during the Cryogenian (Hoffman and Schrag, 2002; Fairchild and Kennedy, 2007; Pierrehumbert et al., 2011; Hoffman et al., 2017). This is supported by paleomagnetic evidence (Evans, 2000), sedimentary facies and the wide-spread distribution of glacial deposits and traces such as dropstones, striations and diamictites (Hambrey and Harland, 1985; Pierrehumbert et al., 2011). Cryogenian glacial deposits are distributed globally (Kulling, 1934; Harland, 1964; Hoffman, 2011a), pointing toward a global climatic event (Hoffman et al., 2017). Moreover, recent advances in geochronology based on the radioactive decay of rhenium to osmium in organic-rich sediments and uranium to lead in zircon contained in volcanic ashes and rocks provide evidence for the synchronous onset and termination of the tropical glacial activity (see Table 1 in Hoffman et al. (2017) for an overview). Geochronology also affirms the separation of the tropical glacial activity into two distinctive events and provide estimates for the duration of these periods (Hoffman et al., 2017). The Sturtian glaciation is constrained to have lasted from 717 to 659 Ma and the Marinoan glaciation has been determined to have started between 650 to 639 Ma, lasting until 635 Ma. Hence, both events were long-lived and lasted for more than 50 million years in case of the Sturtian and 4 to 15 million years in case of the Marinoan glaciation event.

Banded iron formations

A remarkable stratigraphic feature of the Cryogenian is the presence of banded iron formations (BIFs) that contain high amounts of Fe oxide. The deposition of the BIFs is expected to be correlated with the presence of wide-spread ice cover because BIFs were found to contain glacial deposits (Hoffman and Schrag, 2002; Hoffman et al., 2017). The production of BIFs happens in two phases. In the first phase dissolved Fe(II) accumulates in water. This requires anoxic and asulfuric conditions, so that soluble Fe(II) is neither oxidized to unsoluble Fe oxide nor titrated to Fe sulfide. Anoxic conditions would be provided through globally ice-covered oceans, as the ice-shield would hamper the ocean-atmosphere gas exchange. In the second phase a localized oxidation agent is required to yield high local Fe oxide production (Hoffman et al., 2017).

Cap carbonates

The glacial deposits of the Cryogenian glaciation events are directly overlain by distinct layers of carbonate, so-called cap carbonates, which are distributed globally over present-day Earth (Kennedy, 1996; James et al., 2001; Shields, 2005; Jiang et al., 2006; Hoffman, 2011b; Hoffman et al., 2017). Sedimentary structures such as giant wave riples indicate that the carbonate deposition rates were high, which requires a rapid and extremely strong increase of carbonate ions in the ocean (Cloud et al., 1974; Peryt et al., 1990; Allen and Hoffman, 2005; Hoffman and Macdonald, 2010; Hoffman et al., 2017). In contrast, indication for magnetic reversals during the deposition of cap carbonates suggests slower deposition rates (Trindade et al., 2003; Kilner et al., 2005; Raub, 2008; Font et al., 2010; Hoffman et al., 2017). However, this ambiguity may be ruled out by considering higher rates of magnetic reversals during the Cryogenian due to a missing solid inner core of Earth (Hoffman et al., 2017). The formation of cap carbonates requires hot and acid rain and in consequence weathering of exposed carbonate on land. The dissolved carbonate ions are washed into the ocean, leading to supersaturation and subsequent precipitation of $CaCO_3$ (Pierrehumbert et al., 2011). Hot and acid rain can generally be caused by high atmospheric CO_2 concentrations (Pierrehumbert et al., 2011). In order to explain the high Cryogenian carbonate deposition rates, extremely high atmospheric CO_2 concentrations are expected to have prevailed during the deposition. High atmospheric CO_2 levels during the Cryogenian are supported by an oxygen mass-independent fractionation (Bao et al., 2009). The cap carbonates and the associated expectation of high atmospheric CO_2 concentrations is a key observation for testing potential scenarios that strive to explain the Cryogenian geological record.

Life during the Cryogenian

Over the last decades the fossil evidence for complex marine life during the Cryogenian has grown. We here first review unspecific indications for the activity of life in form of carbon isotope ratios and afterwards provide insight into more specific traces of Cryogenian life.

General traces for the activity of life during the Cryogenian can be derived from $\delta^{13}C$ anomalies, i.e., anomalies of the ratio of the carbon isotopes ^{13}C to ^{12}C (Pierrehumbert et al., 2011). Photosynthetic plants preferrably use ^{12}C isotopes as part of photosynthetic production and discriminate against the heavier ^{13}C isotope (see e.g. Körner et al. (1988)). Therefore, the remaining carbon pool exhibits a positive $\delta^{13}C$ anomaly during periods when photosynthetic marine species, such as algae, are active (Pierrehumbert et al., 2011). The $^{13}C/^{12}C$-ratio of the remaining carbon pool can be inferred from carbonate sediments. Consequently, negative variations of $\delta^{13}C$ in carbonate deposits indicate decreased organic carbon burial by photosynthetic species. Strong negative excursions of $\delta^{13}C$ coincide with the Sturtian and Marinoan glaciations indicating the shutdown of organic production during these periods (Pierrehumbert et al., 2011).

More specific traces of life are provided by biomarkers and fossils, which are dated with the help of molecular clocks. To a great extent, these traces are of marine origin and indicate diverse marine life during the Cryogenian. An exception is the evidence for fungi, which may have started to evolve on land before 715 Ma (Bonneville et al., 2020).

Sterane biomarkers indicate that complex marine eukaryotes already existed at the beginning of the Proterozoic (2500 Ma) (Waldbauer et al., 2009). The first eukaryotic photsynthetic species were algae (Gibson et al., 2018). Evidence for the existence of multi-cellular red algae dates back to the early Neoproterozoic (1000 to 900 Ma) and the major features of green algae likely were established before the Cryogenian (750 Ma) (Knoll, 1992). During the Cryogenian the evolution of algae continued leading to the replacement of red algae by green algae (Love and Summons, 2015; Brocks et al., 2017).

Marine, eukaryotic heterotrophs, i.e., organisms obtaining primary energy from other organisms, can be found in sediments dated to around 740 Ma (e.g. Porter (2006)). Microfossils with sizes of up to 1 mm that potentially also represent heterotrophic eukaryotes are found in cap carbonates dated to the end of the Sturtian (716−635 Ma) (Bosak et al., 2012).

Clades of multi-cellular animals that later successfully spread during the Ediacaran (635 to 541 Ma) and Cambrian (541 to 488 Ma) periods are expected to have diverged before the Sturtian (Erwin et al., 2011). The first evidence for animals in the fossil record is considered to originate from sponges - more precisely demosponges - that likely evolved before the Marinoan glaciation (Love et al., 2009; Love and Summons, 2015; Brocks et al., 2017; Lyons et al., 2021). This is based on biomarkers associated with marine demosponges that are found in the cap carbonate layer dated to the end of the Marinoan (Love et al., 2009; Love and Summons, 2015; Zumberge et al., 2018) and molecular clock evidence (Sperling et al., 2010). Digitally reconstructed fossils on the size of milimeters to centimeters that possibly resemble sponges and are dated to the pre-Marinoan support this evidence (Maloof et al., 2010). Less certain evidence even dates possible biomarkers originating from early animals to pre-Cryogenian times (e.g. Dohrmann and Wörheide (2017) and Brocks et al. (2017)).

Summary of Cryogenian geological and fossil evidence

We here summarize the most important features of the geological and fossil record. The Cryogenian climate was cooled by the low-latitude position of the super-continent Rodinia and the draw-down of atmospheric CO_2. The cold climate led to the formation of active tropical land glaciers, which is signaled by glacial deposits found in the paleo-tropics. These deposits are directly overlain by cap carbonates that indicate high atmospheric CO_2 concentrations and warm and moist conditions following the cold climate conditions. Finally, increasing fossil evidence supports the survival of complex marine species, such as sponges, throughout this sequence of diverse climatic conditions.

2.2. The Snowball Earth hypothesis

Most commonly, the evidence from the geological and fossil record described in the previous section is explained by the Snowball Earth hypothesis postulated by Kirschvink (1992) and Hoffman et al. (1998). The Snowball Earth hypothesis considers entirely ice-covered oceans. Therefore it is sometimes also referred to as *hard* Snowball Earth hypothesis to distinguish the associated climate state from so-called *soft* Snowball Earth states with high but non-universal ocean ice cover, which we discuss in section 2.3. The Snowball Earth hypothesis provides a full life cycle that allows one to explain the geological evidence during the Cryogenian. The Snowball life cycle has been demonstrated based on a one-dimensional energy balance model (EBM) (Budyko, 1969; Sellers, 1969) and Snowball Earth states were successfully simulated in fully coupled ocean-atmosphere GCMs (e.g. Voigt and Marotzke (2010); Voigt et al. (2011); Yang et al. (2012); Yang and Peltier (2012); Liu et al. (2013, 2017)). Thus, the Snowball Earth state is considered as a robust feature of the Earth system (Goddéris et al., 2011; Pierrehumbert et al., 2011; Hoffman et al., 2017). Before describing the Snowball life cycle we here introduce the EBM developed by Budyko (1969) and Sellers (1969). The EBM allows us to derive a bifurcation diagram that illustrates the Snowball life cycle (Fig. 2.1).

A one-dimensional energy balance model for assessing the Snowball Earth life cycle

Parts of this section are based on Braun et al. (2022a).
©The Authors.

The EBM balances absorbed solar radiation S with outgoing longwave radiation L and meridional heat transport (MHT) by considering local insolation I, planetary albedo α and surface temperature T at each latitude ϕ (Budyko, 1969; Sellers, 1969).

$$\begin{aligned} S(\phi) - L(\phi) &= \mathrm{MHT}(\phi) \\ I(\phi)(1-\alpha(T(\phi))) - (A_0 - F + BT(\phi)) &= C(T(\phi) - \overline{T}). \end{aligned} \tag{2.1}$$

A_0 and B are parameters of the linearized outgoing longwave radiation and F is the longwave radiative forcing with respect to a reference state. C scales meridional heat transport, which is parameterized to be proportional to the difference of T and the global-mean surface temperature $\overline{T}$. To represent the ice-albedo feedback, α has a high value of 0.6 for ice-covered ocean ($T(\phi) < T_s$) and a low value ($\alpha = 0.3$) for ice-free ocean ($T(\phi) \leq T_s$). We here use $T_s = -10$ °C following the suggestion in Abbot et al. (2011), which we refer to for a detailed description of the EBM and the applied parameters.

The bifurcation diagram calculated from the EBM for the Snowball hypothesis is shown in Fig. 2.1. The EBM considers only stationary states of the Earth system. Hence, the bifurcation diagram shows the equilibrium ice-edge latitude for a given CO_2-radiative forcing F. Solid lines indicate stable equilibria and dashed lines unstable equilibria. The continuum of unstable equilibria is also referred to as separatrix, as it separates the attractor basins of the temperate stable climate, indicated by the solid line at high ice-edge latitudes, and the Snowball climate, indicated by the solid line at an ice-edge latitude of 0°. The bifurcation diagram exhibits two bifurcation points, at which climate becomes unstable if the CO_2-radiative forcing is further decreased or increased and transitions to a different stable climate state. The bifurcation point $\mathcal{T}$ corresponds to the transition from the temperate to the Snowball climate. The bifurcation point $\mathcal{S}$ corresponds to the transition from the Snowball to the temperate climate. In the following we use the bifurcation diagram to describe the Snowball life cycle.

Snowball Earth initiation

During the Neoproterozoic the sun exhibited about 94 % of its present-day luminosity (Gough, 1981). Nevertheless, the pre-Cryogenian climate is believed to have been warmer than present-day climate due to higher CO_2 concentrations compared to present-day climate (Pierrehumbert et al., 2011). Higher CO_2

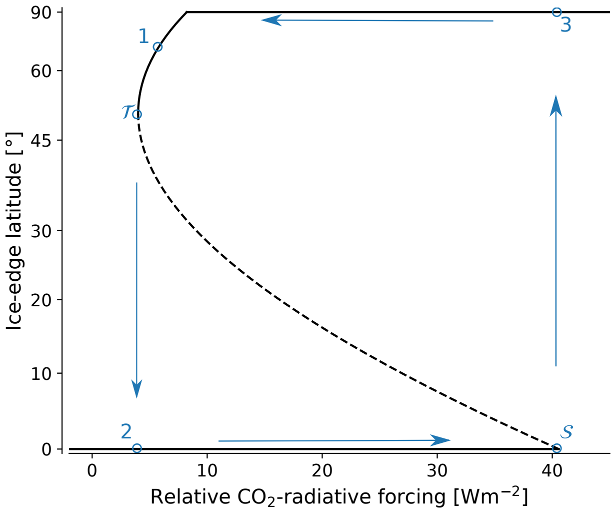

Figure 2.1.: Bifurcation diagram illustrating the Snowball Earth hypothesis. Equilibrium states of the Earth system are characterized by the global-mean ice-edge latitude and the CO$_2$-radiative forcing with respect to a reference state. Solid lines indicate stable equilibrium states and dashed lines indicate unstable equilibrium states. The temperate climate state is located at high ice-edge latitudes and the Snowball state at an ice-edge latitude of 0°. Blue arrows indicate the life cycle of the Cryogenian glaciations as suggested by the Snowball Earth hypothesis.

concentrations are thought to have been caused by the absence of vascular land plants, which reduced the efficiency of CO$_2$ removal from the atmosphere by silicate weathering (Berner, 2004). Hence, the starting point for the Snowball Earth life cycle is characterized by a stable temperate climate at a high ice-edge latitude indicated by point 1 in Fig. 2.1.

The initiation of the Snowball Earth life cycle was triggered due to tectonics. Two aspects are considered particularly relevant. First, the super-continent Rodinia formed in its low-latitude position right before the Cryogenian (Pierrehumbert et al., 2011). On the one hand, tropical continents may have a warming impact due to decreased tropical cloud cover over land (Fiorella and Poulsen, 2013). On the other hand, high land fraction at low latitudes has a cooling effect due to higher albedo of land compared to ocean (Kirschvink, 1992; Voigt et al., 2011) and reduced water vapor supply (Voigt et al., 2011). Furthermore, increased tropical land fraction enhances silicate weathering in the wet tropics leading to a reduction of atmospheric CO$_2$ (Marshall et al., 1988). In total, increased land fraction at low latitudes likely has a cooling effect on Earth's climate (Kirschvink, 1992; Hoffman et al., 2017).

Second, the basalt formation during the installation of the Franklin LIP enhanced silicate weathering, leading to a draw-down of atmospheric CO$_2$ (Macdonald et al., 2010). The breakup of Rodinia led to intrusion of sea water between tectonic plates, which moistened previously arid areas in the formerly off-coast continental regions of Rodinia and increased silicate weathering (Donnadieu et al., 2004a). The reduction of atmospheric CO$_2$ led to a reduction of the warming greenhouse effect of CO$_2$ and thus global cooling. Moreover, Earth's silicate weathering thermostat, which counteracts a reduction of atmospheric CO$_2$ and the corresponding cooling of Earth's climate, may have been less efficient during the early Cryogenian (Hoffman and Schrag, 2002). The silicate weathering thermostat refers to the decreasing

CO_2 removal from the atmosphere via silicate weathering under increasing continental ice cover (Walker et al., 1981). In the absence of polar land masses silicate weathering can only indirectly affected by polar ice cover (Hoffman and Schrag, 2002). This may have facilitated global cooling during the Cryogenian. In summary, Cryogenian tectonical activities may have led to a substantial cooling of climate.

Atmospheric cooling caused a lowering of the tropopause. This favored the injection of precursors of sulfur aerosol into the stratosphere that may have been released through volcanic eruptions during the installation of the LIP (Macdonald and Wordsworth, 2017). Stratospheric sulfur aerosol exerts a cooling effect at the surface that may last on the order of years (Self et al., 2014; Macdonald and Wordsworth, 2017; Glaze et al., 2017).

All these factors may have cooled Cryogenian climate leading to increased ice cover. With the sea-ice edge advancing towards the equator, the destabilizing positive ice-albedo feedback strengthened due to the increase of insolation with decreasing latitude. Once the ice albedo feedback became sufficiently strong to outweigh the stabilizing negative feedbacks, the Earth system reached a bifurcation point, indicated by $\mathcal{T}$ in Fig. 2.1. At the bifurcation point any further decrease of the CO_2-radiative forcing led to a run-away ice albedo feedback and a geologically rapid transition from temperate to a Snowball climate.

The rapid climatic transition is supported by the evidence for the synchronous onset of the tropical glaciations from Re-Os and U-Pb geochronology for the Sturtian and the Marinoan (see e.g. Hoffmann et al. (2004); Macdonald et al. (2010); Calver et al. (2013); Rooney et al. (2014); Nelson et al. (2020)). Using numerical simulations Hyde et al. (2000) determined a time scale of around 150 years for the transition from the temperate to the Snowball climate. Voigt and Marotzke (2010) found the transition from a temperate climate to a Snowball climate to last about 350 years when abruptly reducing insolation from 100 % to 94 % of the present-day value in ECHAM5/MPI-OM with a low-latitude Marinoan continental configuration. Given the time-scale of a few centuries for the transition from temperate to Snowball climate, the concentration of atmospheric CO_2 can be expected to have remained approximately constant during this transition. The stable state, in which the Earth system stabilizes, is therefore found at the same radiative forcing but at global ice cover, indicated by point 2 in Fig. 2.1. Snowball Earth initiation was intensely studied using comprehensive fully-coupled atmosphere-ocean GCMs (e.g. Voigt and Marotzke (2010); Voigt et al. (2011); Yang et al. (2012); Yang and Peltier (2012); Liu et al. (2013, 2017)) and was found to be consistent with the geological evidence (Hoffman et al., 2017).

Snowball Earth climate

The Snowball Earth atmosphere was considerably drier than under present-day climate conditions because of the overall low temperatures and reduced moisture supply from the surface (Voigt et al., 2012). Optically thick clouds mainly formed due to the strong ascent associated with a strong Hadley circulation (Abbot et al., 2013). The low surface heat capacity of the ice-covered ocean led to a large shift of the Hadley circulation with the seasonal cycle, which in the annual-mean led to a reversal of the surface moisture budget compared to present-day climate (Pierrehumbert, 2004, 2005; Pierrehumbert et al., 2011; Voigt, 2013; Abbot et al., 2013).

The cold climate led to the development of sea glaciers with thicknesses on the order of one kilometer (Goodman and Pierrehumbert, 2003; Li and Pierrehumbert, 2011). Sea-glacier flow was driven by gravitation and was directed from the high-latitude ice accumulation zone, where ice formation took place, toward the low-latitude ablation zone, where ice was consumed due to bottom melting and surface sublimation. Modeling studies indicate that sea ice may have grown to hundreds of meters in thickness within a few thousands of years (Warren et al., 2002; Goodman and Pierrehumbert, 2003; Li and Pierrehumbert, 2011; Pierrehumbert et al., 2011; Goodman and Strom, 2013).

Under global ice cover the ocean-atmosphere gas exchange strongly slowed down and the ocean became anoxic. This prevented the oxidisation of soluble Fe(II) which consequently accumulated in the ocean. In regions of oxygen availability, e.g. in basins at coastal margins with meltwater supply, non-soluble ferrous oxides formed and precipitated (Hoffman et al., 2017). Hence, an ice-covered anoxic ocean with local meltwater supply provides an explanation for the Cryogenian banded iron formations with embedded glacial deposits.

Snowball Earth hysteresis and termination

In the extremely cold Snowball climate, continental silicate weathering strongly slowed-down due to the weaker hydrological cycle, the generally reduced efficiency of weathering at lower temperatures, and the formation of land glaciers (Walker et al., 1981). Hence, CO_2 released by volcanic eruptions accumulated in the atmosphere and increased the CO_2-radiative forcing (Kirschvink, 1992; Lan et al., 2022). Due to the globally high surface albedo under the cold Snowball climate conditions, a small to moderate increase of the CO_2-radiative forcing did not allow Earth to return to the temperate climate. This behavior is a fundamental feature of the Earth system and is based on the strong albedo difference between ice-covered and ice-free surfaces. In fact, the CO_2 radiative forcing had to build up to very high values to enable the escape from the Snowball state indicated by bifurcation point $\mathcal{S}$ (Pierrehumbert, 2005; Le Hir et al., 2010; Abbot et al., 2013). Hence, over the range of atmospheric CO_2 concentrations marked by points 2 and $\mathcal{S}$ in Fig. 2.1 two stable states of the Earth system exist at the same CO_2-radiative forcing, i.e., the temperate state and the Snowball state. The occurrence of two stable states at the same radiative forcing is referred to as bistability. We refer to the range of the atmospheric CO_2-concentration and the range of the associated CO_2-radiative forcing for which Earth exhibits bistability as CO_2-hysteresis.

The Snowball Earth hypothesis suggests strong CO_2-hysteresis of the Earth system. Relatively low CO_2 concentrations are required for the initiation and high CO_2 concentrations are required for the termination of the Snowball Earth state. Estimates based on modeling studies suggest volume mixing ratios of CO_2 between 0.01 to 0.1 required to terminate a Snowball Earth state depending on the impact of clouds (Abbot et al., 2012; Abbot, 2014), dust aerosol (Abbot and Halevy, 2010), and dust aeolian deposits, darkening the surface (Abbot et al., 2010; Le Hir et al., 2010; Pierrehumbert et al., 2011) as discussed in more details in sections 2.5 and 2.6. Concerns that the Earth may not be able to escape a Snowball have been expressed by unrealistic high radiative forcing required to melt a Snowball (Pierrehumbert, 2005) or potentially enhanced deposition of frozen CO_2 in the winter hemisphere of a Snowball Earth (Turbet et al., 2017). Both concerns are considered uncritical for the viability of the Snowball Earth hypothesis (Abbot et al., 2012; Hoffman et al., 2017).

After having reached the critical CO_2 concentration for Snowball termination the rapid transition to a warmer climate state is estimated to last around 2000 years (Hyde et al., 2000). This aligns with the geochronlogical evidence for the synchronous global termination of the glaciations (Hoffman et al., 2017). The unstable transition at the termination occurs between the points S and point 3 in the bifuraction diagram in Fig. 2.1. The warm and moist high-CO_2 climate after the Snowball termination was additionally warmed by the positive water vapour feedback. This provided favorable conditions for the rapid formation of cap carbonates that consist of $CaCO_3$. High precipitation rates of $CaCO_3$ in the oceans were supported by weathering of highly abundant shattered rock and unweathered loess particles created by land glaciers during the Snowball episode (Fabre and Berger, 2012). Increased surface runoff transported $CaCO_3$ to the ocean (Higgins and Schrag, 2003). Due to enhanced weathering under warm and moist conditions the climate returned to a temperate state with moderate CO_2 concentrations after a couple of million years (point 1 in Fig. 2.1) (Pierrehumbert et al., 2011).

Overall, the Snowball Earth life cycle is appealing because it is based on straightforward physical mechanisms and is able to explain the geological record. The rapid and drastic climatic changes associated with a global Snowball event also align with the indications for reduced photosynthetic productivity derived from the negative excursions of the carbon isotopic composition found in Cryogenian sediments (Pierrehumbert et al., 2011). Yet, aligning the Snowball Earth hypothesis with the existence of specific complex marine photosynthetic species such as algae and demosponges throughout the Cryogenian glaciations requires a more detailed consideration of the Snowball climate.

Survival of life under Snowball Earth climate conditions?

Phototrophic marine species required either ice-free oceanic regions or regions with thin sea ice, i.e., thinner than 20 m, for a sufficiently high supply of solar radiation (Warren et al., 2002; Dadic et al., 2013). The gravitational spread associated with kilometer thick sea glaciers that formed in a Snowball climate rapidly closed gaps in the ice shield (Warren et al., 2002; Goodman and Pierrehumbert, 2003; Pierrehumbert et al., 2011; Li and Pierrehumbert, 2011; Goodman and Strom, 2013). Campbell et al. (2011, 2014) suggested potentially ice-free ocean regions in marine embayments. However, simulations with two-dimensional ice-models coupled to GCMs using Cryogenian paleogeography suggested that even in marine embayments sea ice grows several hundred meters thick (Hoffman et al., 2017). An increased geothermal flux (Hoffman et al., 2017) or near-by low-albedo land surfaces (Benn et al., 2015) potentially allowed the existence of thin or absent sea ice in long and narrow marine embayments. Overall, during the Cryogenian permanent small areas of ice-free ocean are unlikely to have existed and even areas with thin ice were difficult to maintain (Hoffman et al., 2017).

Sea-glacier flow may have induced relative movement of adjacent packets of ice, especially in the vicinity of land masses (Hoffman et al., 2017). This may have led to shear and associated cracks in the ice shield. Due to the partial freezing of the sea water within these cracks, locally high salinity may occur. These so-called brine inclusions are known to provide habitats for complex eukaryotic species on present-day Earth (Thomas and Dieckmann, 2002). However, the cracks in the Cryogenian ice shields may have been up to 100 m deep, so that sunlight could penetrate to their ground only during very short periods (Hoffman et al., 2017).

The Snowball atmosphere is expected to have contained high amounts of mineral dust released from ice free continental regions and volcanic ash due to tectonic activity (see also section 2.6). If deposited on ice, mineral dust and volcanic ash leads to the formation of dark ice-dust, referred to as cryoconite (Hoffman, 2016). Due to its low albedo, cryoconite absorbs sufficient solar radiation to melt the underlying snow or ice and form so-called cryoconite holes. In present-day climate cryoconite holes are known to host green algae, fungi, and other complex species in polar regions (Christner et al., 2003; Zawierucha et al., 2015). In present-day climate, high-latitude cryoconite holes only contain liquid in summer (Bagshaw et al., 2007; Fountain et al., 2008). In contrast, tropical Cryogenian cryoconite holes likely formed ice on their tops during nighttime only and might have never frozen over entirely, due to the dampened seasonal cycle. Larger accumulations of cryoconite may even have led to cryoconite ponds on Cryogenian ice shields. Yet, during the early and coldest stage of the Snowball climate, i.e., at relatively low CO_2 concentrations, the surface was likely too cold for cryoconite accumulation (Harder et al., 1996). Still, cryoconite holes may have developed in relatively warm marine embayments in the equatorial region (Campbell et al., 2011; Tziperman et al., 2012; Campbell et al., 2014). Thus, especially during the later and warmer phases of Snowball climate, cryoconite holes are considered as a likely habitat for complex eukaryotes (Hoffman, 2016).

Hoffman (2016) suggested the existence of large-scale stable habitats for advanced marine species based on the accumulation of cryoconite in the net-evaporation zone of sea-glaciers. The mechanism for the accumulation of cryoconite at the surface of sea-glaciers at low latitudes was first proposed by Li and Pierrehumbert (2011). This mechanism considers the transport of cryoconite within sea glaciers from high latitudes to the tropical net-evaporation zones, where cryoconite accumulated at the surface and formed large cryoconite ponds that were connected to each other. Freshwater production in cryoconite ponds led to the formation of moulins, through which meltwater and dust was flushed into the sub-glacial ocean. Hoffman (2016) suggested that permanent cryoconite accumulation and flushing created a stabilizing mechanism, which allowed the establishment of stable tropical habitats for cyanobacteria, fungi, and algae on the surface of sea-glaciers. Cryoconite ponds contained fresher, colder and more oxygenated water than the oceans. Moreover, they provided habitats with high amounts of insolation. Thus, cryoconite ponds may have contributed to the replacement of red algae that are adapted to low-light conditions by green algae, that are adapted to freshwater and oxidative stress (Gerdel and Drouet, 1960; Christner et al., 2003; Vincent et al., 2000, 2004). While cryoconite ponds are a promising explanation for the survival of algae, they most likely did not offer a potential habitat for demosponges because modern demosponges are sensitive to the level of salinity. Thus, Cryogenian demosponges are expected not to survive in the fresh water found in cryoconite ponds (Hoffman, 2016; Knight and Fell, 1987; Leamon and Fell, 1990).

Explaining the survival of demosponges in oceanic water is also problematic because freezing of sea water increases the overall salinity of the ocean. Hence, ocean water may have exhibited too high salinity for the survival of demosponges during the Cryogenian glaciations (Hoffman et al., 2017). Potentially, the pre-glacial Cryogenian seawater was less saline than present-day seawater (Blamey et al., 2016), which might have led to tolerable levels of salinity under Snowball Earth conditions. However, if assuming present-day salinity for pre-glacial Cryogenian oceans, the ocean salinity especially in the early phase of the Snowball episodes with thick global ice shields exceeded salinities, at which present-day demosponges can survive (Hoffman et al., 2017; Leamon and Fell, 1990). Environments with suitable levels of salinity might have existed close to meltwater discharging sites at the margins of the ice shield or moulins below large cryoconite ponds. However, freshwater supply and thus salinity is expected to have strongly varied over time. Especially in cold environments, demosponges have difficulties to cope with salinity-levels that deviate from the preferred level (Fell et al., 1989).

In summary, explaining the survival of demosponges during a Cryogenian Snowball Earth event is challenged by finding habitats with sufficient solar radiation and suitable levels of salinity. Moreover, the existence of potential habitats for complex eukaryotes in general is based on local characteristics of the Cryogenian Earth, especially during the early, very cold stage of the glaciations. Therefore, the existence of complex life such as demosponges so far remains a challenge for the Snowball Earth interpretation of the Cryogenian glaciations (Pierrehumbert et al., 2011; Hoffman et al., 2017).

A number of studies explicitly questions the plausibility of the Snowball Earth hypothesis. Arguments against a Snowball Earth climate are based on biomarker evidence for abundant marine primary productivity dated to 740 to 700 Ma (Olcott et al., 2005), the absence of major changes in silicified microfossils during the Cryogenian (Corsetti et al., 2006), broad fossil evidence for advanced life cycles of complex eukaryotes, that rely on well-oxygenated open water in the photic zone (Moczydłowska, 2008), theories of early animal evolution (Runnegar, 2000), and dissolved organic carbon remineralization (Peltier et al., 2007). Accordingly, alternative hypotheses to the Snowball Earth hypothesis were put forward.

Alternative hypotheses

A review of the most widely discussed hypotheses for the Cryogenian glaciations was provided by Fairchild and Kennedy (2007), which provides the basis for this subsection. Besides the hard Snowball Earth hypothesis, Fairchild and Kennedy (2007) discussed the zipper-rift Earth hypothesis (Eyles and Januszczak, 2004) and the high-tilt Earth hypothesis (Williams, 1975), which we will briefly discuss in this section. Moreover, Fairchild and Kennedy (2007) also promoted the idea of a waterbelt climate state with ice-free tropical ocean, which we will further discuss in section 2.3.

The zipper-rift Earth hypothesis was first fully formulated by Eyles and Januszczak (2004). The zipper-rift Earth hypothesis explains tropical land glaciers by the regional rifting of the margins of the super-continent Rodinia. Elevated continental margins are supposed to have led to active land glaciers and the creation of local glacial deposits that were preserved in rift basins. The zipper-rift Earth hypothesis is strongly challenged by the requirement to explain the high CO_2 concentrations required for the formation of the cap carbonates at the termination of the Cryogenian glaciations. Due to the low area fraction of ice cover on a global level, silicate weathering rates do not strongly decrease. This prevents a strong accumulation of atmospheric CO_2 and renders the zipper-rift Earth hypothesis as an unlikely explanation for the Cryogenian glaciation events (Fairchild and Kennedy, 2007).

The high-tilt Earth hypothesis considers an extremely increased obliquity of the Earth's rotation axis of up to 60° and was promoted by Williams (1975). The high tilt is supposed to have led to the tropics being colder than the extratropics and subsequent formation of active tropical land ice sheets. Kirschvink (1992) questioned the high-tilt Earth hypothesis for two reasons. First, Kirschvink (1992) noted the lack of a mechanism that is able to explain the intense orbital oscillations that were suggested by Williams (1975). Second, according to Kirschvink (1992), the high-tilt Earth hypothesis fails to explain why glacial deposits are directly overlain by cap carbonates. The redistribution of the radiative energy input into the Earth system under high obliquity led to the polar regions being warm. Therefore, carbonate deposits would be found at the poles instead of low latitudes. In contrast, glacial deposits originating from tropical land glaciers would still be found at low latitudes. These arguments disqualify the high-tilt Earth hypothesis as a likely explanation for the Cryogenian glaciations.

2.3. Cryogenian waterbelt scenarios

Parts of this section are based on Braun et al. (2022a).
©The Authors.

Fairchild and Kennedy (2007) considered the waterbelt state as a pragmatic compromise between the hard Snowball Earth hypothesis with fully ice-covered oceans and the evidence for the survival of complex marine species. Therefore, Fairchild and Kennedy (2007) did not link the waterbelt state to a specific scenario or mechanism. Fairchild and Kennedy (2007) referred to the idea of a waterbelt climate state as *Slushball Earth hypothesis*. We prefer to use the term *waterbelt state* because the usage of the term *Slushball Earth*, sometimes also *soft Snowball Earth*, is not uniform in the literature. For example, Fairchild and Kennedy (2007) use Slushball Earth to generally refer to climate states with high but non-universal ice cover, i.e., larger or smaller portions of the low-latitude oceans being ice-free. In contrast, Abbot et al. (2011) refers to Slushball Earth states as climate states with ice-edge latitudes in between 25° to 40° latitude that do not exhibit hysteresis with temperate climate states. We here use the term *waterbelt state* as introduced by Pierrehumbert et al. (2011) to refer to climate states with high but non-universal sea-ice cover. More precisely, by *waterbelt states* we refer to climate states with ice-edge latitudes in between 5° to ∼30°, irrespective of whether the climate state exhibits hysteresis. Hence, waterbelt states comprise the above definitions of Slushball and soft Snowball Earth states. We prefer the usage of the term *waterbelt state* because it provides a clear description of the climate state and allows a consistent reference to such kind of climate state across studies (cf. Rose (2015) and Wolf et al. (2017)). In this section we review previous work focused on Cryogenian waterbelt scenarios.

Waterbelt scenarios provide a robust and straight-forward explanation for the survival of life during the Cryogenian glaciations, since in the ice-free tropical ocean, life may have outlived the glaciations (Abbot et al., 2011). In order to align with the most fundamental geological evidence a waterbelt scenario has to satisfy two conditions. First, it has to allow the formation of tropical land glaciers. This implies a minimum threshold for ice cover since Rodehacke et al. (2013) found that tropical land glaciers do not develop if the ice-edge latitude is poleward of 20°. Second, the waterbelt state needs to exhibit CO_2-hysteresis with the temperate state to allow the formation of cap carbonates.

Early GCM studies faced the problem of much lower computing power than we have available today. This led to much coarser grid spacings being applied compared to present-day studies and too few resources to quantify the hysteresis of climate states. We explicitly note that, except for Hyde et al. (2000), hysteresis was not assessed in these early studies. Nevertheless, we review some of these studies in the following because they helped to grow confidence in the viability of a Cryogenian waterbelt scenario.

Hyde et al. (2000) conducted simulations with the GCM GENESIS 2 coupled to a thermodynamic mixed-layer ocean and thermodynamic sea ice, neglecting ocean and sea-ice dynamics. They found waterbelt states with an ice-edge around 25° latitude and - in contradiction to Rodehacke et al. (2013) - with tropical land ice. In Hyde et al. (2000) no CO_2-hysteresis between the waterbelt and the temperate climate was found.

Chandler and Sohl (2000) conducted simulations with the GISS GCM with prescribed ocean heat convergence, a thermodynamic sea-ice parameterization and a reconstructed late Cryogenian continental setup with continents located at high Southern latitudes. They found waterbelt states but no Snowball states when varying atmospheric CO_2, solar luminosity, ocean heat transport, and obliquity. The highest global ice cover found was 68 %, corresponding to a global-mean ice-edge latitude of 19°.

Poulsen et al. (2001) and Poulsen and Jacob (2004) conducted simulations with the coupled ocean-atmosphere GCM Fast Ocean-Atmosphere Model (FOAM) using an idealized rectangular super-continent centered in the tropics. Under reduced insolation (95 % of present-day) and an atmospheric CO_2 concentration of 140 ppmv Poulsen et al. (2001) found Snowball states with mixed-layer oceans but not with a fully coupled ocean. In the latter case the sea-ice edge stabilized at 46° latitude, indicating a that ocean heat transport counteracts the expansion of sea ice towards the equator. Poulsen and Jacob (2004) found waterbelt states with sea-ice margins at 27° latitude, that were stabilized by wind-driven ocean heat transport and cloud-radiative effects.

Donnadieu et al. (2004b) conducted simulations with the coupled ocean–atmosphere model of intermediate complexity (CLIMBER-2) on a very coarse horizontal and vertical resolution using a reconstructed Cryogenian continental setup. They found that ocean dynamical processes modulate the CO_2 concentration, at which waterbelt states transition into a Snowball state. Waterbelt states were found with ice-edge latitudes at a minimum of around 30° latitude. Donnadieu et al. (2004b) considered the major stabilizing effect on the simulated waterbelt climate to be meridional atmospheric heat transport via the Hadley circulation.

Micheels and Montenari (2008) found a low-latitude waterbelt state with an ice-edge around 15° latitude in simulations in an atmospheric GCM coupled to a thermodynamic mixed-layer ocean and sea-ice scheme using reconstructed Cryogenian continents. In any simulation that was not initialized with global sea-ice cover, at least some parts of the ocean remained ice-free, indicating robustness of waterbelt climate states.

More recent studies by Rose (2015) and Abbot et al. (2011) provided model evidence for hysteresis of waterbelt and temperate climate and simultaneously for the formation of tropical land glaciers.

Rose (2015) found waterbelt states with significant CO_2 hysteresis with ice edges stabilized between 21° and 30° latitude in the highly parameterized but fully coupled ice-ocean-atmosphere model MITgcm. Ocean heat convergence at the ice edge driven by a feedback between ice extent, wind stress and ocean circulation was found to stabilize the waterbelt state. In contradiction to Rodehacke et al. (2013), Rose (2015) also found indications that tropical land glaciers may form if the sea-ice edge reaches 20° latitude.

Abbot et al. (2011) postulated the existence of waterbelt states with ice-edge latitudes between 5° and 15° latitude thanks to the albedo contrast between high-albedo extratropical and low-albedo subtropical sea ice in the so-called Jormungand hypothesis. The Jormungand hypothesis proposes an entire life cycle of the Cryogenian glaciations and rests on well-understood atmospheric physics, i.e., the Hadley circulation and corresponding surface net-evaporation in the subtropics. This qualifies the Jormungand hypothesis as an interesting and appealing alternative to the hard Snowball Earth hypothesis. Therefore, in this thesis we investigate the viability of the Jormungand hypothesis as an alternative explanation for the Cryogenian glaciations and review the Jormungand hypothesis in section 2.4.

2.4. The Jormungand hypothesis

Parts of this section are based on Braun et al. (2022a).
©The Authors.

The Jormungand hypothesis was developed by Abbot et al. (2011). It is based on the albedo contrast between bright, snow-covered sea ice in the extratropics and dark, bare sea ice in the subtropical region. The strong contrast is supported by field measurements, laboratory work, and modeling studies (Warren et al., 2002; Brandt et al., 2005; Light et al., 2016; Carns et al., 2016). Abbot et al. (2011) explored the Jormungand hypothesis by extending the one-dimensional energy balance model (EBM) by Budyko (1969) and Sellers (1969).

A one-dimensional energy balance model to assess the Jormungand life cycle

Abbot et al. (2011) extended the EBM defined by Eq. 2.1 by considering the planetary albedo α to not only being a function of surface temperature T, but to also depend on latitude ϕ. The temperature- and latitude-dependent parameters suggested by Abbot et al. (2011), for α are

$$\begin{aligned} \alpha(T > T_s, \phi) &= \alpha_o = 0.35 && (2.2) \\ \alpha(T \leq T_s, \phi > 20^\circ) &= \alpha_{i,s} = 0.8 && (2.3) \\ \alpha(T \leq T_s, \phi \leq 20^\circ) &= \alpha_{i,b} = 0.45. && (2.4) \end{aligned}$$

$T_s = 0$ °C and resembles the temperature, below which the ocean's surface is covered by ice. Hence, α_o denotes the planetary albedo over ice-free ocean. $\alpha_{i,s}$ and $\alpha_{i,b}$ are the planetary albedo over ice-covered ocean in the extratropics, where sea ice is covered by snow, and at low latitudes, where sea ice is bare.

The corresponding bifurcation diagram is shown in Fig. 2.2. The bifurcation diagram exhibits an additional stable climate state with global-mean ice-edge latitudes located in the subtropical region at around 10° to 20° latitude. We refer to this climate state as waterbelt state. Along with the waterbelt state two additional bifurcation points occur in the bifurcation diagram. These mark the unstable transitions from the waterbelt climate to the Snowball climate $\mathcal{W}^1$ and from the waterbelt climate to the temperate climate $\mathcal{W}^2$. We will use the bifurcation diagram shown in Fig. 2.2 to outline the life cycle of the Cryogenian glaciations suggested by the Jormungand hypothesis. The description is based on Abbot et al. (2011).

The Jormungand life cycle

Similar to the Snowball Earth hypothesis, the Jormungand hypothesis suggests that enhanced continental weathering decreased pre-glacial atmospheric CO_2 and drove Earth toward a colder climate with increasing ice cover, which strengthened the ice-albedo feedback (point 1 toward $\mathcal{T}$ in Fig. 2.2). After reaching a critical extent of global ice cover, a bifurcation occurred ($\mathcal{T}$) leading to a runaway ice-albedo feedback. In the subtropics, subsidence associated with the Hadley circulation and moisture export by eddies towards the extratropics suppressed precipitation and promoted evaporation of high-albedo snow deposited on sea ice as illustrated in Fig. 2.3. Hence, subtropical sea ice was snow-free and relatively dark, which weakened the ice-albedo feedback when sea ice entered the subtropics. The strong albedo

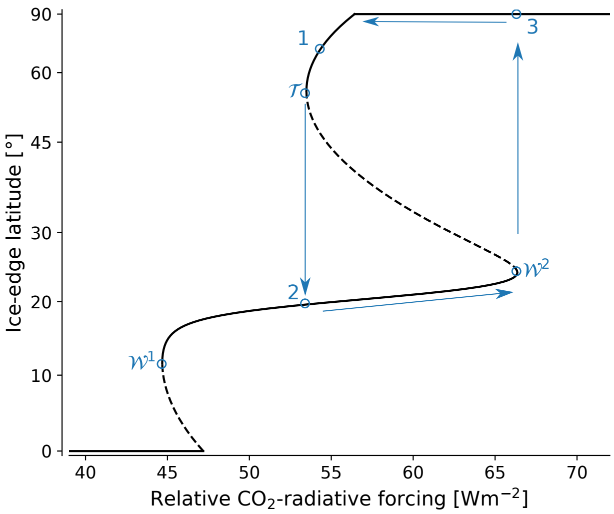

Figure 2.2.: Bifurcation diagram illustrating the Jormungand hypothesis. Equilibrium states of the Earth system are characterized by the global-mean ice-edge latitude and the CO$_2$-radiative forcing with respect to a reference state. Solid lines indicate stable equilibrium states and dashed lines indicate unstable equilibrium states. The stable waterbelt climate is located at ice-edge latitudes between 10° to 20°. Blue arrows indicate the life cycle of the Cryogenian glaciations as suggested by the Jormungand hypothesis.

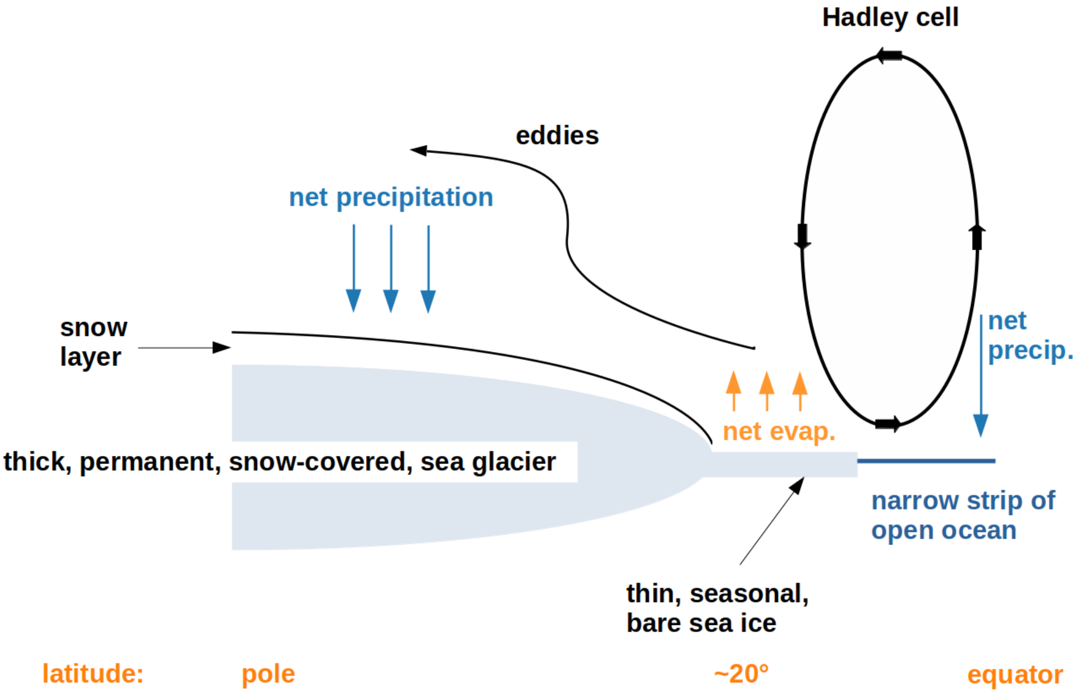

Figure 2.3.: Schematic of the central mechanism of the Jormungand hypothesis leading to the weakening of the ice-albedo feedback. In the subtropical region around 20° latitude subsidence associated with the Hadley circulation and moisture export by eddies towards the extratropics lead to net evaporation at the surface. This leads to the sublimation of snow deposited onto sea ice leaving behind bare sea ice that exhibits a lower albedo than snow. Thus, the ice-albedo feedback weakens once sea ice penetrates into the subtropical region, which allows climate to stabilize with a narrow strip of ice-free ocean around the equator. The figure is adapted from Abbot et al. (2011).

contrast between snow and sea ice constitutes the core of the Jormungand hypothesis. The weakening of the ice-albedo feedback was so drastic as to halt the runaway and thus climate did not rush into a hard Snowball but stabilized in a waterbelt state (point 2). In the waterbelt climate extratropical sea ice was permanent and grew to high thickness, potentially leading to sea-glacier flow towards the equator. In contrast, subtropical sea ice expanded and retreated seasonally as forced by insolation and therefore was thin. Under near-global ice cover, silicate weathering was largely shut down and CO_2 released by volcanic eruptions accumulated in the atmosphere. Due to the high planetary albedo, Earth's climate stayed within the waterbelt state until the greenhouse effect overcame the strong ice-albedo feedback (point $\mathcal{W}^2$). Hence, CO_2-hysteresis between waterbelt and temperate climate states occurred over a considerable range of atmospheric CO_2 concentrations, which is consistent with the deposition of the characteristic cap carbonate layers during the termination of the glaciations. However, the required CO_2 concentration for the termination of a waterbelt state is lower than for a Snowball state (Pollard et al., 2017). This implies that the termination of the Cryogenian waterbelt state would be less dependent on the warming impact of clouds and mineral dust as reviewed in sections 2.5 and 2.6.

A general caveat of waterbelt states is that so far, no explanation has been formulated how a waterbelt climate may be aligned with the evidence of banded iron formations during the Cryogenian (Hoffman et al., 2017). Nevertheless, the Jormungand life cycle provides a plausible interpretation for the survival of Cryogenian life, CO_2-hysteresis, and the existence of active ice sheets at sea level on paleo-tropical continents.

For the geological relevance of the Jormungand-waterbelt scenario, the associated waterbelt state needs to satisfy two conditions. First, the waterbelt state needs to exhibit significant CO_2-hysteresis with the temperate climate. Second, the waterbelt state needs to be accessible from the temperate climate. In the remainder of this work we use $\mathcal{T}$, $\mathcal{W}^1$, and $\mathcal{W}^2$ to not only refer to the bifurcation points in Fig. 2.2 but also to refer to the CO_2-radiative forcing or the associated atmospheric CO_2 concentration at the bifurcation point. Significant CO_2-hysteresis of the waterbelt state with the temperate state requires $\mathcal{W}^2 >> \mathcal{T}$. Accessibility of the waterbelt state from the temperate state requires $\mathcal{W}^1 < \mathcal{T}$, i.e., the waterbelt state needs to exist at a lower CO_2-radiative forcing than the temperate state. In the following we review modeling studies that addressed the geological relevance of the Jormungand hypothesis and the robustness of Jormungand-waterbelt states.

The Jormungand life cycle in global climate models

The postulation of the Jormungand hypothesis by Abbot et al. (2011) was based on GCM simulations. Abbot et al. (2011) found geologically relevant waterbelt states in idealized aquaplanet simulations with the National Center for Atmospheric Research's Community Atmosphere Model v3.1 (CAM3) (Collins et al., 2004) and the Max Planck Institute's atmosphere model ECHAM5 (Roeckner et al., 2003). Both GCMs were coupled to a thermodynamic mixed-layer ocean with thermodynamic sea ice. However, since the sea-ice model in ECHAM5 did not interactively simulate snow deposition onto sea ice, extratropical high and subtropical low sea-ice albedo was prescribed in the ECHAM5 simulations to trigger the Jormungand mechanism.

Since the postulation of the Jormungand hypothesis, several studies have applied model setups similar to Abbot et al. (2011) or investigated the viability of the Jormungand hypothesis in more comprehensive models. We review these in the following.

Voigt and Abbot (2012) explicitly searched for waterbelt states with a low-latitude ice edge in the coupled atmosphere-ocean model ECHAM5/MPI-OM using a dynamics sea-ice model. The applied sea-ice model interactively simulated snow deposition onto sea ice. Voigt and Abbot (2012) considered reconstructed Marinoan continents (635 Ma) and a reduced solar insolation (94 % of modern) and conducted simulations for a range of constant atmospheric CO_2 concentrations. In order to find low-latitude waterbelt states Voigt and Abbot (2012) drastically lowered the albedo of bare sea ice from the default values to the values that were applied in ECHAM5 in Abbot et al. (2011), which allowed the waterbelt state to extent down to 18° ice-edge latitude before collapsing into a Snowball. By further switching of sea-ice dynamics the waterbelt state extended down to 9° latitude. Thus, Voigt and Abbot (2012) concluded that sea-ice dynamics strongly destabilize the waterbelt state. In contrast, the impact of ocean heat transport was found to be weak and the waterbelt state extended down to the same ice-edge latitude irrespective of whether ocean heat transport was active or not. In both cases the waterbelt state was stabilized by the Jormungand mechanism due to the exposure of bare subtropical sea ice. Although they did not explicitly test this, Voigt and Abbot (2012) stated that the waterbelt state was not separated from the temperate state by a bifurcation point and therefore lacked CO_2-hysteresis.

Based on their results, Voigt and Abbot (2012) suggested three stabilizing and three destabilizing mechanisms for low-latitude ice edges. The suggested stabilizing mechanisms were 1) the exposure of bare sea ice, 2) the convergence of ocean heat transport at the sea ice margin, and 3) the poleward ocean drag exerted on sea ice. The suggested destabilizing mechanisms were 1) the equatorward wind drag exerted on sea ice, 2) the equatorward sea-glacier flow, and 3) the weaker greenhouse effect due to the water-vapor feedback. Based on these mechanisms and previous work, Voigt and Abbot (2012) concluded that studies aiming to quantify the bifurcation points associated with waterbelt states need to at least consider the effects of sea-ice dynamics, the water-vapor feedback, clouds, atmospheric dynamics, ocean dynamics, sea-ice thermodynamics, and eventually sea-ice glaciers.

In contrast, Yang et al. (2012) and Yang and Peltier (2012) found waterbelt states with low latitude sea-ice edges with sea-ice dynamics being active in the coupled Community Climate System Model (CCSM) versions 3 and 4. CCSM3 applies CAM3 as its atmospheric component. Their setup used the present-day continental configuration. Both, the atmospheric CO_2 concentration and insolation were varied across simulations. In Yang et al. (2012) waterbelt states existed at ice-edge latitudes down to 14°, whereas they were limited to beyond 20° latitude in Yang and Peltier (2012). This was found to be consistent with the higher ice and snow albedos applied in Yang and Peltier (2012). Moreover, bistability of low-latitude states was found in Yang et al. (2012) between states with ice-edge latitudes at 16° and

30° latitude. However, the width of the associated CO_2-hysteresis is unclear, because the bistability was not further investigated. Yang et al. (2012) also noted that considering sea-ice dynamics destabilizes waterbelt states. Furthermore, in Yang et al. (2012) the ice-albedo feedback was found to be increased with increased vertical resolution of sea ice and reduced by considering melt ponds and leads. In Yang et al. (2012) the latter two effects modulated the albedos of snow and ice.

Rose (2015) discussed the compatibility of the ocean-heat-transport based waterbelt states in his simulations and the Jormungand-waterbelt states of Abbot et al. (2011). On the one hand, the albedo values prescribed in Rose (2015) can be considered to generally allow the Jormungand mechanism to act effectively. In Rose (2015) the albedo of thin, bare sea ice was 0.25. The bare sea-ice albedo increased to 0.6 for thick sea ice. Snow deposition onto sea ice was simulated interactively and the albedo of fresh cold snow was 0.8. Moreover, the waterbelt states found in Rose (2015) were located at ice-edge latitudes between 21° and 30° while Jormungand-waterbelt states found in Abbot et al. (2011) were located in between 5° to 15° latitude. Rose (2015) concluded that there is no overlap in the two climate states and the mechanisms could jointly act in favor of a wide waterbelt climate state. On the other hand, Rose (2015) found an equatorward shift of the net-evaporation zones with increasing ice cover in his coupled simulations leading to sea ice being snow-covered everywhere. Therefore, Rose (2015) suggested that the coupled atmosphere-ocean circulation might prevent the Jormungand mechanism.

Similarly, Pollard et al. (2017) found ubiquitous subtropical snow cover on sea ice in GCM simulations with GENESIS using a model configuration close to Abbot et al. (2011). Pollard et al. (2017) particularly used albedo values similar to Abbot et al. (2011). The reason for the absence of bare-ice regions was hypothesized to be caused by small-scale convective atmosphere dynamics. For CAM3, Pollard et al. (2017) assumed that after sublimation of snow or ice, water vapor is advected out of the bare-sea-ice zone before it is consumed by clouds and corresponding precipitation again. For GENESIS, Pollard et al. (2017) assumed that rapid re-precipitation of sublimated ice or snow occurs. Pollard et al. (2017) concluded that the different behavior of CAM3 and GENESIS might arise from small-scale dynamical circulations that cover a few grid cells or from the applied sub-grid convective plume models. Furthermore, Pollard et al. (2017) found strong effects of ocean heat transport and sea-glacier flow on the bifurcation diagrams derived from additional simulations conducted with a sea-glacier model interactively coupled to GENESIS Pollard et al. (2017).

Finally, waterbelt states potentially based on the Jormungand mechanism were found by Shields et al. (2013) and Wolf et al. (2017) in studies of the climates of extrasolar planets using CCSM4 with a mixed-layer ocean. Shields et al. (2013) applied CCSM4 with snow and sea-ice albedo parameterizations taken from CCSM3, i.e., similar to Abbot et al. (2011). Shields et al. (2013) found low-latitude waterbelt states, which they suspected to exist thanks to the albedo contrast between snow-covered and bare sea ice, which forms the core of the Jormungand hypothesis. Wolf et al. (2017) built their work on the set of simulations conducted as part of Shields et al. (2013). Since the waterbelt climate state is located in between the temperate and the Snowball state, Wolf et al. (2017) considered the waterbelt climate to extend the range of habitable climates, which they defined via the availability of liquid water at the surface.

Due to its proximity to the Snowball climate, the Jormungand-waterbelt climate needs to be robust against variations of external and internal climate forcings (Pierrehumbert et al., 2011). On the one hand, Yang et al. (2012) assessed the stability of a waterbelt state against variations in solar forcing and found that Milankovitch-type variations do not destabilize the waterbelt state. Furthermore, Micheels and Montenari (2008) found the simulated waterbelt climate to be robust against variations of continental surface albedo. On the other hand, Abbot et al. (2011) concluded from the analysis of the EBM, which they applied to explore the Jormungand mechanism, that the impact of clouds on the planetary albedo may determine the geological relevance of waterbelt states. Abbot et al. (2011) further noted that the uncertainty associated with the cloud representation in atmospheric models may have implications for Jormungand-waterbelt states. Similar to clouds, aerosol also impacts the planetary albedo directly via aerosol-radiation interactions and aerosol-cloud interactions (e.g. Twomey (1977); Storelvmo and Tan (2015)). Both clouds and aerosol-cloud interactions are major contributors to the uncertainty of climate model responses (Boucher et al., 2013) and have been considered as important players during Cryogenian climate (Pierrehumbert et al., 2011; Hoffman et al., 2017). Therefore, we provide a short overview of the literature discussing radiative impacts of clouds and aerosols during the Cryogenian glaciations in the following sections.

2.5. Clouds during the Cryogenian glaciations

Since the Jormungand mechanism relies on the weakening of the radiation driven ice-albedo feedback, we here focus on the radiative impact of clouds. Given fixed optical properties of a cloud, its net radiative effect is determined by the cloud's location and altitude. In the cold Cryogenian climate the location is particularly important because it determines whether the cloud is located over a bright or a dark surface (Pierrehumbert, 2002). In general, clouds may have a warming effect at the surface due to absorption and re-emission of thermal longwave radiation and a cooling effect due to scattering of incident solar radiation in the shortwave spectrum. Over a dark surface the net effect of high-level clouds is warming and the net effect of low-level clouds is cooling. Given a cloud with fixed scattering efficiency, the cooling effect of shortwave scattering is determined by the albedo of the surface located below the clouds. The cooling shortwave effect is strong if a cloud is located over a dark surface with a low albedo and weak or absent if a cloud is located over a bright surface with a high albedo. Thus, over a bright surface clouds at any level warm the surface via longwave radiation. These effects govern the discussion of clouds during the Cryogenian, which focuses on Snowball initiation and termination as we outline in the following.

Early studies focused on the feasibility of simulating a Snowball climate applied GCMs with rather crude implementations of clouds because they were limited to very coarse resolutions in horizontal (up to 8° latitude and 10° longitude) and vertical direction (10 vertical levels and less) (Hyde et al., 2000; Chandler and Sohl, 2000; Poulsen et al., 2001; Poulsen and Jacob, 2004). Nevertheless, these studies provide a controversial discussion of cloud impacts in the context of Snowball Earth initiation.

Chandler and Sohl (2000) compared cloud impacts in climate states with minimum ice-edge latitudes of 30° to a modern control simulation using GISS GCM. They found decreased cloud cover over sea ice at high latitudes due to increased atmospheric stability over colder surfaces compared to warmer, ice-free oceans. At ice-free mid and low latitudes they found increased cloud cover, which they attributed to more energetic eddies caused by increased atmospheric energy transport. This increase of low-latitude clouds was interpreted as a positive cooling cloud feedback.

Conversely, Hyde et al. (2000) found that a colder atmosphere exhibits reduced absolute humidity, which led to a reduced cloudiness of up to 35 % in their GCM simulations with GENESIS. This led to a reduced planetary albedo in the equatorial region of the simulated waterbelt climate and may be considered as a cloud feedback acting against global glaciation.

In contrast, Poulsen et al. (2001) did not find a reduction of cloud cover in a colder climate in FOAM. In fact, they found even higher cloudiness in Cryogenian climate compared to present-day climate. However, they did not mention the optical thickness of the simulated clouds. Furthermore, Poulsen et al. (2001) suggested that in mid- and high latitudes clouds negatively feed back on the advance of the ice-edge because of the reduced shortwave cooling but maintained longwave warming of clouds located over ice. This suggestion was supported by GCM simulations of Poulsen and Jacob (2004), who found that the cloud radiative effect and the wind-driven ocean circulation are the most important factors to maintain a waterbelt climate in their FOAM simulations. If they disabled the longwave and shortwave cloud radiative effect the waterbelt state collapsed to a Snowball state within 15 years. Poulsen and Jacob (2004) found that the cloud radiative effect strongly warmed the surface in the presence of ice and weakly cooled the surface in the presence of ice-free ocean and therefore in total has a warming effect. Based on these results they suggested a feedback mechanism of clouds acting against the ice-albedo feedback, focusing on the longwave warming impact of clouds. In the absence of clouds over sea-ice, surface air temperatures were lower than in the presence of clouds (Poulsen and Jacob, 2004). This led to higher sensible heat loss of the ocean at the sea-ice margin and associated cooling of sea surface temperatures (Poulsen and Jacob, 2004). However, Poulsen and Jacob (2004) noted that this effect is subject to the uncertainty of cloud parameterizations in GCMs.

Pierrehumbert et al. (2011) noted that cloud parameterizations developed for present-day climate may not be suitable for Cryogenian Snowball conditions. However, to our knowledge cloud parameterizations specific for Cryogenian conditions have not been developed up to date. Pierrehumbert et al. (2011) proposed that progress may arise from future theoretical work and simulations with cloud-resolving models. They further pointed out that the difference in CO_2-thresholds for Snowball initiation between GCMs is determined by clouds and atmospheric dynamics.

Concerning Snowball deglaciation the effect of clouds is considered to be a clear longwave warming effect at the surface due to ubiquitous high surface albedo. Thus, clouds are considered to facilitate the termination of the Snowball climate (Pierrehumbert, 2002; Pierrehumbert et al., 2011; Abbot et al., 2012). The magnitude of the cloud surface warming was considered to be low in studies using FOAM (Pierrehumbert, 2004, 2005). This was later attributed to the specific implementation for cloud condensate, which does not yield plausible results under the cold Cryogenian conditions (Abbot et al., 2012). The magnitude of the cloud surface warming was also considered to be low in the Laboratoire de Météorologie Dynamique GCM (LMDZ) (Le Hir et al., 2010). In LMDZ Le Hir et al. (2010) found a considerable increase in cloud cover associated with a potential surface-warming feedback via increased moisture supply by altering the sub-grid distribution of vapor and liquid. However, they considered the altered sub-grid distribution as physically unlikely and found the warming effect to be too weak to considerably impact the Snowball deglaciation threshold.

Based on a comparison of 6 GCMs Abbot et al. (2012) and Abbot et al. (2013) concluded that the surface warming exerted by clouds might be sufficiently strong to reduce the atmospheric CO_2 concentration required for Snowball deglaciation by a factor of 10 to 100. Their comparison included the GCMs FOAM, GENESIS, CAM, LMDZ, and ECHAM5. The latter three GCMs were applied with parameterizations for cloud fraction and prognostic cloud condensate that were developed for modern climate. Furthermore, Abbot et al. (2012) and Abbot et al. (2013) applied super-parameterized CAM (SP-CAM), which uses a two-dimensional cloud resolving scheme within each gridbox. They found the cloud radiative effect to be positive in all simulations. The associated spread was about 35 Wm-2, which arose from substantial differences in cloud condensate and differences in the parameterizations of cloud optical properties. Abbot et al. (2013) further found that the GCMs with higher cloud radiative effect in the tropical region exhibit higher tropical heat export.

Abbot (2014) confirmed the magnitude of the warming cloud effect at the surface in the cloud-resolving model System for Atmospheric Modeling, version 6.10.4 (SAM). To our knowledge, this is the first and only study to date that studied Cryogenian climate in a cloud-resolving model. SAM was applied in an idealized setup with doubly periodic lateral boundaries on a quadratic domain spanning 128 km and reaching up to 17.5 km. The horizontal grid spacing was 1 km and in the vertical direction 59 levels were applied with refinement towards the lower boundary. Except small linear shear, no large-scale forcing was applied. Cloud microphysical processes were considered by a one-moment microphysical scheme. In these simulations Abbot (2014) found stratocumulus-like clouds located below a boundary layer inversion to be the dominant cloud type. The cloud longwave effect was found to be insensitive to cloud amount and particle size.

Finally, Koeberl and Ivanov (2019) suggested a deglaciation scenario, in which the atmospheric water vapor abundance in a Snowball Earth climate may drastically increase through the impact of asteroids that are 5–10 km in diameter. They expected the increased water vapor abundance to enhance cloud formation, which may facilitate deglaciation.

Overall, clouds are recognized as an important but admittedly uncertain feature of Cryogenian climate, especially in the context of waterbelt states and Snowball initiation.

2.6. Aerosol during the Cryogenian glaciations

Cryogenian aerosol abundance and composition is highly uncertain. Cryogenian aerosol scenarios cover a wide range and climatic impacts of aerosol have been discussed in the context of Snowball Earth initiation (Liu et al., 2021; Feulner et al., 2015; Macdonald and Wordsworth, 2017) and termination (Wu et al., 2021; Abbot and Halevy, 2010; Abbot and Pierrehumbert, 2010; Le Hir et al., 2010), as well as in Snowball climate itself (Li and Pierrehumbert, 2011; Hoffman, 2016). Macdonald and Wordsworth (2017) suggested volcanic eruptions to have impacted stratospheric sulfur aerosol abundance leading to global cooling that may have facilitated the initialization of the Cryogenian glaciations. The rise of eukaryotic algae (800-750 Ma) was hypothesized to have increased biogenic aerosol abundance leading to higher concentrations of cloud condensation nuclei and according to the Twomey effect optically thicker clouds (Feulner et al., 2015; Twomey, 1977). Specifically, Feulner et al. (2015) found, that the increased optical thickness induces stronger shortwave cloud cooling, which may have facilitated the initiation of the Cryogenian glaciations. However, increased marine organic production may also have led to a simultaneous increase of ice nucleaeting particle concentrations (Wilson et al., 2015), leading to optically thinner clouds. The most widely discussed Cryogenian aerosol species is mineral dust, for which the focus has mainly been on its atmospheric shortwave radiative effect (Abbot and Halevy, 2010) and the effect of surface darkening via dust deposition onto sea ice and snow (Abbot and Pierrehumbert, 2010; Le Hir et al., 2010; Pierrehumbert et al., 2011; Wu et al., 2021).

In the cold Snowball climate dust is expected to originate from continental ice-free areas and to accumulate on the surface of sea glaciers at low latitudes (Li and Pierrehumbert, 2011; Hoffman, 2016). We have reviewed the mechanism of dust accumulation and potential implications of dust deposition onto sea ice for the survival of advanced marine species in section 2.2. The radiative effect of low-latitude surface dust accumulation in a Snowball climate was found to be a strong warming effect in the GCM based studies of Abbot and Pierrehumbert (2010), Le Hir et al. (2010), and Wu et al. (2021). In these studies surface dust accumulation clearly facilitates Snowball deglaciation. Similarly, the radiative effect of dust aerosol was found to support Snowball deglaciation via surface warming in Abbot and Halevy (2010) using the Single Column Atmospheric Model (SCAM). Abbot and Halevy (2010) estimated Cryogenian dust aerosol concentrations to be one to two orders of magnitude higher in Snowball climate compared to present-day climate using the Dust Entrainment and Deposition (DEAD) box model of Zender et al. (2003) driven by GCM simulation results.

Liu et al. (2020) and Liu et al. (2021) studied the impact of the shortwave radiative effects of mineral dust aerosol and deposits onto snow and sea ice on the pre-glacial Cryogenian climate and the initiation of the glacial events. They applied the fully coupled atmosphere–ocean general circulation model CESM1.2.2 and considered interactive dust emission, transport, and the shortwave radiative effect of dust. To do so, they applied parameterizations for soil erodibility, dust emission size distributions, wet deposition, and optical properties. Liu et al. (2020) assumed that soil erodibility was high during the Cryogenian due to the absence of land vegetation. By considering high values of soil erodibility they found a global-mean atmospheric dust loading up to 40 times higher than in present-day climate. Liu et al. (2020) found that the high atmospheric dust abundance may have cooled the temperate pre-glacial Cryogenian climate by about 10 K, making the temperate climate more susceptible to transition to a colder climate state. However, Liu et al. (2021) found that the shortwave radiative effect of atmospheric dust acts against global ice cover due to the higher surface albedo in a colder climate. They found that in a colder climate the shortwave cooling effect of atmospheric dust is negligible and the planetary albedo is darkened through dust deposition onto snow and sea ice. Liu et al. (2021) also found that in a colder climate increased continental snow coverage decreases dust emissions. The formation of land glaciers might amplify this effect but was not considered in their study. Yet, Liu et al. (2021) found that in a colder climate, the atmospheric dust loading is not decreased for two reasons. First, precipitation and thus washout is reduced due to a less active hydrological cycle compared to warmer climate conditions. Second, the Hadley circulation strengthens with decreasing surface temperatures, which lifts aerosols to higher levels and increases their residence time within the atmosphere.

Mineral dust aerosols are considered to be the dominating species for heterogeneous ice nucleation in present-day climate (Kanji et al., 2017). Sagoo and Storelvmo (2017) found a high sensitivity of the climate during the last glacial maximum (around 20,000 years ago) to interactions of mineral dust aerosol with clouds. They applied the Community Earth System Model version 1.0.6 with CAM5 as the atmospheric component with an empirical parameterization for the ice nucleation on dust aerosols and prescribed dust emissions. In simulations with increased abundance of dust aerosols they found smaller and more numerous ice crystals in mixed phase clouds with an impact on cloud optical thickness, cloud lifetime, and precipitation. This increased the shortwave cloud radiative effect and resulted in a significant cooling at the surface. Furthermore, changes in the abundance of mineral dust aerosol led to large changes in hydrological processes that were associated with changes of atmosphere dynamics. Sagoo and Storelvmo (2017) concluded that indirect effects of mineral dust aerosols may significantly improve the shortcomings of paleoclimate simulations. However, in the studies of Cryogenian climate mentioned above, mineral dust aerosol has only been considered to impact climate via direct radiative impacts (Abbot and Halevy, 2010; Abbot and Pierrehumbert, 2010; Le Hir et al., 2010; Pierrehumbert et al., 2011; Wu et al., 2021). Despite the importance of mineral dust acting as INPs (Kanji et al., 2017), especially for simulations of climate states colder than present-day climate (Sagoo and Storelvmo, 2017), aerosol-cloud interactions have so far been neglected in studies considering the impact of mineral dust on Cryogenian climate.

3. Research Questions

As outlined in chapter 2 the classical Snowball Earth hypothesis and the associated life cycle provide comprehensive and sophisticated explanations for the Cryogenian geological record. Still, attempts to align the survival of sponges during the Marinoan glaciation with fully ice-covered oceans have failed so far (Hoffman et al., 2017). Hence, waterbelt scenarios with a narrow strip of ice-free tropical are attractive alternatives to the Snowball Earth hypothesis because they provide a large-scale refugium for the survival of complex marine life during the glaciations (Hyde et al., 2000; Abbot et al., 2011; Rose, 2015). The Jormungand hypothesis proposed by Abbot et al. (2011) is particularly attractive as it proposes an entire life cycle of the glaciations. The central mechanism of the Jormungand hypothesis, which leads to the weakening of the ice-albedo feedback, in the subtropical region rests on well-established atmospheric dynamics and physics. This motivates the overarching question that our work contributes to: Is the Jormungand hypothesis a viable alternative to the Snowball Earth hypothesis?

Jormungand-like waterbelt states were found in idealized aquaplanet setups with thermodynamic ocean and sea ice (Pierrehumbert et al., 2011; Abbot et al., 2011; Shields et al., 2013; Wolf et al., 2017). Furthermore, a variety of different model setups including continents, ocean heat transport and dynamics, and sea-glacier models has been applied to study the robustness of the Jormungand hypothesis since its postulation (Voigt and Abbot, 2012; Yang et al., 2012; Yang and Peltier, 2012; Rose, 2015; Pollard et al., 2017). While identifying climatic factors that stabilize or destabilize the waterbelt climate, these studies did not question the robustness of the central mechanism of the Jormungand hypothesis. Moreover, these studies have not comprehensively explained, under which conditions low-latitude waterbelt states based on the Jormungand mechanism can exist.

The goal of this thesis is to assess the robustness of the central mechanism of the Jormungand hypothesis, which provides a basic step for enhancing our understanding of the key factors governing the waterbelt climate. To focus on the central mechanism of the Jormungand hypothesis we apply an idealized aquaplanet setup. In the first part of this work, we analyze GCM simulations conducted with the Community Atmosphere Model in version 3.1 (CAM), as used by Abbot et al. (2011), and the ICOsahedral Nonhydrostatic atmosphere model in climate version 1.3.00 (ICON-AES) and answer the following research questions.

1. Is the Jormungand-waterbelt scenario a robust feature of Earth's climate?
    a) Are geologically relevant Jormungand-waterbelt states a robust feature of idealized aquaplanet simulations?
    b) Under which conditions do geologically relevant Jormungand-waterbelt states exist in idealized aquaplanet simulations?
    c) How do these conditions link to the weakening of the ice-albedo feedback in the subtropical region, which constitutes the core of the Jormungand hypothesis?
    d) Can we expect these conditions to be achieved during the Cryogenian?

We answer research question 1 and the corresponding sub-questions in chapter 5. By answering these questions we find a critical role of subtropical cloud reflectivity for the existence of geologically relevant waterbelt states. However, we also find a large difference of subtropical cloud reflectivity between the applied GCMs, which prohibits us to ultimately assess the plausibility of the Cryogenian Jormungand-waterbelt scenario. We show that the difference in cloud reflectivity arises from the uncertainties associated with representing clouds in GCMs, which is a well-known issue in modeling present-day climate (Boucher et al., 2013; Sherwood et al., 2014).

Therefore, in the second part of this thesis, we explicitly study Cryogenian subtropical clouds and discuss implications for the Cryogenian Jormungand-waterbelt scenario. Enhancing our understanding of Cryogenian clouds is primarily motivated by the critical role of subtropical cloud reflectivity identified in chapter 6. Moreover, the important but controversial role of clouds in Cryogenian climate as discussed in section 2.5 also motivates our detailed study of Cryogenian clouds, which is set up as follows.

First, we extend our analysis of subtropical cloud reflectivity in a waterbelt climate by an additional GCM simulation with the ICON model in numerical weather prediction mode v2.6.1 (ICON-NWP). Second, the uncertainty associated with the representation of clouds in GCMs largely arises from convection parameterizations (Sherwood et al., 2014) and aerosol-cloud interactions (Boucher et al., 2013). In order to gradually reduce the model uncertainty associated with the representation of clouds, we conduct a hierarchy of simulations across a wide range of horizontal grid spacings. To do so, we make use of the ICON model framework, which allows us to apply the same dynamical core from horizontal grid spacings larger than 100 km to 300 m. At the coarse end of this hierarchy we apply a global ICON-NWP simulation. At the fine end we apply ICON in large-eddy mode (ICON-LEM) using a nested grid within a limited-area simulation. Third, as outlined in section 2.6 mineral dust aerosol and associated aerosol-cloud interactions are an important aspect of Cryogenian climate. Therefore, we additionally conduct ICON-NWP and ICON-LEM simulations, in which we assess the sensitivity of Cryogenian subtropical cloud reflectivity to the abundance of mineral dust aerosol acting as ice nucleating particles. Collectively, these simulations allow us to answer the following research questions.

2. Can we rule out the Jormungand hypothesis in idealized aquaplanet simulations due to the critical role of subtropical cloud reflectivity?
    a) How does Cryogenian subtropical cloud reflectivity compare among three GCMs with different treatment of cloud microphysical processes?
    b) Can differences in Cryogenian low-level mixed-phase cloud abundance between GCMs be explained by the large-scale atmospheric state and the synoptic conditions?
    c) How does explicitly resolving moist convection impact Cryogenian subtropical cloud reflectivity?
    d) How do high concentrations of ice nucleating particles impact Cryogenian subtropical cloud reflectivity?

The answers to the research questions are organized in two chapters. We answer research question 1 and the corresponding sub-questions in chapter 5 and research question 2 and the corresponding sub-questions in chapter 6.

4. Three-dimensional Atmospheric Models and Simulations

We apply three-dimensional atmospheric models ranging from coarse-scale general circulation models (GCMs) with horizontal grid spacings on the order of hundreds of kilometers to a large-eddy model with a grid spacing of several hundred meters. The GCMs that we use to conduct global simulations are the Community Atmosphere Model (CAM) and the ICOsahedral Nonhydrostatic atmosphere model (ICON) in climate mode (ICON-AES: Atmosphere in the Earth System) and in numerical weather prediction mode (ICON-NWP) (Collins et al., 2004; Giorgetta et al., 2018; Zängl et al., 2015). For global and local simulations ranging from horizontal grid spacings of 10 km to 300 m we apply ICON-NWP and the ICON large-eddy model (ICON-LEM) (Zängl et al., 2015; Dipankar et al., 2015; Heinze et al., 2017; Stevens et al., 2020).

In this chapter we provide a description of the applied three-dimensional atmospheric models and the conducted simulations. We first describe general aspects of these models in sections 4.1 and 4.2. We further describe the parameterizations of the sub-grid scale physical processes that are not explicitly represented in the models in section 4.3. Finally, we describe how we apply the atmospheric models in order to map bifurcation diagrams (section 4.4) and to study the intensity of subtropical cloud reflectivity in a Jormungand-waterbelt climate (section 4.5). All simulations were conducted on the computing cluster Mistral hosted at the German Climate Computing Center (DKRZ).

4.1. The Community Atmosphere Model

We apply the Community Atmosphere Model in version 3.1 (in the following referred to as CAM) developed by the National Center for Atmospheric Research, Boulder, Colorado. We apply CAM in this specific version because CAM was successfully applied to demonstrate the Jormungand hypothesis in Abbot et al. (2011). We first provide a general description of CAM based on Collins et al. (2004) and afterwards describe a newly implemented modification of CAM for the local suppression of cloud radiative effects.

4.1.1. General description

CAM is based on the Eulerian hydrodynamic equations formulated in spherical coordinates using the assumption of hydrostatic equilibrium. This set of equations consists of the prognostic equations describing the conservation of mass, horizontal momentum, thermal energy, and equations for tracer transport. These equations are complemented by the equation of state for moist air and the hydrostatic assumption.

CAM separates the calculation of dynamics, i.e. the time integration of the hydrodynamic equations, from the calculation of parameterized sub-grid scale physical processes. The impact of the sub-grid scale physical processes is included in the hydrodynamic equations via time tendencies, which act as forcing terms.

We apply CAM with an Eulerian spectral dynamical core. This requires the variables to be transformed between the physical grid-point space spanned by space and time and the spectral space spanned by wave numbers. Transformations between spectral and physical space are done using Fast-Fourier-Transformations. Each time-integration step starts with the calculation of the nonlinear terms in the physical space. Afterwards the nonlinear terms are transformed to spectral space using Gaussian quadrature. In the spectral space the spectral coefficients of the truncated series of spherical harmonic functions representing the prognostic variables are calculated for the next time step. The prognostic variables are updated in spectral space and then are transformed back to physical space. Afterwards adjustments of horizontal diffusion, mass and energy are performed. Finally, tracer transport is calculated.

Dynamics and physics parameterizations are evolved in a process split manner. This means that the dynamical core and the physics parameterizations are both updated based on the same past model state. The physical parameterizations are calculated in the physical grid-point space. Among the parameterizations a time-split, i.e., sequential update of the model variables is performed. The parameterizations are called in the following order: 1) moist processes, involving penetrative convection, shallow convection, and large-scale non-convective condensation, 2) the representation of clouds, 3) the parameterization of radiative energy transfer, 4) surface processes, and finally 5) turbulent mixing. The physical parameterizations are described in section 4.3.

4.1.2. Local suppression of cloud radiative effects: CAM partial COOKIE

This section is adapted from Braun et al. (2022a).
©The Authors.

We implement a modification of CAM, to locally suppress cloud-radiative effects (CRE). We do so by setting cloud cover to zero when calling the radiation scheme, inspired by the Clouds On-Off Klimate Intercomparison Experiment (COOKIE) (Stevens et al., 2012). This intervention is limited to the radiation scheme, and clouds, latent heating and precipitation can still form. Specifically, we disable CRE in between 10° to 14° latitude in both hemispheres at all longitudes on the model levels 22 to 26, which corresponds to the lower troposphere. We refer to these simulations as CAM partial COOKIE (pCOOKIE).

4.2. The ICOsahedral Nonhydrostatic model

The ICOsahedral Non-hydrostatic (ICON) model is jointly developed by the German Weather Service, the Max Planck Institute for Meteorology, the German Climate Computing Center (DKRZ), and the department of meteorology and climate research (IMK) at the Karlsruhe Institute of Technology (KIT). We apply ICON across a wide range of horizontal grid spacings. Therefore, we here provide a general description of ICON based on Zängl et al. (2015) and further describe how to conduct ICON simulations on local subdomains based on Prill et al. (2020).

4.2.1. General description

ICON consists of a dynamical core accompanied by packages of physical parameterizations that are designed for the purposes of long-term climate simulations (ICON-AES), numerical weather prediction (ICON-NWP) and large-eddy simulations (ICON-LEM). One major benefit of ICON is the possibility to apply the same dynamical core across a wide range of horizontal grid spacings ranging from the upper mesoscale of $\mathcal{O}$(>100 km) to the microscale of $\mathcal{O}$(10 m). This flexibility is based on successive grid refinement of ICON's icosahedral-triangular grid along with the possibility to simulate local subdomains.

The dynamical core of ICON is based on the fully compressible Navier Stokes equations using the shallow atmosphere approximation. The prognostic variables are the horizontal velocity component normal to the triangle edges v_n, the vertical velocity component w, the density of air ρ, and the virtual potential temperature as recommended by Gassmann and Herzog (2008). The horizontal velocity component parallel to triangle edges v_t is reconstructed using vector radial basis functions (Wan et al., 2013). Pressure is related to density and temperature through the ideal gas law, which considers moist air.

The basic shape of ICON's grid is an icosahedron projected onto a sphere resulting in 20 equilateral and equally sized triangles. Finer grids are obtained in two steps, referred to as root division (termed Rn) and bisection (termed Bk). In the root division step the edges of the triangles are divided into n equal segments. Connecting the created edge points by great-circle arcs yields n^2 triangles within each original triangle. In the bisection step, a recursive subdivision into 4 smaller triangles is performed k times. A specific grid is fully defined by RnBk and the orientation of the basic icosahedron. The number of grid cells n_c is determined by $n_c = 20n^2 4^k$. The nominal grid spacing Δx can be defined as the square root of the average cell area.

$$\Delta x = \sqrt{\frac{4\pi r_E^2}{n_c}} = \sqrt{\frac{\pi}{5}}\frac{r_E}{n2^k} \tag{4.1}$$

Here r_E is the Earth radius.

The spatial discretization of the equations is based on finite volume and finite difference schemes (Wan et al., 2013). Horizontally, the equations are discretized using a staggered configuration. Scalar variables are defined at the cell circumcentre and the edge-normal horizontal velocity component is defined at the midpoints of the triangle edges. The vertical discretization is formulated in a generalized height-based system, which applies geometric altitude as the vertical dimension (Prill et al., 2020). Vertical velocity is defined in the center of the top and bottom triangle of a grid cell. These locations are termed half levels. All other variables are defined on full levels, i.e., located vertically in the middle between half levels (Prill et al., 2020). The definition of velocities at the surface centers together with a finite volume scheme mathematically allows precise mass and tracer conservation. The temporal discretization is done using a two-time-level predictor-corrector scheme.

ICON applies time splitting between the dynamical core and the other model components. These components comprise physical parameterizations of atmospheric processes, advection of hydrometeors and aerosols, and numerical horizontal diffusion. The dynamical core integrates the prognostic equations over 5 time steps before the current atmospheric state is passed on to the other model components.

The physical parameterizations are further divided into fast physics and slow physics. Slow physics parameterizations are called less frequently than fast physics parameterizations. Therefore, slow physics parameterizations do not update the prognostic variables directly, but provide time tendencies that are incorporated as forcing terms in the prognostic equations. Fast physical processes are surface mass and heat exchange, turbulent transport, saturation adjustment and cloud microphysical processes. Slow physical processes are cloud cover, radiation, moist convection, and non-orographic gravity wave drag. The details of the physical parameterizations are provided in section 4.3.

4.2.2. Simulations on local subdomains

ICON provides two methods for conducting simulations on local subdomains. First, ICON allows to create local subdomains, so-called nests, with increased horizontal grid spacing within a larger subdomain. Second, ICON allows to run simulations in limited area mode (LAM). The nesting and LAM methods can also be combined.

Nesting is done using a multi-grid approach. This approach overlays an additional domain with reduced horizontal grid spacing (termed child) on a subset of a domain with a coarser grid spacing (termed parent). The grid of the child domain is derived by a single bisection step performed on the parent grid, i.e., one triangle on the parent grid corresponds to four triangles on the child grid. Accordingly, the time step for the calculation on the child domain is reduced by a factor of 2. Multiple nests can be used simultaneously. The child domain(s) can be switched on and off at any point during a simulation. ICON allows for one-way and two-way nesting. We apply one-way nesting, which does only consider information transfer from the parent to the child domain. Information is transferred at every time step of the parent domain via the lateral boundaries of the child domain.

Running ICON in LAM also requires to provide lateral boundary conditions on the LAM-grid (termed child). However, lateral boundary conditions in this case are obtained by an independently run previous simulation, which is usually conducted on a coarser grid (termed parent). The simulations on the parent and child grid may differ regarding their physical parameterizations. Furthermore, the update intervals of the lateral boundary conditions for LAM-simulations are usually considerably larger compared to nesting. In between the update intervals of the lateral boundary conditions data is linearly interpolated. Using ICON in LAM allows the parent and child grid to differ in vertical extent and resolution. Moreover, the grid spacing ratio between parent and child grid may exceed 2 but is recommended to be below 5. Boundary conditions for a LAM-simulation can also be derived from a previous LAM-simulation.

Both approaches require to pass information from the parent grid to the child grid. This is done using a boundary interpolation zone, which is fixed to 4 rows of grid cells. The boundary interpolation zone is the outermost layer of the child domain. Concerning the child domain, the boundary interpolation zone is purely diagnostic. Interpolation from the parent to the child grid is done during the simulation runs for nesting and before the simulation runs for LAM-simulations. The boundary interpolation zone encloses a nudging zone. The nudging zone is required to prevent artificial reflection of acoustic waves at the lateral boundaries. Within the nudging zone, a prognostic integration is performed but a nudging update is imposed, which nudges the prognostic variables towards the model state in the boundary interpolation zone. We apply the recommended width of the nudging zone, which is 10 rows of grid cells.

We use ICON-NWP and ICON-LEM in LAM with online one-way nesting to conduct ICON-LEM simulations that are driven by a realistically evolving large-scale climatic and synoptic state as described in section 4.5.

4.3. Physical parameterizations

We here describe the physical parameterization packages applied in our CAM and ICON simulations. These packages comprise parameterizations for the ocean and sea ice (section 4.3.1), turbulent atmospheric transport (section 4.3.2), moist convection (section 4.3.3), non-orographic gravity wave drag (section 4.3.4), cloud microphysical processes (section 4.3.5), cloud cover (section 4.3.6), and radiative energy transfer (section 4.3.7). We provide more detailed descriptions associated with the parameterizations of sub-grid scale atmospheric flow, i.e., turbulent transport and moist convection, as well as cloud microphysical processes, because we focus on these parameterizations in our analysis of the simulation results. Our descriptions are organized as follows. We describe the parameterization packages for a specific physical process for all models applied in this work. After describing the parameterization packages for one physical process we briefly point out the implications of applying the parameterizations in our simulations. The descriptions in this section are based on Collins et al. (2004) for CAM, Giorgetta et al. (2013) and Giorgetta et al. (2018) for ICON-AES, Prill et al. (2020) for ICON-NWP, and Dipankar et al. (2015) and Prill et al. (2020) for ICON-LEM.

4.3.1. Surface: ocean and sea ice

Since we apply aquaplanet setups in our simulations, the lower boundary conditions of the atmosphere are determined by the ocean and sea-ice surfaces. Ocean and sea ice determine the moisture supply at the surface and act as a reservoir for thermal energy. Moreover, sea ice and snow deposited on it, are the core component of the sea-ice albedo feedback.

The uppermost ocean layer can be considered as well mixed due to stirring by wind, leading to small vertical gradients of temperature and salinity. This layer is referred to as mixed layer and can be up to a few hundred meters deep (Wallace and Hobbs, 2006). The mixed layer separates the atmosphere from the deeper ocean layers and the corresponding oceanic circulation patterns. Therefore, the mixed layer accounts for the quick adjustment of the ice-ocean system to changes in the atmospheric forcing. Adjustment times of a 50 m mixed-layer ocean are on the order of ten years without sea-ice formation (Woelfle et al., 2015) but may be on the order of a century if considering the ice-albedo feedback (Mengel et al., 1988). We apply CAM and ICON-AES with thermodynamic mixed-layer ocean models of 50 m depth without ocean heat transport and neglect sea-ice dynamics. This is the same setup as applied by Abbot et al. (2011), which led to the discovery of the Jormungand-waterbelt state.

CAM

In CAM the formulation for the ice-free ocean mixed-layer model is taken from Hansen et al. (1984). The energy exchange of the ocean with the atmosphere is determined by the absorbed shortwave radiation, incoming and outgoing longwave radiation, as well as latent and sensible heat fluxes from the ocean to the atmosphere. These energy fluxes determine the temperature change of the ocean, which is considered to exhibit a constant heat capacity of 3930 $\mathrm{Jkg^{-1}K^{-1}}$ and density of 1026 $\mathrm{kgm^{-3}}$. The ocean model is extended to allow for fractional sea-ice cover.

CAM applies a thermodynamic sea-ice model, which is adopted from the Community Sea Ice Model (CSIM) as described in detail in Briegleb et al. (2002). The sea-ice model consists of a snow layer and multiple ice layers. Therefore, it allows for internal heat storage within sea ice.

Deposition of snow is treated explicitly, which allows us to interactively simulate the strong albedo gradient arising from the transition of snow-covered to bare sea ice in the subtropical region. In CAM surface albedos are specified in two wavebands and for direct and diffuse radiation. Furthermore, albedo values are specified for cold and warm sea ice and snow, i.e., for surface temperature $T \leq -1$ °C and $T = 0$ °C. In between albedo values are linearly interpolated (Collins et al., 2004). The cold bare sea-ice broadband albedo is estimated to be ~ 0.45 and the cold snow-covered sea-ice broadband albedo to be ~ 0.79 (Abbot et al., 2011). The warm broadband albedo values are estimated to be 0.38 for bare sea ice and 0.66 for snow-covered sea ice under the assumption that 40 % of solar radiation is in the visible spectrum (Abbot et al., 2011).

ICON-AES

This section is adapted from Braun et al. (2022a).
©The Authors.

In ICON-AES the energy exchange of the mixed-layer ocean with the atmosphere comprises shortwave radiation, incoming and outgoing longwave radiation, as well as latent and sensible heat fluxes from the ocean to the atmosphere similar as in CAM. The mixed-layer ocean has a constant heat capacity of 3994 $\mathrm{Jkg^{-1}K^{-1}}$ and density of 1025 $\mathrm{kgm^{-3}}$.

We implement a link between the thermodynamic mixed-layer ocean with a sea-ice scheme by Semtner (1976) in ICON-AES. The Semtner sea-ice scheme is a 0-layer scheme, which does not account for heat storage within the ice. Sea ice forms if $T < T_f = -1.9$ °C, i.e., the freezing point of water at a salinity of 35 psu (Fujino et al., 1974). The transformation of ice-free ocean to sea ice requires the formation of a sea-ice layer of a minimum thickness $h_{i,min} = 0.05$ m. If $T < T_f$ but T is still too high to form an ice layer of the thickness $h_{i,min}$, T is set to T_f and a residual heat flux corresponding to the difference $T - T_f$ is calculated. The residual flux is added to the energy balance of the mixed-layer ocean during the next model time step.

Similar to CAM, ICON-AES keeps track of snow deposited on sea ice. We modify the ice-albedo parameterization in ICON-AES to reproduce the albedo values used in the GCM simulations of Abbot et al. (2011). We set the albedo of bare sea ice and snow to 0.45 and 0.79, respectively, and the warm albedo of bare sea ice and snow to 0.38 and 0.66, respectively. For the temperature range between -1 °C and 0 °C, we implement a linear interpolation between the cold and warm albedo values.

ICON-NWP and ICON-LEM

This section is adapted from Braun et al. (2022b).

©American Meteorological Society. Used with permission. This preliminary version has been accepted for publication in the Journal of Climate and may be fully cited. The final typeset copyedited article will replace the EOR when it is published.

In ICON-NWP and ICON-LEM we prescribe sea surface temperatures (SSTs) and sea ice cover (SIC). In regions covered by sea ice, surface temperatures are calculated by the sea-ice scheme described in Mironov et al. (2012). The sea-ice scheme assumes a fixed shape of the temperature profile within the ice layer, which determines the heat budget of the ice layer. Snow deposition onto sea ice is not considered explicitly. Therefore we prescribe a high surface albedo (0.66 to 0.79) in the extratropics, i.e., for latitudes beyond 18° latitude, and a low surface albedo (0.38 to 0.45) in the subtropical region, i.e., for latitudes within 18° latitude. We use the same temperature dependent albedo values as for ICON-AES.

Implications of applying an idealized aquaplanet setup

The idealized aquaplanet setup allows us to focus our analysis on the ice-albedo feedback, which constitutes the core of the Jormungand hypothesis. Furthermore, we can directly compare our results to Abbot et al. (2011) because they used the same setup. Since we do not apply ocean dynamics and heat transport, our simulations reach equilibrium states within a few decades to a century. For the ICON-NWP and

ICON-LEM simulations with prescribed SSTs and SIC the equilibration times are much shorter because spinup processes are limited to the atmosphere. This allows us to conduct much shorter simulations in ICON-NWP and ICON-LEM.

4.3.2. Turbulent transport

In this section we first provide a brief general overview of turbulent motion within the atmosphere based on Wallace and Hobbs (2006) to outline the different effects of turbulent motion. Afterwards we provide a description of turbulent transport in the applied atmospheric models.

Turbulent motion within the atmosphere occurs over a wide range of length and time scales and generally acts to reduce instability. Atmospheric instability may be of mechanical, thermal or inertial origin. Mechanical generation of turbulence is caused by shear in the mean flow. Shear arises from frictional drag near a surface or is caused by obstacles. Turbulent transport of momentum, heat and moisture due to shear is usually taken care of in turbulence schemes. We describe the turbulence schemes used in the applied atmospheric models later in this section. Thermal generation of turbulence is driven by buoyancy of warm air parcels in a colder environment and is also referred to as convective turbulence. Convective turbulent plumes may exhibit a cumulus cloud at their top if they exhibit sufficient moisture. Since clouds are an important feature of Earth's atmosphere, convective turbulence is usually considered in separate moist convection parameterizations, described in section 4.3.3. Inertial generation of turbulence is a special case of shear induced turbulence, for which shear is induced by larger eddies that fall apart into smaller eddies. In this case, turbulence acts to dissipate larger eddies. At the smallest turbulent scales, on the order of molecules, turbulence dissipates kinetic energy to thermal energy. The dissipation of kinetic energy within the atmosphere is, e.g., taken care of in parameterizations of non-orographic gravity wave drag, described in section 4.3.4.

The appropriate parameterization of the effects of turbulence strongly depends on the resolved length scales of the applied model. We provide a brief general discussion of applying the above parameterizations after the overview of the applied non-orographic gravity wave drag parameterizations in this chapter. We further provide more specific discussions of applying the convection parameterizations at different resolved length scales in section 6.2 along with our discussion of the simulation results. We here continue with a description of the turbulent transport parameterizations in the applied atmospheric models.

Turbulent transport reduces gradients of momentum, energy, moisture, gases, and particles. Turbulent transport schemes account for turbulent vertical transport within the free troposphere and the atmospheric boundary layer (ABL). In the ABL turbulent transport is particularly important. The ABL consists of the bottom 500 to 3000 m of the atmosphere that are strongly influenced by energy and moisture exchange with the surface (Jacobson, 2005). Atmosphere-surface exchange processes are determined by the vertical turbulent fluxes of momentum, sensible heat and moisture.

A deterministic simulation of turbulence on relevant time scales is not feasible due to the high nonlinearity of turbulent flows (Jacobson, 2005). Therefore turbulence is usually described by statistical approaches. To do so, the prognostic variables are considered to be separated into a mean component and a fluctuation around the mean. The equations describing atmospheric motion are then filtered using a spatial and/or temporal filter. The spatial filter width is usually considered to be at the size of the grid spacing. Hence, the mean flow is assumed to be represented by the grid-scale variables. This approach introduces additional free variables in the form of nonlinear fluctuation-terms that describe the sub-grid scale turbulent transport. Hence, statistical approaches yield unclosed sets of equations that need to be closed using closure assumptions.

CAM

The turbulence scheme in CAM consists of two components: First, a parameterization of vertical diffusion in the free atmosphere and second, an ABL parameterization described in Holtslag and Boville (1993).

Vertical diffusion in the free atmosphere is closed by a local diffusion approach. This means that the vertical turbulent flux of a quantity is assumed to be proportional to the local vertical gradient of the quantity and the turbulent diffusivity. In order to determine the turbulent diffusivity a discrimination between stable and unstable conditions based on the Richardson number is applied.

The ABL parameterization determines the turbulent exchange at the surface and is based on a non-local diffusion approach. This means, that additionally to the local turbulent flux a non-local term is considered, which parameterizes counter-gradient turbulent fluxes. The non-local term allows to apply turbulent properties that are characteristic for the ABL. This requires an estimate of the ABL depth based on the bulk-Richardson number.

ICON-AES

The turbulence scheme implemented in ICON-AES also considers vertical diffusive transport by sub-grid scale turbulent motion. It is based on a prognostic budget equation for total turbulent energy, which was developed by Mauritsen et al. (2007) for stably stratified conditions and was extended by Angevine et al. (2010) for convectively unstable situations. Total turbulent energy is the sum of turbulent kinetic energy (TKE) and turbulent potential energy (Mauritsen and Svensson, 2007). The latter is proportional to fluctuations of potential temperature and atmospheric stability (Mauritsen and Svensson, 2007). The budget equation for total turbulent energy itself and the associated closure assumptions depend on atmospheric stability, which is measured by the Richardson number and empirical stability functions (Mauritsen and Svensson, 2007).

The same parameterization is also applied within the ABL. Yet, in the upper part of the ABL below the capping inversion, the budget equation is determined by atmospheric stability and a mixing length derived using empirical constants (Mauritsen et al., 2007). At the lowermost model layer a logarithmic vertical profile of wind and temperature is assumed.

ICON-NWP

The turbulence scheme applied in ICON-NWP is based on Raschendorfer (2001). It consists of two components that account for the free troposphere (TURBDIFF) and the surface layer (TURBTRAN).

TURBDIFF accounts for vertical diffusion based on a prognostic equation of TKE assuming quasi-isotropic turbulence. TURBDIFF is a moist turbulence scheme, i.e., TURBDIFF considers sub-grid scale effects of clouds via a statistical cloud scheme by Sommeria and Deardorff (1977). The scheme assumes the production of TKE to be caused by sub-grid scale thermal circulations. A second order closure for the wind components, virtual potential temperature, specific humidity, and cloud tracers is applied. This means that associated nonlinear turbulent fluctuation-terms are treated as diagnostic source terms in the prognostic equation for TKE. The scheme is applicable within and above the boundary layer because the sub-grid scale energy spectrum is separated into turbulent and non-turbulent contributions.

TURBTRAN is applied in the lowermost model layer and considers the effect of turbulent transport from the surface into the atmosphere via transfer resistances.

ICON-LEM

ICON-LEM considers turbulent transport via a three-dimensional Smagorinsky diffusion scheme based on Smagorinsky (1963) and Lilly (1962).

In ICON-LEM, Favre filtering is applied and leads to nonlinear turbulent transport terms in the conservation equations for momentum, thermal energy, moisture and atmospheric tracers. In the momentum conservation equations these terms represent the divergence of the sub-grid scale stress tensor. The system is closed by considering sub-grid scale turbulence to cause additional grid-scale viscosity via the so-called eddy viscosity. The value of eddy viscosity is a function of the applied Favre-filter width, which is a function of the grid spacing, and considers a stability correction factor suggested by Lilly (1962).

The turbulent transport terms in the energy, moisture and tracer conservation equations are parameterized in a similar manner. Here, instead of eddy viscosity, the eddy diffusivity coefficient is applied. Eddy diffusivity is assumed to be related to eddy viscosity through the turbulent Prandtl number, i.e. the ratio of kinematic viscosity to thermal diffusivity. The eddy diffusivity coefficient is assumed to be equal for thermal energy, moisture and tracers.

Parameterizations for the turbulent surface fluxes are based on the drag-law formulation (Dipankar et al., 2015). The required bulk-aerodynamical transfer coefficient for turbulent mass and heat exchange at the surface is parameterized following Louis (1979).

4.3.3. Moist convection

Moist convection acts to stabilize unstable stratified atmospheric conditions (Wallace and Hobbs, 2006). Moist convection is associated with cloud formation through condensation and is thus amplified by latent heat release. An important process during convection is the mixing of cloudy air with the surrounding environment via entrainment and detrainment. Moist convection parameterizations estimate the effect of sub-grid scale moist convection on and based on the grid-scale model state.

CAM

The convection scheme applied in CAM separates convection into deep convection and shallow or mid-level convection.

The deep convection parameterization was developed by Zhang and McFarlane (1995). It assumes the presence of an ensemble of updrafts if the atmosphere is conditionally unstable in the lower troposphere, i.e., convective available potential energy (CAPE) is available. The height, up to which the updrafts penetrate into the atmosphere, is determined by budget equations for the dry static energy, the water vapor mixing ratio, the moist static energy, and cloud liquid water. These equations consider entrainment and detrainment rates that are determined based on the moist static energy contained in the plume of updrafts. To close this set of equations the cloud base mass flux is related to CAPE. The deep convection parameterization considers the vertical transport of tracers.

Moist adiabatically unstable conditions not covered by the deep convection parameterization are treated via the combined shallow or middle tropospheric moist convection parameterization. This parameterization is based on a three-layer non-entraining cloud model considering the budget equations for dry static energy and specific humidity. The model estimates a detrainment parameter, based on which the mass flux at cloud base can be determined. This mass flux is applied for the vertical transport of atmospheric tracers.

ICON-AES

In ICON-AES convection is separated into deep, mid-level and shallow convection based on the mass flux scheme by Tiedtke (1989) with updates from Nordeng (1994). Convective motion is described by budget equations for a representative plume, which consider entrainment and detrainment. The set of equations is closed by applying closure assumptions concerning the cloud base mass flux, which determines the intensity of convective motion. Depending on the atmospheric level that convective motion penetrates into, different closure assumptions are applied. The closure for deep convection is based on CAPE. The closure for mid-level convection is based on the grid-scale vertical velocity at the cloud base. The closure for shallow convection is based on the moisture convergence within the ABL.

ICON-NWP

In ICON-NWP the mass-flux convection scheme by Tiedtke (1989) and Bechtold et al. (2008) separates convection into deep, mid-level and shallow convection. The scheme operates in three steps. In a first step it is determined, whether and which type of convection is expected to occur based on the grid-scale atmospheric state. In a second step a cloud model is applied to determine the convection-related tendencies of heat, moisture, momentum. The cloud model represents an ascending plume and the interactions with its environment via entrainment and detrainment. In a third step a closure assumption is applied to determine, how much CAPE is transformed into kinetic energy. The larger the amount of energy converted, the stronger the convection and the larger the generated amount of precipitation. The closure assumptions applied in the convection scheme are similar to the convection parameterization in ICON-AES.

ICON-LEM

In ICON-LEM convection is a grid scale process. Hence, no convection parameterization is applied.

4.3.4. Non-orographic gravity wave drag

Gravity waves arise from the vertical oscillation of air parcels, which is triggered by features of the atmospheric flow such as fronts, convection, and the jet streams (Prill et al., 2020). The drag arising from gravity waves exerted on the atmospheric background flow in the middle and upper atmosphere is assumed to be significant across the entire spectrum of wavelengths (Prill et al., 2020).

CAM

To our knowledge CAM does not apply a parameterization for non-orographic gravity wave drag.

ICON-AES

The non-orographic gravity wave parameterization applied in ICON-AES is based on Hines (1997). It considers constant, globally uniform and isotropic gravity wave sources at around 680 hPa.

ICON-NWP

The Orr-Ern-Bechtold-scheme used in ICON-NWP for considering the drag of non-orographically induced gravity waves is described in Orr et al. (2010). The scheme assumes a constant source of gravity waves in a hydrostatic, non-rotational atmosphere. The parameters have been tuned according to Ern et al. (2006).

ICON-LEM

In ICON-LEM, gravity waves are assumed to be explicitly resolved.

Implications of applying parameterizations for turbulent transport, moist convection and non-orographic gravity wave drag

The parameterizations for atmospheric turbulent transport, moist convection, and non-orographic gravity wave drag applied in CAM, ICON-AES, and ICON-NWP were developed using empirical relations derived from present-day climate conditions. Thus, they may not be valid under the extremely different conditions occurring in our simulations of Cryogenian climate. In contrast, applying the more generalized formulation of the three-dimensional Smagorinsky turbulence scheme and explicitly simulating convective-scale atmosphere dynamics in ICON-LEM does not include a priori assumptions based on a specific climate state. Therefore, we consider ICON-LEM to be able to flexibly adjust to the cold waterbelt climate in terms of atmosphere dynamics.

4.3.5. Cloud microphysical processes

Clouds consist of numerous small particles, namely liquid cloud droplets and solid ice crystals. The bulk optical properties and the life-time of clouds are determined by the interactions of these particles. The interactions of these particles are furthermore impacted by atmospheric motion and aerosols. The entirety of these interactions is usually referred to as cloud microphysical processes. We here provide a brief summary of cloud microphysical processes with a focus on mixed-phase clouds and the formation of liquid and ice particles. Afterwards we describe how the applied atmospheric models incorporate these effects in the associated cloud microphysical schemes.

Mixed-phase clouds represent a three-phase system that consists of water vapor, ice particles, and supercooled liquid droplets (Korolev et al., 2017). Within the atmosphere the three phases can coexist at air temperatures between 0 °C and -38 °C. A characteristic feature of mixed-phase clouds are persistent narrow layers of supercooled liquid on top of the mixed-phase clouds (Korolev et al., 2017). Because cloud droplets are considerably smaller than ice crystals their bulk effect on cloud reflectivity is much higher than that of ice crystals. Yet, the role of ice crystals in supercooled clouds is important because the ice phase can influence the amount of supercooled liquid via the Wegener-Bergeron-Findeisen (WBF) process (Korolev et al., 2017).

The WBF process considers that if the vapour pressure is between the saturation vapor pressure over ice and the saturation vapor pressure over water, supercooled liquid is consumed at the expense of growing ice crystals (Storelvmo and Tan, 2015). Thus, the conversion of cloud liquid to ice is dependent on the intensity of updrafts, which sets the saturation pressure via adiabatic cooling. The efficiency of the WBF process further strongly depends on the number of ice crystals and in turn on the abundance of ice nucleating particles (INPs), onto which water vapor can condense. Thus the formation of cloud droplets and ice crystals are important processes regarding the reflectivity of mixed-phase clouds.

At supersaturations occuring in Earth's atmosphere, cloud droplets form via heterogeneous nucleation only and thus cloud droplet formation relies on the presence of condensation nuclei (CN; Wallace and Hobbs (2006)). Most commonly, supersaturation is a result of expansion of air and associated adiabatic cooling in updrafts. If sufficiently high supersaturation is reached, water vapor condenses onto CN. The number of CN that are activated to cloud condensation nuclei (CCN) depends on the properties of the CCN, such as size and composition, and increases with increasing supersaturation, i.e., with stronger updrafts. Once formed, cloud droplets can grow by collision with other droplets. The process of small droplets growing via collision to larger droplets is called accretion and can further lead to the formation of raindrops via autoconversion.

Ice crystal formation happens via homogeneous and heterogeneous ice nucleation, also referred to as primary ice production. Ice crystal formation in cold clouds at temperatures below -50 °C predominantly happens via homogeneous ice nucleation. At temperatures slightly below -38 °C and for moderate supersaturation with respect to the ice phase (40 - 50 %), ice crystal formation may happen via heterogeneous and homogeneous nucleation (Kanji et al., 2017). At temperatures slightly below -38 °C and high supersaturation, homogeneous ice nucleation is dominant (Kanji et al., 2017).

Heterogeneous ice nucleation refers to the idea that an INP stabilizes a critical ice embryo. This lowers the energy barrier to form an ice crystal (Kanji et al., 2017). Heterogeneous ice nucleation can involve the formation of ice from the vapor or the liquid phase (Kanji et al., 2017). A common classification of nucleation processes are deposition ice nucleation, contact freezing, and immersion freezing. Deposition ice nucleation refers to the direct transition from vapor to ice by deposition onto a porous INP. During contact freezing an INP approaches the air–water interface of a supercooled droplet from either the outside (collision contact freezing) or the inside of a droplet (inside-out contact freezing). Immersion freezing describes an INP becoming immersed in a cloud droplet via activation of a CCN during cloud droplet formation, subsequent supercooling, and freezing of the supercooled droplet at sufficiently low temperatures. Heterogeneous ice nucleation is the only way for primary ice production above -38 °C, and therefore is important for mixed-phase cloud microphysical processes. More specifically, immersion freezing is suggested to be the most important ice formation mechanism in mixed-phase clouds (Kanji et al., 2017).

Besides heterogeneous ice nucleation the ice crystal number concentration in mixed-phase clouds is strongly impacted by secondary ice formation (Korolev et al., 2017). Well established processes of secondary ice production are rime splintering, which may be caused by riming of ice crystals with supercooled droplets, and crystal-crystal collision with subsequent fragmentation (Field et al., 2017). Secondary ice formation is considered as an explanation why ice crystal number concentrations can exceed INP concentrations by up to an order of 10^4 at -10 °C (Field et al., 2017; Hallett and Mossop, 1974).

In summary, the abundance of cloud droplets and ice crystals in mixed-phase clouds is determined by numerous entangled processes and the dynamic and thermodynamic environment. Particularly representing the partitioning of cloud condensate into the liquid and ice phase in microphysical schemes is challenging. The different approaches cover different levels of complexity as we outline in the following.

CAM

This section is based on Braun et al. (2022a).
©The Authors.

In CAM the evolution of cloud condensate is separated into a macroscale and a microscale component. The macroscale component is based on Zhang et al. (2003) and considers the conversion between water vapor and cloud condensate and the corresponding changes of air temperature.

The microscale component is the one-moment cloud microphysical scheme based on Rasch and Kristjánsson (1998). The scheme integrates prognostic equations for the mass of cloud liquid and ice considering grid scale processes, i.e., advection of cloud condensate, and sub-grid scale processes, i.e., convection and turbulence. The forcing exerted by these processes and the thermodynamic in-cloud conditions determine whether condensate evaporates or is converted to precipitation. Precipitation is considered to consist either of rain or snow and is treated purely diagnostic.

Basically, cloud liquid and ice are considered as independent quantities. Yet, liquid-ice partitioning is performed explicitly based on air temperature T_a at every microphysical model time step (Collins et al., 2004). x_i indicates the ice fraction within a cloud within the temperature range $T_{a,\min} = -40\,°\mathrm{C}$ to $T_{a,\max} = -10\,°\mathrm{C}$.

$$x_i = \frac{T_a - T_{a,\max}}{T_{a,\min} - T_{a,\max}},\ T_{a,\min} \leq T_a \leq T_{a,\max} \tag{4.2}$$

$x_i = 1$ for $T_a < T_{a,\min}$ and $x_i = 0$ for $T_a > T_{a,\max}$. Cloud liquid l and cloud ice I within each grid cell are calculated based on x_i from the previous total cloud condensate $(l' + I')$.

$$l = (l' + I')(1 - x_i) \tag{4.3}$$

$$I = (l' + I')x_i \tag{4.4}$$

After the explicit partitioning of cloud condensate, conversion rates from cloud liquid to rain and cloud ice to snow are calculated.

ICON-AES

This section is based on Braun et al. (2022a).
©The Authors.

In ICON-AES the evolution of cloud condensate is separated into a macroscale and a microscale component.

The macroscale component consists of the cloud cover scheme by Sundqvist et al. (1989) and determines the amount of condensate generated during cloud formation. The condensational growth of cloud droplets is considered to be proportional to cloud cover. Cloud cover is parameterized as a non-linear function of grid-mean relative humidity, if relative humidity exceeds a pressure dependent minimum threshold.

The microscale component is a one-moment microphysical scheme based on Lohmann and Roeckner (1996), which is described in Giorgetta et al. (2013). It considers prognostic equations for the mass of water vapor, cloud liquid and ice. Raindrops and snow are treated diagnostically.

The prognostic equations consider advection and diffusion of the three phases and phase transitions triggered by convection and turbulence. Furthermore, a wide range of phase specific conversion processes is considered, of which we list the most relevant here. Liquid may be converted to precipitation due to autoconversion or accretion of liquid by rain or snow. Ice may be converted to precipitation by aggregation and accretion by snow.

Liquid-to-ice conversion contains parameterizations for contact freezing of cloud liquid and temperature-dependent freezing rates. The latter cover three temperature regimes. First, homogeneous freezing of cloud liquid occurs instantly below air temperatures of -35 °C. Second, complete melting of cloud ice occurs above air temperatures of 0 °C. Third, in between -35 °C to 0 °C stochastic and heterogeneous freezing occurs.

Furthermore, conversion from the vapor phase directly to the ice phase by deposition is considered in addition to condensation if air temperatures either are below -35 °C, or are below 0 °C and the ratio of cloud ice to cloud liquid x_i exceeds a threshold $x_{i,thr}$. This can be considered as an idealized parameterization of the Wegener-Bergeron-Findeisen process (WBF). A higher $x_{i,thr}$ corresponds to a weaker WBF and favors the existence of cloud liquid, because more condensation instead of deposition takes place.

The microscale component also provides the temperature changes associated with phase changes between vapor, liquid and solid phase.

ICON-NWP and ICON-LEM

In ICON-NWP and ICON-LEM we apply the 2-moment scheme based on Seifert and Beheng (2006). This scheme predicts the mass and number density of cloud water, rain water, cloud ice, snow, graupel and hail using prognostic equations. Consequently, the mass and size of hydrometeors can vary independent from each other.

The scheme considers a comprehensive set of conversion rates, including CCN activation (Segal and Khain, 2006), heterogeneous and homogeneous ice nucleation (Hande et al., 2015; Phillips et al., 2008; Kärcher et al., 2006; Seifert and Beheng, 2006), particle growth and conversion to precipitation by selfcollection processes, particle-particle collisions, and riming with associated secondary ice formation via the Hallet-Mossop effect. These processes represent the most important processes within mixed-phase clouds (Seifert and Beheng, 2006). Furthermore, this scheme relates cloud microphysical processes directly to grid scale variables because no assumptions concerning sub-grid scale variability of vertical velocity are applied. This provides a direct coupling of dynamical and microphysical processes and omits parameterizations of sub-grid scale variability. Therefore, this scheme is recommended to be applied with grid spacings smaller than 3 km, because here convective updrafts can be considered to be explicitly resolved.

The temperature changes resulting from the phase transitions calculated in the microphysical scheme are calculated by the saturation adjustment as described in Prill et al. (2020).

Implications of applying cloud microphysical schemes

The magnitude of mixed-phase cloud reflectivity is largely determined by the amount of liquid water contained in mixed-phase clouds. As outlined above, the approaches to determine the amount of liquid water in mixed-phase clouds strongly differ and thus may yield substantially different results (McCoy et al., 2016). Although more complex modeling approaches yield higher flexibility in terms of buffering feedbacks (Stevens and Feingold, 2009), they are not necessarily more accurate. Thus, we find it important to apply a variety of cloud microphysical schemes and investigate how the different schemes play out under Cryogenian climate conditions.

4.3.6. Cloud cover

Clouds are typically much smaller than horizontal grid spacings applied in atmospheric models. Therefore cloud cover schemes assume a sub-grid distribution of clouds and provide fractional cloud cover within a grid cell. The assumed sub-grid distribution of clouds and cloud condensate is related to grid-scale variables. The sub-grid distribution of clouds is relevant for the radiative effect of clouds that is considered in the radiation scheme.

CAM

CAM applies a diagnostic cloud cover scheme based on Slingo (1987). The cloud cover scheme diagnoses cloud fraction within a grid cell based on relative humidity, atmospheric stability and the convective mass flux. Three types of clouds are considered. Low-level marine stratus are diagnosed according to an empirical relationship, which relates marine stratocumulus cloud fraction with the atmospheric stability in the lower troposphere (Klein and Hartmann, 1993). Convective cloud fraction is diagnosed based on the updraft mass flux calculated in the deep and shallow moist convection schemes (Xu and Krueger, 1991). Remaining cloud types are jointly considered to form if relative humidity exceeds a pressure dependent threshold. Cloud fraction increases with increasing relative humidity.

Multiple cloud types can occur within each grid box. The resulting total cloud cover in each grid box is determined by a maximum overlap assumption. Cloud condensate is assumed to be uniformly distributed within each grid box.

ICON-AES

ICON-AES applies a diagnostic cloud cover scheme following Sundqvist et al. (1989). If relative humidity exceeds a pressure dependent minimum threshold, the cloud cover in each grid box and on each vertical level is diagnosed based on relative humidity. A special treatment is performed for marine stratus under a low-level inversion (below $\sim$ 700 hPa) to facilitate cloud formation under these conditions. This allows for the formation of thin stratus clouds under an inversion caused by subsidence. Without this special treatment ICON-AES would not be able to capture marine stratus due to insufficient vertical resolution.

ICON-NWP

In ICON-NWP a diagnostic cloud cover scheme is applied (Prill et al., 2020). The scheme receives grid-scale cloud liquid, cloud ice, and water vapor as input variables and redistributes water mass among the three phases considering mass conservation of total water. The redistribution is based on sub-grid scale information from the turbulence scheme, the convection scheme and the cloud microphysical scheme. The turbulence scheme provides the sub-grid variability of water caused by turbulent motion. The convection scheme provides the intensity of detrainment in cloud anvils, which converts cloud ice and liquid into water vapor. The microphysical scheme provides the supersaturation with respect to the ice phase, which impacts vapor deposition onto ice crystals.

ICON-LEM

In ICON-LEM an all-or-nothing cloud cover scheme as described in Sommeria and Deardorff (1977) is applied. The grid spacing is assumed to be sufficiently small to explicitly account for cloud cover. Hence, a grid box is entirely covered by a cloud or exhibits clear-sky conditions.

Implications of applying cloud cover parameterizations

Similar to the parameterizations of turbulent atmospheric motion, the cloud cover parameterizations in CAM, ICON-AES, and ICON-NWP use a priori assumptions regarding the simulated climate state. The all-or-nothing cloud cover scheme used in ICON-LEM avoids these assumptions but requires relatively small grid spacings for an accurate representation of clouds. To not rely on the results of a single parameterization we consider it reasonable to apply different cloud cover parameterizations especially under conditions that considerably differ from the conditions found on present-day Earth.

4.3.7. Radiative energy transfer

Radiative energy transfer within the atmosphere is determined by the interaction of electromagnetic waves with atmospheric constituents, such as cloud droplets and ice crystals, gases, and aerosols. In Earth's atmosphere radiative energy transfer is a three-dimensional process involving scattering, reflection, absorption, and emission. All radiation schemes applied within this work are one-dimensional schemes that assume the atmosphere to consist of independent vertical columns, which is a common approximation in atmospheric models. Atmospheric radiation is usually considered to be separated into a shortwave solar spectrum, with a peak in transferred energy at wavelengths smaller than 4 μm, and a longwave terrestrial spectrum, with a peak in transferred energy at wavelengths larger than 4 μm (Wallace and Hobbs, 2006).

Radiation schemes calculate radiative fluxes within each atmospheric layer. Radiative heating rates can be derived from the divergence of the radiative fluxes. The here applied radiation schemes provide all-sky and clear-sky radiative fluxes for the shortwave and the longwave spectrum. From the difference of all-sky and clear-sky radiative fluxes we diagnose the shortwave and longwave cloud radiative effect.

CAM

The radiation scheme in CAM applies two separate components for the shortwave and the longwave spectrum.

The solution of the shortwave component is based on the δ-Eddington approximation by Joseph et al. (1976) and Coakley et al. (1983), which allows for a fast but accurate computation of monochromatic radiative fluxes. The solar spectrum is divided into 19 discrete spectral intervals, most of which are associated with specific atmospheric gases. Each atmospheric column is considered as a set of horizontally homogeneous layers, which represent a homogeneous combination of atmospheric constituents. Radiative interactions include gaseous absorption, molecular scattering, and scattering and absorption by cloud droplets. Multiple scattering between layers is considered.

A maximum-random cloud overlap assumption by Collins (2001) is applied. It assumes that clouds in adjacent layers are maximally overlapped. Groups of clouds that are separated by one or more cloud-free layers are assumed to randomly overlap. Over the ocean and sea ice the effective radius of cloud droplets is 14 μm. The effective radius of ice particles is a function of air temperature (Kristjánsson et al., 2000).

The longwave component is based on an absorptivity and emissivity formulation by Ramanathan and Downey (1986). It considers the three major absorbers H_2O, CO_2 and O_3 and the trace gases Methane, Nitrous Oxide, and CFCs. Longwave cloud emissivity is determined by assuming clouds to be gray bodies with emissivities that depend on the cloud water path, the partitioning of cloud water into the liquid and ice phase, and the effective radius of ice particles.

ICON-AES

ICON-AES applies the radiation scheme PSrad by Pincus and Stevens (2013) for the longwave and shortwave spectrum. The longwave spectrum is divided into 16 bands, ranging from wavelengths of 3 to 1,000 μm. The shortwave spectrum is also divided into 16 bands, ranging from wavenumbers of 0.2 to 12 μm. In the shortwave band multiple scattering between layers is considered.

The calculation of radiative energy transfer is done using the Rapid Radiation Transfer Model (RRTM) based on Mlawer et al. (1997). RRTM applies the correlated-k method, which provides radiation calculations at an accuracy comparable with line-by-line models but with considerably higher computational efficiency. The high efficiency is achieved by rearranging the spectral absorption coefficients k_a for each wave number interval in ascending order. This yields a smooth absorption function that can accurately be discretized. RRTM considers reflection, transmission and internal radiation sources in each grid-box and model layer.

A generalized Monte Carlo independent column approximation is applied to take into account cloud vertical overlap (Pincus et al., 2003). This allows for multiple potential realizations of the cloud field within each atmospheric column using a maximum-random cloud overlap assumption. Cloud optical properties were adapted from ECHAM6 and are prescribed based on look-up tables derived from Mie-calculations as described in Stevens et al. (2013).

ICON-NWP and ICON-LEM

ICON-NWP and ICON-LEM also apply the Rapid Radiation Transfer Model (RRTM). Here, the spectrum is divided into 30 spectral bands, with 16 bands in the longwave spectrum and 14 bands in the shortwave spectrum. Within each band the properties of the atmospheric constituents are defined.

An exponential-random cloud vertical overlap assumption based on Hogan and Illingworth (2000) is applied. It considers clouds that are separated by cloud-free layers to randomly overlap. The overlap of clouds extending over multiple vertical levels decreases exponentially with vertical distance.

Given the same amount of cloud water, clouds with high horizontal variability of water interact weaker with radiation than clouds with a homogeneous distribution of water. Cloud water largely determines the optical thickness of a cloud. The horizontal variability of optically thin and thick parts of clouds is taken into account by reducing the cloud optical depth by a cloud inhomogeneity factor of 0.8.

Cloud optical properties are based on Mie-calculations assuming spheres for cloud droplets and more complex geometries for ice crystals.

Implications of applying parameterizations of atmospheric energy transfer

The radiation schemes used in the atmospheric models applied in this work use different cloud overlap assumptions and optical properties for cloud droplets and ice crystals. Cloud overlap is determined by the shape and small-scale interaction of clouds, both of which are unknown for Cryogenian climate.

Therefore, we find it reasonable to apply the default parameterizations for cloud overlap. The optical properties of hydrometeors, i.e., cloud droplets and ice crystals, are determined by their size and shape. As outlined in section 4.3.5 the size and shape of hydrometeors is impacted by the abundance of CCN and INPs. Given our limited knowledge regarding Cryogenian aerosol conditions, we consider it as reasonable to use the default parameterizations for the size and shape of hydrometeors.

4.4. Simulation setups for mapping bifurcation diagrams and studying atmospheric processes in a waterbelt climate state

Parts of this section are adapted from Braun et al. (2022a).
©The Authors.

The geologically relevance of the Jormungand-waterbelt state can be determined based on bifurcation diagrams. In sections 2.2 and 2.4 we introduced bifurcation diagrams, which we calculated based on the one-dimensional energy balance model. In this section we describe the steps to obtain bifurcation diagrams using GCM simulations. These simulations also allow us to analyze the atmospheric circulation and clouds in a waterbelt climate. We first describe the default simulation setups in CAM and ICON-AES as well as the applied modifications. Afterwards we describe how we derive the bifurcation diagrams.

4.4.1. Simulation setups

Mapping bifurcation diagrams requires to estimate the positions of stable and unstable equilibria in a space spanned by global-mean ice-edge latitude vs. atmospheric CO_2 concentration. We search for these positions by conducting simulations with constant concentrations of atmospheric CO_2, in which the models drift towards the closest stable equilibrium state depending on the initial global-mean ice-edge latitude.

We apply CAM as described in Abbot et al. (2011) and Pierrehumbert et al. (2011), and ICON-AES based on Giorgetta et al. (2018), with modifications as given below. For all simulations we consider an idealized aquaplanet setup. We set the solar constant to 1285 Wm^{-2} and apply a circular Kepler orbit with zero eccentricity and an obliquity of 23.5° , following Abbot et al. (2011). Simulations are either initialized from ice-free states, stable waterbelt states or transient waterbelt states. We run simulations until either reaching a stable equilibrium state or until exhibiting a clear drift away from an unstable state. The evolution of the global-mean ice-edge latitude for all simulations conducted for mapping the bifurcation diagrams is given in Figs. A.1 and A.2. The corresponding labels also provide an overview of the initial global-mean ice-edge latitude.

CAM

We apply CAM without any aerosols. We apply modern levels of ozone and non-CO_2 greenhouse gases as described in Abbot et al. (2011) and Pierrehumbert et al. (2011).

We conduct CAM simulations with resolution T42, i.e., truncation in spectral space at order 42, which corresponds to a horizontal resolution in physical space of 64 latitudinal and 128 longitudinal grid points and an nominal horizontal grid spacing of 310 km. In the vertical direction CAM applies 26 pressure levels between 993 hPa and 3 hPa. For the analysis of CAM simulations we use monthly-mean zonal-mean profiles with a latitudinal resolution of 2.8125°.

CAM pCOOKIE - modified cloud radiation in CAM

We also investigate the specific impact of cloud-radiative effects by mapping an additional bifurcation diagram using the modified version CAM pCOOKIE as described in section 4.1.2.

ICON-AES

The version of ICON-AES applied within this thesis is based on version 1.3.00 as described by Giorgetta et al. (2018). We modify this version to simulate an aquaplanet climate with no continents and a thermodynamic mixed-layer ocean linked to a thermodynamic sea-ice scheme as further described in section 4.3.1.

In ICON-AES we do not consider any greenhouse gases, except CO_2, which has a constant and uniform concentration, and water vapour. Direct radiative effects of aerosols are set to zero. The ozone concentration is constant in time and taken from the aquaplanet simulations of Liang et al. (1997).

Since we simulate climate states that are much colder than in Giorgetta et al. (2018), we decrease the model height from 83 km to 72 km by removing the two top levels (from originally 47). This helps to avoid model instabilities in the lower stratosphere. Along with reducing the levels we adjust the stretch factor for the distribution of vertical levels from 0.9 to 0.949 to keep the distribution near the surface close to the the setup with 47 levels. However, some instabilities remain under high CO_2 concentrations and large ice cover. Therefore, if global ice cover exceeds about 20 % in the simulations, we also increase the Rayleigh damping of vertical velocity near the model top and decrease the model time step (Klemp et al., 2008; Zängl et al., 2015). This stabilizes the model, and we have verified that these modifications have a negligible impact on the simulated climates.

Specifically, starting from ice-free states we conduct simulations with a time step of 10 minutes and a Rayleigh damping coefficient of 0.1. Subsequently the model time step is reduced to 8 minutes and the Rayleigh damping coefficient is increased to 10 after the model first becomes unstable. If further instabilities occur, the time step is reduced to 6 minutes, and we have not seen further model crashes then. The ICON-AES simulation at 1500 ppmv CO_2 that is initiated from an ice-free state runs into a Snowball state without any instabilities with an 8 minute time step. Yet, for consistency we conduct the branchedoff simulations with increased atmospheric CO_2 with a time step of 6 minutes. Thus, all simulations in the temperate climate state use a time step of 10 minutes and a Rayleigh damping coefficient of 0.1, and all simulations in the waterbelt climate state use a time step of 6 minutes and a Rayleigh damping coefficient of 10.

We conduct ICON-AES simulations on a R2B4 grid ($\approx$ 160 km nominal grid spacing). For the analysis of ICON-AES simulations we use monthly-mean zonal-mean profiles with a latitudinal resolution of 1.875°. We regrid 3D output from ICON-AES to the same pressure levels used in CAM.

ICON-AES WBF - modified cloud microphysical processes in ICON-AES

We investigate specific impacts of the WBF process by mapping an additional bifurcation diagram using ICON-AES with decreased efficiency of the WBF process (ICON-AES WBF). We do so by increasing $x_{i,thr}$ from its default value of $5 \cdot 10^{-6}$ kgm^{-3} to the upper limit of $5 \cdot 10^{-5}$ kgm^{-3} as suggested in Mauritsen and Roeckner (2020) (see section 4.3.5).

4.4.2. Mapping bifurcation diagrams from general circulation model simulations

We determine the global-mean ice-edge latitude as the sine of the global ice-free surface fraction.

The thermodynamic mixed-layer ocean limits the timescales to the order of decades to a century. Therefore, we here consider climate states to be stable if they stay within a climate state for at least one hundred years after initialisation without considerable drift of the ice edge.

We define the atmospheric CO_2 concentration of bifurcation points to be in the middle between the last simulated stable climate state and the next simulated climate state that transitions to a colder (warmer) climate state for decreasing (increasing) CO_2. All our results and conclusions are independent of this choice. In fact, the large number of simulations that we conduct near the bifurcation points for all model setups allows us to pinpoint the critical CO_2 values within about 100 ppmv.

4.5. Simulations to study the intensity of subtropical cloud reflectivity in a waterbelt climate state

This section is adapted from Braun et al. (2022b).
©American Meteorological Society. Used with permission. This preliminary version has been accepted for publication in the Journal of Climate and may be fully cited. The final typeset copyedited article will replace the EOR when it is published.

In this section we describe the applied atmospheric models and the corresponding simulations to study controls on subtropical cloud reflectivity. Specifically, we focus on the sensitivity of subtropical cloud reflectivity to the convection parameterization and the abundance of INPs. We analyze Cryogenian subtropical mixed-phase clouds and their environment as simulated by CAM, ICON-AES, and ICON-NWP in section 4.5.1. We further use ICON-NWP together with ICON-LEM to conduct a hierarchy of simulations ranging from coarse resolutions $\mathcal{O}(>100 \text{ km})$ to fine resolutions $\mathcal{O}(<1 \text{ km})$ as described in section 4.5.2. We describe the simulations to study the sensitivity of cloud reflectivity to the INP concentration in section 4.5.3.

4.5.1. Simulations with general circulation models at coarse horizontal resolution

We compare the GCMs CAM, ICON-AES, and ICON-NWP v2.6.1 (Collins et al., 2004; Zängl et al., 2015; Giorgetta et al., 2018; Prill et al., 2020). An overview of the simulations is given in Tab. 4.1. The CAM and ICON-AES simulations analyzed in this chapter are conducted as described in section 4.4, i.e., they are configured as aquaplanet setups with a thermodynamic mixed-layer ocean coupled to a thermodynamic sea-ice scheme. These simulations use a nominal horizontal grid spacing of $\Delta_h \approx 310$ km in CAM and $\Delta_h \approx 160$ km in ICON-AES. Specifically, we here analyze simulations with atmospheric CO_2 concentrations of 10000 ppmv in CAM and 5000 ppmv in ICON-AES. This yields approximately equal annual-mean global ice-edge latitudes due to the substantially different cloud reflectivity. The ICON-AES simulation was conducted with the default WBF tuning factor $x_{i,thr} = 5 \cdot 10^{-6}$ and the default Rayleigh-damping factor of 0.1.

In ICON-NWP we also use an aquaplanet setup. However, since our goal is to focus on atmospheric processes, we prescribe sea surfaces temperatures (SST) and sea ice cover (SIC) obtained from the ICON-AES simulation at 5000 ppmv CO_2 described in the previous paragraph. Further details are given in section 4.3.1. Applying prescribed instead of interactive SST and SIC has a negligible impact on the atmospheric circulation (not shown). Similar as in CAM and ICON-AES simulations, we apply a circular orbit with zero eccentricity and set the solar constant to 94 % of today's value (1285 Wm^{-2}). We set the concentration of atmospheric CO_2 to 5000 ppmv.

We conduct the coarse-scale global ICON-NWP simulation with $\Delta_h \approx 160$ km, 47 vertical levels reaching up to 75 km, and a timestep of 600 s. We simulate 6 years and exclude the first year from our analysis, which thus spans 5 years. As described in section 4.3.5 we apply ICON-NWP with a two-moment microphysical scheme, which is intended to be used for $\Delta_h < 3$ km (Prill et al., 2020). Nevertheless, we apply the two-moment microphysical scheme in all ICON-NWP and ICON-LEM simulations to focus on the impact of the convection parameterization on cloud reflectivity.

We apply the two-moment microphysical scheme with the default configuration for heterogeneous ice nucleation, which considers immersion and depositional freezing as parameterized by Hande et al. (2015). This parameterization determines the INP concentration as a function of air temperature and supersaturation with respect to ice. With the default settings, the maximum INP concentration at -20 °C is approximately 0.1 L^{-1}. This is a moderate value on present-day Earth, where INP concentrations at -20 °C range from 10^{-2} L^{-1} to 10^{2} L^{-1} (Kanji et al., 2017).

For the nucleation of cloud droplets we also apply the default configuration, which is based on Segal and Khain (2006) and relates the concentration of cloud condensation nuclei (CCN) to height dependent profiles of condensation nuclei (CN). Given that Cryogenian aerosol conditions are uncertain, we here apply the default settings, which correspond to a continental profile that exhibits considerably higher CN concentrations than expected in marine environments (Segal and Khain, 2006). We briefly discuss potential implications of high CCN concentrations in section 6.2.2.

Table 4.1.: Overview of simulations conducted with the GCMs CAM, ICON-AES, and ICON-NWP. Δ_h is the nominal horizontal grid spacing.

model	Δ_h [km]	period [years]	CO_2 [ppmv]	ocean	sea ice
CAM	310	40	10000	interactive thermodynamic	interactive thermodynamic
ICON-AES	160	40	5000	interactive thermodynamic	interactive thermodynamic
ICON-NWP	160	5	5000	prescribed SST	prescribed SIC with interactive surface temperatures

4.5.2. Hierarchy of ICON-NWP and ICON-LEM simulations to study the impact of convection

We here provide an overview of our hierarchy of ICON-NWP and ICON-LEM simulations across horizontal resolutions. ICON-LEM (Dipankar et al., 2015; Heinze et al., 2017; Stevens et al., 2020) also uses the ICON dynamical core, which allows us to apply the same dynamical core from coarse to fine resolutions. The hierarchy is summarized in Tab. 4.2 and further details are given in section 6.2. We label simulations by the applied model and Δ_h. NWP160 refers to the global ICON-NWP simulation with $\Delta_h = 160$ km described in section 4.5.1.

NWP160 marks the upper end of Δ_h. ICON supports grid refinement, simulations in limited-area mode (LAM), and nested subdomains (Prill et al., 2020). This allows us to conduct simulations with consecutively decreasing Δ_h based on NWP160. These simulations apply 180 vertical levels reaching up to 20 km. From the surface to 4.4 km altitude the layer thickness Δ_v gradually increases from 15 to 70 m with a logarithmic profile. Between 4.4 km and 9 km altitude, $\Delta_v = 70$ m. Above Δ_v gradually increases to 1.3 km. The simulations are configured as NWP160, except when stated otherwise.

We conduct a global ICON-NWP simulation at $\Delta_h = 10$ km (NWP10) with parameterizations for deep, mid-level and shallow convection. NWP10 spans 7 days, including 2 days of spinup, and is initialized from NWP160. Furthermore, we conduct two ICON-NWP simulations at $\Delta_h = 2.5$ km in LAM over a subtropical subdomain from 2.5° to 22.5° latitude South and spans 25° in longitudinal direction (Fig. B.4). In these two simulations, we either parameterize only shallow convection (NWP2.5) or do not parameterize convection at all (NWP2.5cex). The simulation periods are 5 and 2 days for NWP2.5

and NWP2.5cex, respectively, and include a 12 h spinup. The corresponding initial and lateral boundary conditions are derived from NWP10.

We conduct one ICON-LEM simulation at $\Delta_h = 600$ m (LEM0.6) in LAM. The corresponding subdomain spans 6° in latitudinal and longitudinal direction (Fig. B.4). We refer to this subdomain as *LEM-6°*. The simulated period is 13 h, including 7 h of spinup. The initial and lateral boundary conditions are derived from NWP2.5. LEM0.6 contains a nested subdomain with $\Delta_h = 300$ m (LEM0.3), which is centered within the LEM-6°-subdomain and spans 5° in latitudinal and longitudinal direction. We refer to this subdomain as *LEM-subdomain*. In LEM0.6 and LEM0.3 we prescribe constant SST and SIC due to the short simulation period. ICON-LEM assumes the energy-conserving scales of the turbulent spectrum to be explicitly resolved (Dipankar et al., 2015). Hence, ICON-LEM and ICON-NWP differ in the turbulence scheme (Smagorinsky (1963) vs. Raschendorfer (2001)). ICON-LEM allows us to explicitly resolve convection and use an all-or-nothing grid scale cloud-cover scheme, i.e., a grid cell is either 100 % cloudy or cloud-free. In contrast, ICON-NWP uses a fractional cloud-cover scheme.

Table 4.2.: Simulation hierarchy across nominal horizontal grid spacings Δ_h. Simulation names are defined by the applied ICON-mode (NWP and LEM) and the nominal horizontal grid spacing Δ_h given in km. The simulation NWP160 is identical to the ICON-NWP simulation listed in Tab. 4.1. All simulations listed in this table are conducted with prescribed SST and SIC and apply the two-moment microphysical scheme based on Seifert and Beheng (2006) with the default parameterization for heterogeneous ice nucleation by Hande et al. (2015). Further details concerning the simulations are given in sections 4.5.2 and 6.2.

simulation (ICON-mode and Δ_h in km)	domain	period	convection parameterization	turbulence scheme	cloud cover
NWP160	global	5 years	Tiedtke-Bechtold	Raschendorfer	fractional
NWP10	global	5 days	Tiedtke-Bechtold	Raschendorfer	fractional
NWP2.5	LAM	4.5 days	Tiedtke-Bechtold, shallow only	Raschendorfer	fractional
NWP2.5cex	LAM	1.5 days	explicit	Raschendorfer	fractional
LEM0.6	LEM-6°	6 hours	explicit	3D Smagorinsky	all-or-nothing
LEM0.3	LEM	6 hours	explicit	3D Smagorinsky	all-or-nothing

4.5.3. Simulations to study the impact of the ice nucleating particle concentration on cloud reflectivity

To investigate the sensitivity of cloud reflectivity to the INP concentration we apply a parameterization for heterogeneous ice nucleation derived by Phillips et al. (2008) instead of the default configuration. We apply this parameterization assuming that mineral dust is the only INP species available. Using this parameterization, we modify the INP concentration by increasing the number concentration of aerosol particles that potentially become activated to INPs, n_a. We conduct three simulations with $\Delta_h = 2.5$ km (NWP2.5x) and $\Delta_h = 600$ m (LEM0.6x), respectively. The NWP2.5x and LEM0.6x simulation setups are identical to NWP2.5 and LEM0.6. The only exceptions are the dust-only INP parameterization and that NWP2.5x simulations are run for only 2 days, including 12 h of spinup. The simulations are summarized in Tab. 4.3 and details are given in section 6.3.

Table 4.3.: Simulations with increased mineral dust aerosol number concentration, n_a, using the parameterization for heterogeneous ice nucleation by Phillips et al. (2008) limited to mineral dust aerosol. Except for the parameterization for heterogeneous ice nucleation and the shorter duration of NWP2.5x simulations, these simulations are configured in the same way as NWP2.5 and LEM0.6 in Tab. 4.2.

simulation	period	n_a $[L^{-1}]$
NWP2.5x1	1.5 days	7e2
NWP2.5x10	1.5 days	7e3
NWP2.5x100	1.5 days	7e4
LEM0.6x1	6 hours	7e2
LEM0.6x10	6 hours	7e3
LEM0.6x100	6 hours	7e4

5. The Robustness of the Jormungand Hypothesis in Idealized Aquaplanet Simulations and the Role of Subtropical Cloud Reflectivity

With minor adjustments in the text, large parts of this chapter are based on Braun et al. (2022a).
©The Authors.

In this chapter, we address research question 1 and the corresponding sub-questions.

1. Is the Jormungand-waterbelt scenario a robust feature of Earth's climate?
    a) Are geologically relevant Jormungand-waterbelt states a robust feature of idealized aquaplanet simulations?
    b) Under which conditions do geologically relevant Jormungand-waterbelt states exist in idealized aquaplanet simulations?
    c) How do these conditions link to the weakening of the ice-albedo feedback in the subtropical region, which constitutes the core of the Jormungand hypothesis?
    d) Can we expect these conditions to be achieved during the Cryogenian?

The structure of this chapter is as follows. We begin with testing the robustness of the Jormungand hypothesis idealized aquaplanet simulations using CAM and ICON-AES in section 5.1. We further explore the impact of subtropical cloud reflectivity in section 5.2. In order to understand and interpret the impact of subtropical cloud reflectivity we apply a one-dimensional energy-balance model in section 5.3. Finally, we summarize and discuss the main results in section 5.4. In this chapter we only use the climate version (-AES) of ICON and for brevity refer to it as ICON.

5.1. Testing the robustness of the Jormungand hypothesis

We perform simulations with CAM (Collins et al., 2004) and ICON (Giorgetta et al., 2018) as described in section 4.4, i.e., the models are configured as in Abbot et al. (2011) using an idealized aquaplanet setup with a 50 m deep mixed-layer ocean, thermodynamic sea ice, and a reduced solar constant of 1285 Wm^{-2}. We conduct simulations for a range of atmospheric CO_2 concentrations and initial sea-ice cover (Fig. A.1) to compute each GCM's bifurcation diagram.

CAM exhibits three stable climate regimes (Fig. 5.1a): a temperate regime with no or little ice cover, the waterbelt regime with an ice edge between 9° to 15° latitude, and the Snowball regime with global

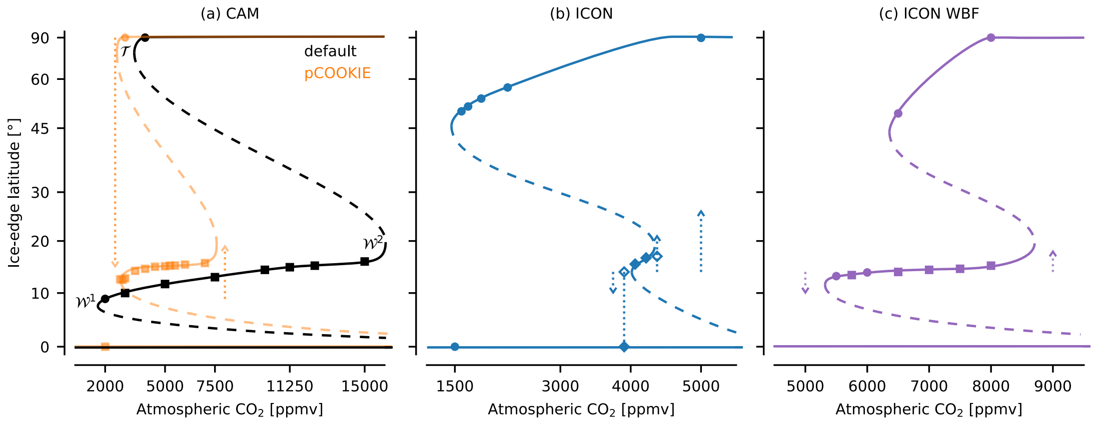

Figure 5.1.: Low-latitude clouds control the existence and absence of waterbelt states in the GCMs CAM and ICON. Bifurcation diagrams of global-mean ice edge versus atmospheric CO_2 concentrations for (a) CAM in its default configuration and with clouds made transparent to radiation in a narrow tropical region (pCOOKIE), (b) the default configuration of ICON, and (c) ICON with less efficient Wegener-Bergeron-Findeisen (WBF) process. Filled symbols show stable states. Circles show simulations initialized from ice-free conditions, squares show simulations initialized from stable waterbelt states, and diamonds represent simulations initialized from transient waterbelt states. Unfilled diamonds mark slowly drifting simulations that remain in a waterbelt-like state for at least 40 years, with arrows indicating the drift of the ice edge. Lines are drawn as best guesses of equilibrium states, with solid lines indicating stable and dashed lines indicating unstable states. $\mathcal{T}$, $\mathcal{W}^1$, and $\mathcal{W}^2$ here label the bifurcation points (nose points) corresponding to the CO_2 thresholds referred to in the text. Bifurcation points mark the unstable transitions between temperate and waterbelt/Snowball climate ($\mathcal{T}$), waterbelt and Snowball climate ($\mathcal{W}^1$), and waterbelt and temperate climate ($\mathcal{W}^2$).

ice cover. We here point out that in this chapter we use a distinction between the terms climate *state* and climate *regime*. The term climate state refers to one specific state of the climate indicated, e.g., by a specific radiative forcing and global-mean ice-edge latitude. In contrast, the term climate regime refers to a range of stable climate states, that exists over a range of radiative forcings and global-mean ice-edge latitudes.

Our simulations reproduce the findings of Abbot et al. (2011). There are three relevant bifurcation points exhibiting rapid climate transitions: 1) At 3000 ppmv CO_2 the temperate climate transitions into the waterbelt climate. We mark this CO_2 threshold by the symbol $\mathcal{T}$. 2) The transition from waterbelt to Snowball climate occurs at $\mathcal{W}^1 = 1750$ ppmv CO_2 (Abbot et al., 2011). 3) The transition from waterbelt to temperate climate occurs at $\mathcal{W}^2 = 15000$ ppmv CO_2 (Abbot et al., 2011). Thus, the waterbelt regime exists over $\mathcal{W}^2 - \mathcal{W}^1 \approx 13000$ ppmv CO_2 and is easily accessible from the temperate climate because $\mathcal{W}^1 < \mathcal{T}$.

ICON yields a strikingly different bifurcation diagram (Fig. 5.1b), which questions the robustness of the Jormungand-waterbelt scenario. In ICON, waterbelt states exist only over a narrow range of CO_2 since $\mathcal{W}^2 - \mathcal{W}^1 \approx 400$ ppmv. Even more importantly, in ICON waterbelt states are not accessible from the temperate state because $\mathcal{T} = 1594$ ppmv CO_2 is smaller than $\mathcal{W}^1 \approx 4000$ ppmv CO_2. Thus, although waterbelt states exist, they are geologically irrelevant.

Although using the same idealized aquaplanet setup, CAM and ICON simulations exhibit differences in (1) the initial and (2) boundary conditions, as well as (3) differences in the applied sea-ice scheme. Regarding all three aspects there is no qualitative impact on our key results, as lined out in the following.

(1) The initial conditions differ in terms of sea surface temperature (SST) patterns between CAM and ICON. In CAM homogeneous SSTs of 300 K are used while in ICON a zonally symmetric SST-profile reaching from 273.5 K at the poles to 302.5 K at the equator is applied. We conducted ICON simulations (at 1500 ppmv CO_2 and 3000ppmv CO_2) with initially homogeneous SSTs of 300 K and found no difference in the equilibrium state that ICON drifts to.

(2) Boundary conditions between ICON and CAM differ in the amount of well-mixed greenhouse gases and the ozone climatology. ICON uses no well-mixed greenhouse gases except CO_2. CAM uses the well-mixed greenhouse gases CH_4, N_2O, CFC_{11}, and CFC_{12} with the volume mixing ratios defined in Pierrehumbert et al. (2011). Additional greenhouse gases exert an additional radiative forcing and therefore to shift the bifurcation diagram to lower CO_2 concentrations. Besides the shift of the bifurcation diagram the additional forcing is not expected to alter the structure of the bifurcation diagram and the stability of the waterbelt state. The ozone concentration applied in ICON was derived from the ozone climatology applied in CAM by calculating the annual-mean and symmetrizing across the equator (Liang et al., 1997). Therefore the ozone concentrations in CAM and ICON exhibit similar magnitudes and are not expected to lead to qualitative differences in the bifurcation diagrams.

(3) The fundamental difference between the sea-ice schemes applied in CAM and ICON is the vertical resolution of sea ice. ICON applies a 0-layer scheme (Semtner, 1976), whereas CAM applies a 4-layer scheme (Bitz and Lipscomb, 1999). The multi-layer sea-ice scheme applied in CAM keeps track of ice internal energy and therefore buffers summer and daytime melting (Abbot et al., 2010), which facilitates Snowball initiation (Yang et al., 2012). Hörner et al. (2022)[1] conducted ICON simulations with the 0-layer Semtner sea-ice scheme as described in section 4.3.1 and a 3-layer sea-ice scheme by Winton (2000) and studied the implications for Snowball Earth initiation. With the 3-layer sea-ice scheme ICON more readily initiated a Snowball climate compared to using the 0-layer sea-ice scheme. Therefore, we apply the 0-layer scheme in ICON because it facilitates the simulation of stable waterbelt states.

5.2. The impact of subtropical cloud reflectivity

CAM and ICON both exhibit bare sea ice in the subtropical region and thus low reflection at the surface and in clear-sky conditions at the top-of-atmosphere, consistent with the Jormungand hypothesis (Fig. A.3). Yet, planetary albedo α is much lower in ICON (Fig. 5.2a), because ICON simulates fewer clouds than CAM, and as a consequence a weaker shortwave cloud-radiative effect (SWCRE) over ice-free

---

[1] The article Hörner et al. (2022) resulted from the Master thesis of Johannes Hörner, which I co-supervised during my PhD.

ocean (Fig. 5.2b and c). The most pronounced difference arises from low-level clouds in the subtropics and tropics (Figs. 5.2d and e).

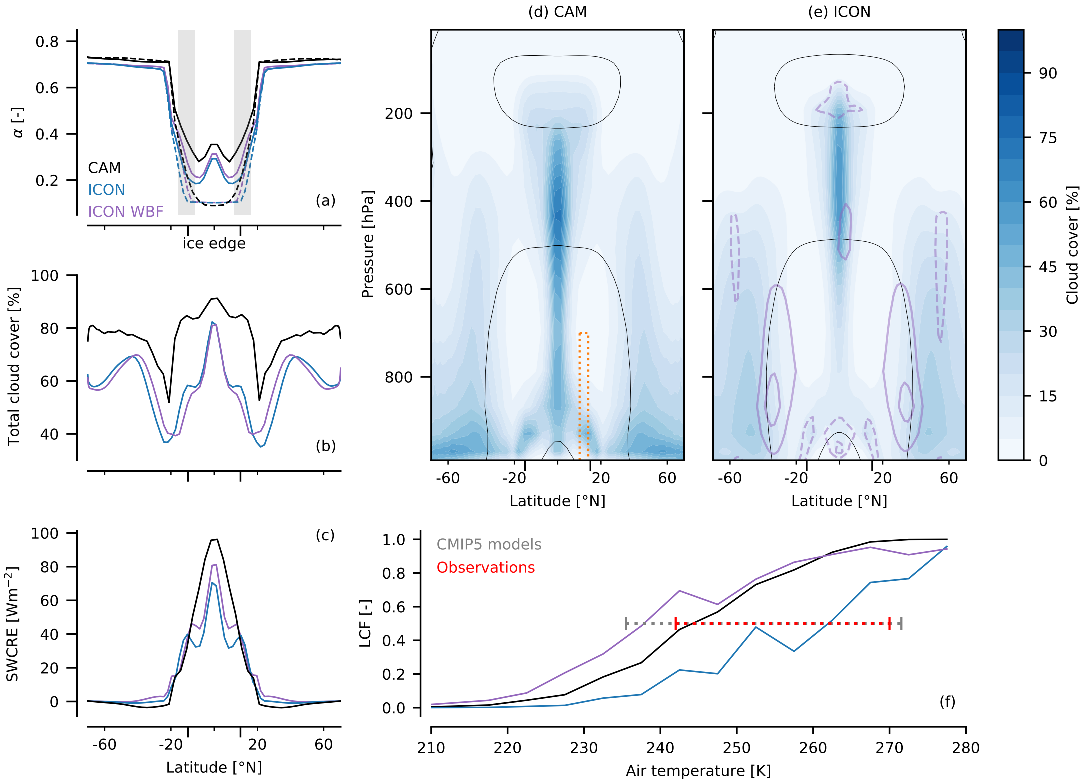

Figure 5.2.: Differences in clouds and their shortwave cloud-radiative effect (SWCRE) as obtained from the GCMs CAM and ICON as well as ICON with modified Wegener-Bergeron-Findeisen process (ICON WBF). (a) Zonal-mean annual-mean planetary albedo α for all-sky (solid) and clear-sky conditions (dashed), (b) total cloud cover, and (c) SWCRE averaged over all stable waterbelt states for each model. The grey band in (a) indicates the range of global-mean ice-edge latitudes for all stable equilibrium states found in CAM, ICON, and ICON WBF simulations. (d,e) Zonal-mean cloud cover together with 273 K, 235 K, and 192 K isotherms in CAM and ICON for simulations with comparable global-mean ice cover (10000 ppmv CO_2 in CAM; 4063 ppmv CO_2 in ICON). Orange dotted box in (d) shows region of CAM pCOOKIE modification for Northern hemisphere. Purple contours in (e) show cloud-cover difference between ICON WBF (at 6000 ppmv CO_2) and ICON (contour interval of 3%; positive differences in solid). (f) Liquid condensate fraction (LCF) from simulations shown in (d) and (e). The range of temperatures for which liquid and ice are equally prevalent for 26 Coupled Model Intercomparison Project phase 5 (CMIP5) GCMs is shown in grey. The red line shows the combined observational range of ground based LIDAR and air craft measurements (McCoy et al., 2016).

The differences in cloud cover do not arise from differences in the large-scale atmospheric state. The vertical and zonal structure of air temperature as characterized by the 273, 235 and 192 K isotherms is similar in both GCMs (Figs. 5.2d and e), as is the Hadley circulation (Figs. A.4 and A.5). As the 273 and 235 K isotherms mark the limits of pure liquid and pure ice clouds (Boucher et al., 2013), the low-level clouds in the subtropics and tropics are mixed-phase clouds.

The treatment of mixed-phase clouds is highly uncertain in GCMs (McCoy et al., 2016) and is based on various microphysical modeling approaches. The main difference between CAM and ICON arises from liquid-ice-partitioning (LIP): CAM applies explicit LIP based on air temperature, while in ICON

LIP results from a comprehensive set of conversion rates between liquid and ice phase (see section 4.3.5). Furthermore, the temperature range over which the liquid and ice phases can co-exist differs considerably, with -40 °C to -10 °C in CAM and -35 °C to 0 °C in ICON.

The different treatment of cloud micropyhsics has a clear impact on the simulated liquid condensate fraction (LCF). We calculate LCF for 40-year periods of single simulations for CAM (10000 ppmv CO_2), ICON (4063 ppmv CO_2), and ICON WBF (6000 ppmv CO_2). We use monthly-mean zonal-mean data on the pressure levels used in CAM simulations. We apply vertical weighting by the pressure level thickness and horizontal weighting by the cosine of latitude. We further bin LCF by air temperature. For binning we use 5K-intervals of air temperature and exclude data points with total cloud condensate below $1e^{-7}$ $kg\ kg^{-1}$.

Sampling clouds by air temperature and LCF shows that ICON generates relatively more cloud ice at higher temperatures than CAM (Fig. 5.2f) and indicates that the liquid-to-ice conversion is more efficient in ICON. A lower LCF leads to optically thinner clouds because cloud ice crystals are typically larger than cloud liquid droplets, and also works in favor of less cloud cover since ice crystals settle more efficiently than smaller cloud droplets (Vergara-Temprado et al., 2018). Hence, the more icy mixed-phase clouds in ICON explain the considerably lower planetary albedo over ice-free ocean compared to CAM.

The temperature at which LCF crosses a value of 0.5 in our simulations is well within the large temperature range simulated by Coupled Model Intercomparison Project phase 5 (CMIP5) GCMs and the combined observational range of ground based LIDAR and air craft measurements (McCoy et al., 2016) (Fig. 5.2f). Furthermore, there is considerable uncertainty arising from Cryogenian atmospheric boundary conditions, including aerosol amount and composition (Abbot and Halevy, 2010; Feulner et al., 2015), which may strongly impact mixed-phase clouds physics (Vergara-Temprado et al., 2018), as well as the applied convection schemes that were developed for present-day climate. Although the treatment of mixed-phase clouds is more comprehensive in ICON, these uncertainties mean that we cannot judge whether the clouds in CAM or ICON are more realistic.

We demonstrate the sensitivity of waterbelt states to clouds by running additional simulations, in which we manipulate cloud radiation in CAM and microphysical processes in ICON (Fig. A.2).

First, we locally disable cloud-radiative effects (CRE) in CAM pCOOKIE simulations as described in section 4.1.2. These simulations are inspired by the Clouds On-Off Klimate Intercomparison Experiment (COOKIE) (Stevens et al., 2012). We disable CRE in the region that captures the strong differences in low-latitude low-level clouds between CAM and ICON in each hemisphere (orange box in Fig. 5.2d). Yet, the impact on the global energy balance is small. Therefore, $\mathcal{T}$ is only marginally affected (Fig. 5.1a). The modification mainly affects SWCRE, since it is applied to low-level clouds (Fig. A.6).

When low-level tropical clouds are made transparent in CAM, the CO_2 range over which the waterbelt climate exists, shrinks from 13000 to approximately 5000 ppmv (Fig. 5.1a). Moreover, the CO_2 required to initiate a Snowball from a waterbelt climate increases to $\mathcal{W}^1 = 2375$ ppmv. As a result, the waterbelt state is almost unaccessible, and CAM with modified clouds approaches the behavior of ICON in terms of the geological relevance of the waterbelt climate regime. We find a qualitatively similar behaviour if we disable CRE in other regions (not shown).

Second, we reduce the efficiency of liquid-to-ice conversion in ICON, to increase the LCF to a value close to CAM. Liquid-to-ice conversion in mixed-phase clouds strongly depends on the Wegener-Bergeron-Findeisen process (WBF) (Storelvmo and Tan, 2015). The WBF occurs as the saturation pressure over water is greater than the saturation pressure over ice and, which allows ice crystals to grow at the expense of cloud droplets in mixed-phase clouds. We weaken the WBF in ICON by modifying a loosely constrained tuning parameter within plausible ranges as suggested in Mauritsen and Roeckner (2020) and described in section 4.4.

Weakening the WBF drastically increases cloud liquid, i.e., LCF, SWCRE and planetary albedo (Figs. 5.2 and A.7) and results in a strong cooling effect. As a consequence, higher atmospheric CO_2 concentrations are required to maintain a temperate climate and $\mathcal{T}$ increases to 6250 ppmv (Fig. 5.1c). More importantly, however, reduced liquid-to-ice conversion via the WBF allows ICON to exhibit waterbelt climates that are accessible and exist over a substantial range of CO_2, namely from $\mathcal{W}^1 = 5250\,\text{ppmv}$ to $\mathcal{W}^2 = 8500\,\text{ppmv}$ (Fig. 5.1c).

In summary, our GCM simulations clearly show that tropical clouds and their impact on planetary albedo can determine the geological relevance of the waterbelt climate regime.

5.3. Understanding the impact of cloud reflectivity in a one-dimensional energy balance model

To understand how low-latitude clouds shape the waterbelt states via their impact on planetary albedo, we apply the one-dimensional energy balance model (EBM) following Abbot et al. (2011) as introduced in sections 2.2 and 2.4. The EBM considers two opposing climate feedbacks: The negative longwave feedback, which is considered to be constant, and the positive ice-albedo feedback. The ice-albedo feedback depends on the ice-edge latitude, because ice albedo is high for snow covered ice in the extratropics $\alpha_{i,s} = 0.8$ and low for bare ice at low latitudes $\alpha_{i,b} = 0.45$ Abbot et al. (2011). Planetary albedo over ice-free ocean α_o is homogeneous and is dominated by shortwave reflection by clouds (Fig. 5.2a). Hence, the ice-albedo feedback in the waterbelt regime is determined by the ratio $\alpha_o/\alpha_{i,b}$.

The EBM captures the qualitative differences among GCM simulations (Fig. 5.3a). We estimate the EBM parameters from GCM simulations for the longwave feedback, α_o and meridional heat transport as described in section A.6. If the EBM is driven with ICON parameters, the waterbelt regime is not accessible and has substantially weaker CO_2-hysteresis compared to CAM parameters. If driven by CAM pCOOKIE instead of CAM parameters, the hysteresis of the waterbelt regime shrinks, and the waterbelt state becomes inaccessible from the temperate climate. We do not analyze the EBM with ICON WBF parameters because it fails to satisfy the requirement of a constant longwave feedback as shown in Tab. A.1 and lined out in section A.6.

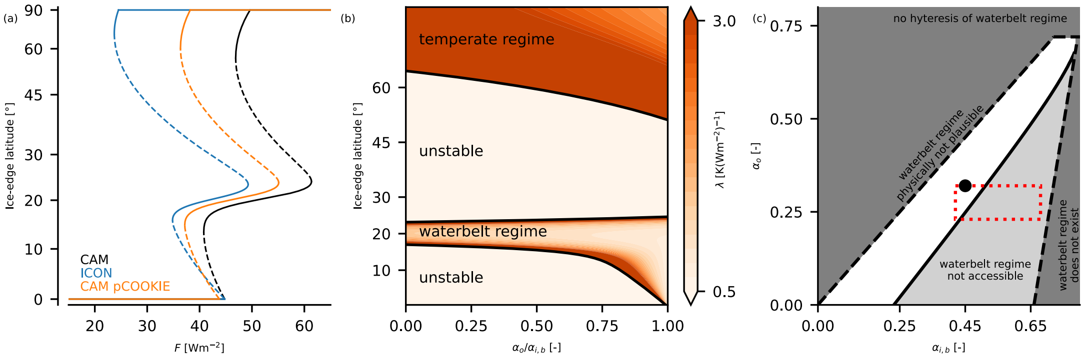

Figure 5.3.: Analysis of the waterbelt regime in a one-dimensional energy balance model (EBM). (a) Bifurcation diagrams of ice-edge latitude vs. CO_2-radiative forcing F calculated from the EBM with parameters estimated from the GCMs. (b) Climate sensitivity parameter λ determined from the EBM as a function of the ratio of planetary albedo over ice free ocean α_o and bare sea-ice albedo $\alpha_{i,b}$ and ice-edge latitude. (c) Map in α_o-$\alpha_{i,b}$-space showing domains of stable and accessible waterbelt states (white) and stable but unaccessible waterbelt states (light gray). The black dashed lines indicate the margins within which the waterbelt regime can exist. The red dotted box indicates the range of plausible values for α_o and $\alpha_{i,b}$. The black circle marks albedo values for CAM.

Using the EBM, we calculate the climate sensitivity parameter λ for equilibrium climate states as described in section A.7. We limit our analysis to $\alpha_o < \alpha_{i,b}$ and use $\alpha_{i,b} = 0.45$. The EBM exhibits stable states with positive finite λ for the temperate, waterbelt, and hard Snowball regime (not shown) and unstable climate regimes with negative λ in between (Fig. 5.3b).

Larger α_o allows waterbelt states to extend to lower latitudes, because the ice-albedo feedback becomes weaker as α_o is increased. At higher α_o, changes in ice cover have a smaller radiative impact at top of the atmosphere. A similar behavior is observed for the cloud impact on the radiation budget over the present-day Arctic (Sledd and L'Ecuyer, 2019). As a result, high cloud contribution to planetary albedo supports stable waterbelt states by muting the shortwave impact of changes in ice cover.

The combination of GCM simulations with the EBM analysis distills an important mechanism by which low-latitude clouds control the width and accessibility of the waterbelt regime. If clouds are abundant and cause a high albedo over ice-free ocean, the waterbelt regime is wide and easily accessible. In contrast, if clouds are scarce, the waterbelt regime is narrow and potentially inaccessible. This shows that the stark differences between CAM and ICON are to a large extent related to their strong differences in low-latitude clouds, of which there are many in CAM and few in ICON.

We further use the EBM to assess whether a waterbelt scenario is a likely explanation for Cryogenian geology. The waterbelt regime can exist over a wide range of $\alpha_{i,b}$ and α_o (enclosed by black dashed lines in Fig. 5.3c)). Yet, its accessibility requires α_o to exceed a threshold, which increases with increasing $\alpha_{i,b}$ (white domain in Fig. 5.3c). If α_o is too small, the subtropical ice-albedo feedback is too strong to escape the runaway feedback towards a hard Snowball state. We calculate the accessibility of the waterbelt climate regime in the EBM as proposed in Abbot et al. (2011).

The albedo values for CAM are located within the domain of accessible waterbelt climate states (black circle in Fig. 5.3c). Yet, a subtle decrease of α_o makes the waterbelt regime unaccessible as shown in Fig. A.8, comparably to our CAM pCOOKIE simulations with modified clouds. Furthermore, the EBM analysis indicates that a small increase of $\alpha_{i,b}$ would also make the waterbelt regime in CAM unaccessible.

We define a domain of physically plausible albedo values based on the range of α_o found in our GCM simulations and estimates for $\alpha_{i,b}$, that range from 0.42 to 0.68 (Dadic et al., 2013) (red dotted rectangle in Fig. 5.3c). The EBM predicts stable waterbelt states for the entire plausible domain. However, the overlap of the plausible domain and accessible waterbelt states is small and confined to low plausible $\alpha_{i,b}$. In fact, the geologically relevant waterbelt regime simulated by CAM results from the combination of rather extreme values for α_o and $\alpha_{i,b}$. Hence, a geologically relevant waterbelt regime is physically possible, but its viability is limited to a narrow range of key parameters.

5.4. Discussion and conclusions

Waterbelt states were proposed as alternative solutions for the pan-glaciations of the Cryogenian that, in contrast to a hard Snowball Earth, can easily explain the survival of life by providing a narrow strip of ice-free tropical ocean (Abbot et al., 2011). Waterbelt states were suggested based on fundamental physics of the tropical atmospheric circulation, the hydrological cycle and the albedo of dark bare versus bright snow-covered sea ice. These physics are well understood and robustly represented in models, lending support to the viability of waterbelt scenarios.

However, our results provide evidence that waterbelt solutions are not a robust feature of climate and that their geological relevance depends on uncertain cloud processes. We use two global climate models with different treatments of clouds and an energy balance model to demonstrate the impact of low-latitude clouds. First, clouds influence the range of CO_2 for which waterbelt states exists. Second, clouds control whether waterbelt states are accessible from a temperate climate.

The importance of clouds arises because clouds control the strength of the ice-albedo feedback. If clouds contribute little to the reflection of shortwave radiation at the top of atmosphere, e.g., because they are scarce or optically thin, then the low-latitude ice-albedo feedback is stronger. In our simulations, modifying clouds within physically plausible bounds shrinks the CO_2 range of waterbelt states by a factor of two or more and renders waterbelt states inaccessible.

Our study highlights the role of clouds and their interactions with sea ice by applying an aquaplanet setup. Incorporating land masses, ocean heat transport, and sea-ice dynamics also affects the waterbelt climate as shown in Voigt and Abbot (2012), Rose (2015), and Pollard et al. (2017), who explicitly referred to the Jormungand hypothesis (see section 2.4 for a review of these studies). The masking effect of highly reflective clouds that we identify here can be considered to impact the waterbelt climate also in the less idealized setups applied in these studies. We discuss potential implications of our results in this context in the following.

Voigt and Abbot (2012) were able to simulate stable low-latitude waterbelt states in ECHAM5/MPI-OM stabilized by the Jormungand mechanism only if disabling sea-ice dynamics. As Voigt and Abbot (2012) mentioned, this suggests that the impact of sea-ice dynamics, which destabilizes the low-latitude ice edge by wind-driven equatorward drag and viscous flow of sea ice, is stronger than the stabilizing effects. Conversely, in Yang et al. (2012) stable low-latitude waterbelt states existed with sea-ice dynamics being active in CCSM3. Voigt and Abbot (2012) attributed this difference to stronger sea-ice dynamics in ECHAM5/MPI-OM compared to CCSM3. In light of our results at least part of the difference between ECHAM5/MPI-OM and CCSM3 may arise from clouds. The corresponding atmosphere components ECHAM5 and CAM are applied in Abbot et al. (2011) and lead to quantitatively different bifurcation diagrams with a smaller CO_2-hysteresis in ECHAM5, which indeed is consistent with weaker subtropical cloud reflectivity in ECHAM5 compared to CAM. Hence, in general the forcing exerted onto the ice-edge position by the Jormungand mechanism and sea-ice dynamics may be on the same order of magnitude.

Voigt and Abbot (2012) further found that the presence of ocean heat transport allowed the waterbelt state to exist at a lower CO_2-radiative forcing but not at a lower ice-edge latitude. This has two major implications. First, as hypothesized by Rose (2015), ocean heat transport and the Jormungand mechanism seem to act jointly. Hence, the continuous range of climate states found in Voigt and Abbot (2012) extending from about 25° latitude (~ 55 % sea-ice cover) to about 10° latitude may be stabilized by ocean heat transport at the upper end and the Jormungand mechanism at the lower end. However, Voigt and Abbot (2012) obtained the same latitudinal range of climate states without ocean heat transport, which indicates a potentially important impact of continents on the Jormungand hypothesis. Second, the maximum expansion of sea ice towards the equator before climate transitions to a Snowball state is limited rather by the Jormungand mechanism than by ocean heat transport. Hence, in the subtropical region the Jormungand mechanism appears to be more important for maintaining a stable waterbelt climate than ocean heat transport.

Rose (2015) and Pollard et al. (2017) applied albedo values that are similar to the values applied in Abbot et al. (2011) and therefore are suitable to simulate Jormungand-waterbelt states. However, as discussed in section 2.4, Rose (2015) and Pollard et al. (2017) did not find Jormungand-waterbelt states. Based on Voigt and Abbot (2012) and our results, we suggest that in Rose (2015) and Pollard et al. (2017) subtropical cloud reflectivity may have been too low to find Jormungand-waterbelt states. Rose (2015) and Pollard et al. (2017) did not analyze clouds explicitly but attributed the absence of the Jormungand mechanism in their GCM simulations to ubiquitous snow cover.

However, in Rose (2015) no climate state was analyzed, for which the ice-edge latitude was below 20°. We suggest that the analyzed climate state in Rose (2015) is not suited to draw conclusions regarding subtropical snow cover because for latitudes poleward of 20° sea ice was also entirely snow covered in Abbot et al. (2011). Instead, we propose to seek the cause for the absence of the Jormungand mechanism in clouds. Rose (2015) applied MITgcm with the atmosphere model SPEEDY, which solves the primitive equations on five vertical levels, of which one level is considered to represent the boundary layer (Molteni, 2003). SPEEDY does not consider cloud formation within the boundary layer and cloud albedo is only related to total cloud cover (Molteni, 2003). Thus, SPEEDY is not suited to simulate the low-level mixed-phase clouds that stabilize the waterbelt climate in our simulations.

We similarly suggest that the analyzed climate states in Pollard et al. (2017) are not suited to draw conclusions regarding subtropical snow cover. In Pollard et al. (2017) snow cover was analyzed in a waterbelt state with an ice edge at 32° latitude and a Snowball state. For the former, the same argument as above applies. For the latter, we argue that consistent with, e.g., Hoffman et al. (2017) the annual-mean hydrological cycle is reversed in the Snowball state due to the low surface heat capacity. Hence, in a Snowball state no sublimation of subtropical snow can be expected. Therefore, we also suggest to seek explain the absence of the Jormungand mechanism in Pollard et al. (2017) by clouds. Pollard et al. (2017) explicitly mentioned that the applied GCM GENESIS exhibits fewer clouds but more cloud condensate, presumably ice, at high altitudes than other GCMs applied in Snowball climate. Hence, GENESIS likely lacks sufficiently high amounts of supercooled liquid in subtropical mixed-phase clouds, which is required for highly reflective clouds that stabilize the waterbelt climate at low latitudes.

Overall, the stabilizing role of low-latitude mixed-phase clouds provides potential explanations for the discrepancies of previous GCM-based studies (Voigt and Abbot, 2012; Yang et al., 2012; Rose, 2015; Pollard et al., 2017). This highlights the important role of clouds as an important factor for Cryogenian waterbelt scenarios also in less idealized model setups. Furthermore, setups incorporating aerosol released from land surfaces and marine life provide the option of influencing waterbelt states via cloud microphysical processes (Feulner et al., 2015; Abbot et al., 2010).

The stabilizing mechanism of shortwave cloud reflection proposed in this work also has potential implications for the climate on extrasolar planets and their habitability. A planet is classically considered to be habitable if liquid water is available at the planet's surface. Wolf et al. (2017) suggested that waterbelt climate states may be considered to widen the range of habitable climates within the habitable zone. This suggestion appears intuitive and, indeed, waterbelt states extend the range of ice-edge latitudes, over which habitable climate states occur, towards the equator. This also extends the range of global-mean surface temperatures and radiative forcings, for which habitable climates occur, to lower values than without a waterbelt state and everything else being equal, i.e., the temperate and the Snowball state with the corresponding bifurcation points remaining unchanged. However, if the reason for the absence of the waterbelt state is rooted in too low cloud reflectivity for the presence of the waterbelt state, this implies that the temperate state can exist at a lower radiative forcing. This is the case because lower cloud reflectivity leads to a higher fraction of the solar radiation being absorbed by the Earth system. Hence, the temperate climate can be maintained at a lower radiative forcing. This is evident from comparing the lowermost CO_2 concentrations, at which any non-Snowball climate state exists, in our GCM simulations with ICON and ICON WBF shown in Fig. 5.1b and c. In ICON habitable climates exist down to 1594 ppmv CO_2, while in ICON WBF habitable climates do not exist below 5250 ppmv CO_2 at the same solar forcing.

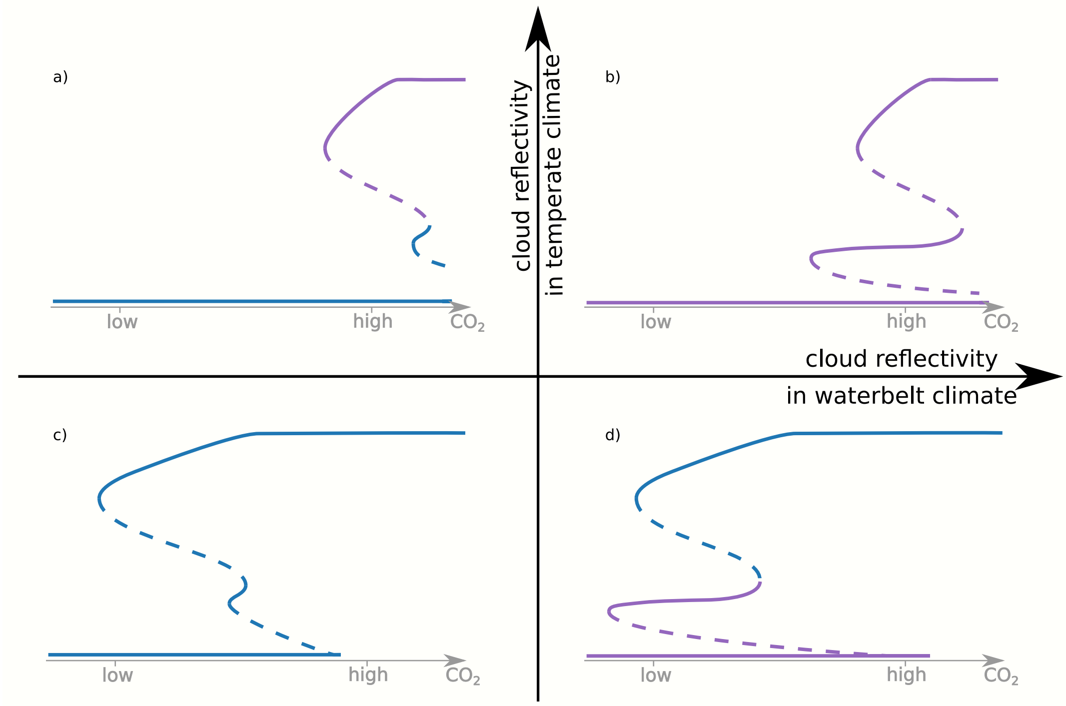

Figure 5.4.: Impact of cloud reflectivity in the temperate and waterbelt climate on (hypothetical) bifurcation diagrams. The grey axes indicate the level atmospheric CO_2 and the corresponding CO_2radiative forcing. Bifurcation diagrams are sorted by cloud reflectivity in the temperate climate and the waterbelt climate, which is indicated by the black axes. b) and c) represent the best guesses of the bifurcation diagrams as derived from the ICON WBF and ICON GCM simulations in Fig. 5.1. a) and d) represent hypothetical bifurcation diagrams assuming a strong cloud response to the transition from the temperate to the waterbelt climate. Specifically, a) assumes cloud dissipation and d) assumes cloud invigoration. In consequence, a) exhibits the lowest and d) the highest resilience against global glaciation (see text for further explanation). For a general explanation of birurcation diagrams see Figs. 2.1 and 2.2 and the corresponding explanations in sections 2.2 and 2.4.

Fig. 5.4b and c also shows the best guesses of the bifurcation diagrams derived from ICON WBF and ICON and sorts the bifurcation diagrams by cloud reflectivity in the temperate and waterbelt climate, which increase along the black axes. ICON WBF exhibits high cloud reflectivity in both climate states. Conversely, ICON exhibits low cloud reflectivity in both climate states. Hence, while overall weak cloud reflectivity allows a planet to maintain a temperate climate, i.e., to be habitable, at a low radiative forcing (Fig. 5.4c), overall strong cloud reflectivity allows a planet to prevent the Snowball catastrophe and instead settle in a waterbelt state once the radiative forcing is too weak to maintain the temperate climate (Fig. 5.4b). If the planet exhibits a warming mechanism in the waterbelt climate, e.g., accumulation of atmospheric CO_2 similar to the Cryogenian Earth under intense ice cover, the climate can return to the temperate state again without experiencing a Snowball climate (cf. Fig. 2.2). A planet's ability to maintain a temperate climate and to prevent the Snowball catastrophe determine the planet's resilience against global glaciation. The clouds simulated in ICON and ICON WBF either promote the ability to maintain a temperate climate or the ability to prevent the Snowball. Qualitatively, this leads to moderate resilience against global glaciation in either case.

The resilience of a planet against global glaciation can be impacted by the cloud response to the change of the climatic state. The cloud response likely affects cloud abundance and composition and thus cloud reflectivity if a planet's climate transitions from a warm to a cold climate. Depending on the nature of the cloud response, clouds may either increase or decrease the resilience against global glaciation. For example, clouds may dissipate (Hyde et al., 2000) or be more abundant in a colder climate (Chandler and Sohl, 2000). The lowest resilience against global glaciation occurs for strong cloud reflection in the temperate climate in combination with cloud dissipation when transitioning to a colder climate (Fig. 5.4a). In this case the planet can neither maintain liquid surface water at a low radiative forcing nor do clouds prevent the Snowball catastrophe once the radiative forcing is too low to maintain the temperate climate. Conversely, the highest resilience against global glaciation occurs for weak cloud reflection in the temperate climate in combination with cloud invigoration at low latitudes when transitioning to a colder climate (Fig. 5.4d). In this case the planet can maintain liquid surface water at a low radiative forcing and clouds prevent the Snowball catastrophe once the radiative forcing is too low to maintain the temperate climate. Such a cloud response may be triggered by an invigorated Hadley circulation in a colder climate, which would impact atmospheric stability, or the changing abundance of aerosols that may serve as cloud condensation nuclei or ice nucleating particles.

We note that our analysis only accounts for variations of the CO_2-radiative forcing. Yang et al. (2012) compared the impact of the radiative forcing exerted by atmospheric CO_2 and the sun. The forcings mainly differ because the reduction of CO_2 is uniform while the reduction of solar radiation is strongest at the equator and decreases towards the poles. Therefore, for similar changes in the total radiative forcing, reducing CO_2 results in more rapid glaciation in climate states, with high-latitude ice edges, while reducing solar radiation results in more rapid glaciation in climate states with low-latitude ice edges. If starting GCM simulations from the same climate state with a high-latitude ice edge and applying a similar reduction of the total radiative forcing, Yang et al. (2012) found that reducing solar radiation leads to a Snowball more readily than reducing CO_2. Nevertheless, reducing the solar and CO_2-radiative forcing triggers similar feedbacks (Hansen et al., 1984). Therefore, we consider the general mechanism revealed by our results to also account for variations of the solar forcing.

Furthermore, our results may also have implications for climate on planets near the outer limit of the habitable zone (OHZ). The habitable zone covers the range of distances between a planet and its star, for which the planet exhibits liquid surface water (see e.g. Schwieterman et al. (2019)). The OHZ is conventionally defined as the distance of a planet from its star, at which any increase in atmospheric CO_2 does not allow the planet to maintain liquid surface water (see e.g. Schwieterman et al. (2019)). The masking effect of clouds that we discussed in the previous paragraphs for planet's located *within* the habitable zone likely affects the even more extreme climate near the OHZ in a similar manner. von Paris et al. (2013) suggested that at the OHZ scattering of incident stellar radiation by CO_2 clouds and the generally dense CO_2 atmosphere decreases the ice-albedo feedback on planets orbiting sun-like stars. The masking effect of clouds found in our work arises from the condensation of H_2O instead of CO_2. Nevertheless, our results also show a weakening of the ice-albedo feedback with increasing cloud condensate and demonstrate that the effect identified by von Paris et al. (2013) based on plane-parallel radiative transfer calculations also occurs in the three-dimensional atmospheric models applied here. The convergence of modeling dense CO_2 atmospheres and the three-dimensional atmospheric circulation is currently under development (Way et al., 2017) as further discussed in section 7.2.

Finally, our key finding is that waterbelt states are only geologically relevant if planetary albedo over ice-free ocean, i.e., shortwave reflection by clouds, is at the upper end of its plausible range, and if simultaneously bare sea ice albedo is at the lower end of its plausible range. This has two major implications. First, the requirement of extreme albedo values and the sensitivity of waterbelt states to uncertain cloud processes strongly questions the idea that the Cryogenian pan-glaciations and their geology can be explained without a hard Snowball Earth. Thus, Cryogenian life has likely faced harsh evolutionary conditions under long lasting global ice cover, which it most likely may have survived thanks to surface dust exposure and dust cycling by sea glaciers (Hoffman, 2016; Hoffman et al., 2017). Second, we would be able to reject the Jormungand hypothesis in idealized aquaplanet setups if we were able to constrain subtropical cloud reflectivity to low values. However, the here identified strong sensitivity of the waterbelt climate arises from mixed-phase clouds, which are uncertain across global climate models (McCoy et al., 2016) and thus contribute substantially to uncertainty in model-based estimates of climate sensitivity of the present-day climate (Zelinka et al., 2020). Our results demonstrate that clouds are not only crucial to anticipate future climate change, but also to understand the dynamics of the Cryogenian glaciations. However, the well-known uncertainty associated with representing clouds under presented-day climate conditions (Boucher et al., 2013; Sherwood et al., 2014; McCoy et al., 2016; Zelinka et al., 2020) prohibits to constrain subtropical shortwave cloud reflection.

A promising approach to reduce cloud uncertainty in atmospheric models that are used to assess present-day climate is the application of high-resolution models that allow to reduce uncertain assumptions associated with the representation of clouds. In chapter 6 we follow this approach in order to assess whether explicitly resolving hectometer-scales of atmospheric motion may help us to constrain Cryogenian cloud reflectivity.

6. Cryogenian Subtropical Cloud Reflectivity Across a Hierarchy of Atmospheric Models

With some minor adjustments in the text, this chapter is based on Braun et al. (2022b).

In chapter 5 we showed that the existence of stable Jormungand-waterbelt states requires the presence of highly reflective low-level mixed-phase clouds at and near the subtropical ice edge. The reflectivity of mixed-phase clouds is strongly determined by the amount of supercooled liquid that they contain (see e.g. Vergara-Temprado et al. (2018)). The dynamical and microphysical processes that determine the abundance of supercooled cloud liquid cannot be explicitly represented in GCMs and rely on parameterizations. This gives rise to substantial uncertainty of the cloud-radiative forcing in future climate projections even under modern climate conditions (Boucher et al., 2013; Sherwood et al., 2014; McCoy et al., 2015). Poorly constrained parameters contained in parameterizations are usually applied as tuning parameters, i.e., adjusted in order to reduce biases between the simulated climate and observations of present-day climate (Hourdin et al., 2017). Due to the lack of observations of paleoclimate atmospheric conditions, parameterizations that were tuned for present-day Earth are often used for paleoclimate simulations even though this may not be valid (Pierrehumbert et al., 2011; Abbot et al., 2012; Kageyama et al., 2017). As shown in chapter 5 the existence of a stable waterbelt climate can be triggered by varying a loosely constrained tuning parameter, which represents the efficiency of the Wegener-Bergeron-Findeisen (WBF) process. The WBF process is an important sink for supercooled liquid in shallow low-level mixed-phase clouds (Korolev et al., 2017). As described in section 4.3.5 the efficiency of the WBF process dependends on the number of ice crystals and in turn on the abundance of ice nucleating particles (INPs) and the intensity of updrafts. Both processes need to be parameterized in global coarse-scale GCMs. Consequently, in GCMs, the requirement to parameterize sub-grid updrafts that strongly impact cloud microphysical processes prohibits a judgement whether Cryogenian subtropical cloud reflectivity may have been sufficiently high to allow the existence of a stable waterbelt state. Therefore, we investigate here whether resolving hectometer to kilometer scales of atmospheric motion provides more robust insights into Cryogenian subtropical cloud reflectivity.

Resolving small scales of atmospheric motion allows us to reduce, and at scales of hectometers even omit, uncertain convection parameterizations. We make use of this by applying a state of the art two-moment microphysical scheme that directly couples aerosol-cloud interactions to the resolved atmosphere dynamics (Seifert and Beheng, 2006; Seifert et al., 2011; Phillips et al., 2008; Hande et al., 2015). The two-moment microphysical scheme further allows us to explicitly consider the abundance of INPs. We here present a hierarchy of global and local simulations that span horizontal grid spacings from 160 km to 300 m with the ICOsahedral Nonhydrostatic atmosphere model in numerical weather prediction mode (ICON-NWP) and large-eddy mode (ICON-LEM) as described in section 4.5.2. Additionally, we conduct simulations with different INP concentrations as described in section 4.5.3. This allows us to address research question 2 and the corresponding sub-questions.

2. Can we rule out the Jormungand hypothesis in idealized aquaplanet simulations due to the critical role of subtropical cloud reflectivity?
    a) How does Cryogenian subtropical cloud reflectivity compare among three GCMs with different treatment of cloud microphysical processes?
    b) Can differences in Cryogenian low-level mixed-phase cloud abundance between GCMs be explained by the large-scale atmospheric state and the synoptic conditions?
    c) How does explicitly resolving moist convection impact Cryogenian subtropical cloud reflectivity?
    d) How do high concentrations of ice nucleating particles impact Cryogenian subtropical cloud reflectivity?

The structure of this chapter is as follows. First, we provide a comparison of cloud reflectivity and the conditions for cloud formation in the three GCMs (CAM, ICON-AES, and ICON-NWP) in section 6.1. Second, we use ICON-NWP and ICON-LEM to assess the impact of convection parameterizations on subtropical cloud reflectivity in section 6.2. Third, we assess the sensitivity of subtropical cloud reflectivity to the abundance of mineral dust aerosol acting as INPs in ICON-NWP and ICON-LEM simulations in section 6.3. We summarize the key results in section 6.4.

6.1. Subtropical clouds and associated reflectivity in General Circulation Models

We begin with investigating the differences in subtropical cloud reflectivity between the global coarse-scale GCMs (CAM, ICON-AES, and ICON-NWP).

Cloud reflectivity

As discussed in chapter 5, the different treatment of low-level mixed-phase clouds in CAM and ICON-AES leads to strong differences in subtropical cloud reflectivity around the ice edge (Fig. 6.1). We quantify cloud reflectivity by the shortwave cloud-radiative effect at top-of-the-atmosphere (SWCRE) calculated as the difference between all-sky and clear-sky net shortwave radiation.

Low-level cloud-tops exhibit temperatures comparable to the surface. Therefore, changes in low-level cloud amount only weakly impact the top-of-the-atmosphere energy balance via longwave radiation and are negligible regarding the stability of waterbelt states, see e.g. Fig. A.6. Hence, we here focus on SWCRE.

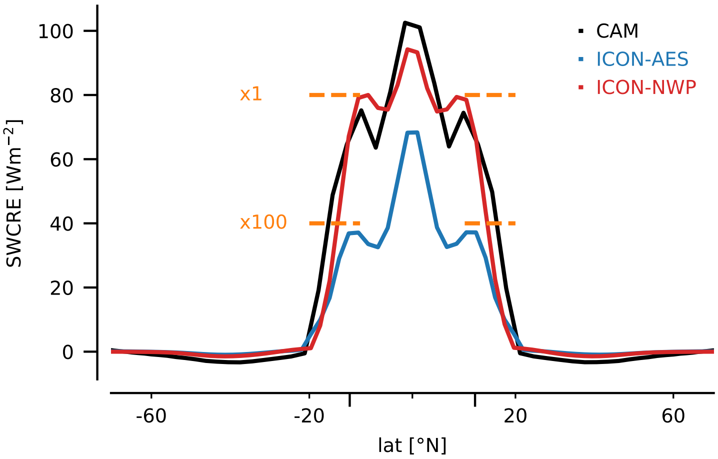

Figure 6.1.: Zonal-mean time-mean shortwave cloud-radiative effect (SWCRE) in global simulations with the GCMs CAM, ICON-AES, and ICON-NWP. Analysed periods comprise 40 years for CAM and ICON-AES and 5 years for ICON-NWP. Longer ticks around 15° latitude indicate the approximate position of the ice edge. The dashed horizontal orange lines indicate estimates of the subtropical SWCRE and the impact of increased ice nucleating particle (INP) concentrations based on NWP2.5x simulations as described in section 6.3. x1 denotes the SWCRE estimated for the reference INP concentration and x100 denotes the SWCRE estimated for a high INP concentration.

The zonal-mean time-mean SWCRE in a waterbelt climate simulated in CAM and ICON-AES is shown in Fig. 6.1. SWCRE peaks at the equator and exhibits smaller peaks in the subtropics at around 15° latitude. Poleward of 20° latitude SWCRE equals 0 Wm^{-2} because of the high albedo of snow deposited on sea ice. In ICON-AES, subtropical SWCRE is about 40 Wm^{-2} weaker compared to CAM. As shown in chapter 5, geologically relevant waterbelt states are promoted by high subtropical SWCRE in CAM and inhibited by the low subtropical SWCRE in ICON-AES.

ICON-NWP exhibits similarly high subtropical SWCRE as CAM (Fig. 6.1), which supports a Cryogenian waterbelt scenario. However, comparing two GCMs against one GCM is a narrow sample. Thus, no firm conclusions should be drawn whether high or low subtropical SWCRE can be considered more realistic. To approach this question, we study the environment of subtropical low-level clouds in the following sections.

Cloud controlling factors

We investigate whether the difference in SWCRE among the GCMs arises from differences in the large-scale environment of subtropical clouds. To this end, we study cloud controlling factors (CCFs, see e.g. (Klein et al., 2017)). We use the CCFs surface temperature T_s, pressure velocity at 500 hPa ω_{500} and lower tropospheric stability (LTS) and analyze 5-year periods based on monthly-mean data. For the CCF analysis, we use a simulation with prescribed SST and SIC for ICON-AES, because for this simulation three-dimensional data is available.

We find that differences in the amount of simulated low-level clouds are not due to differences in the large-scale atmospheric conditions captured by CCFs. This is evident from cloud cover binned by the CCFs and the frequency distributions of the CCFs shown in Fig. 6.2.

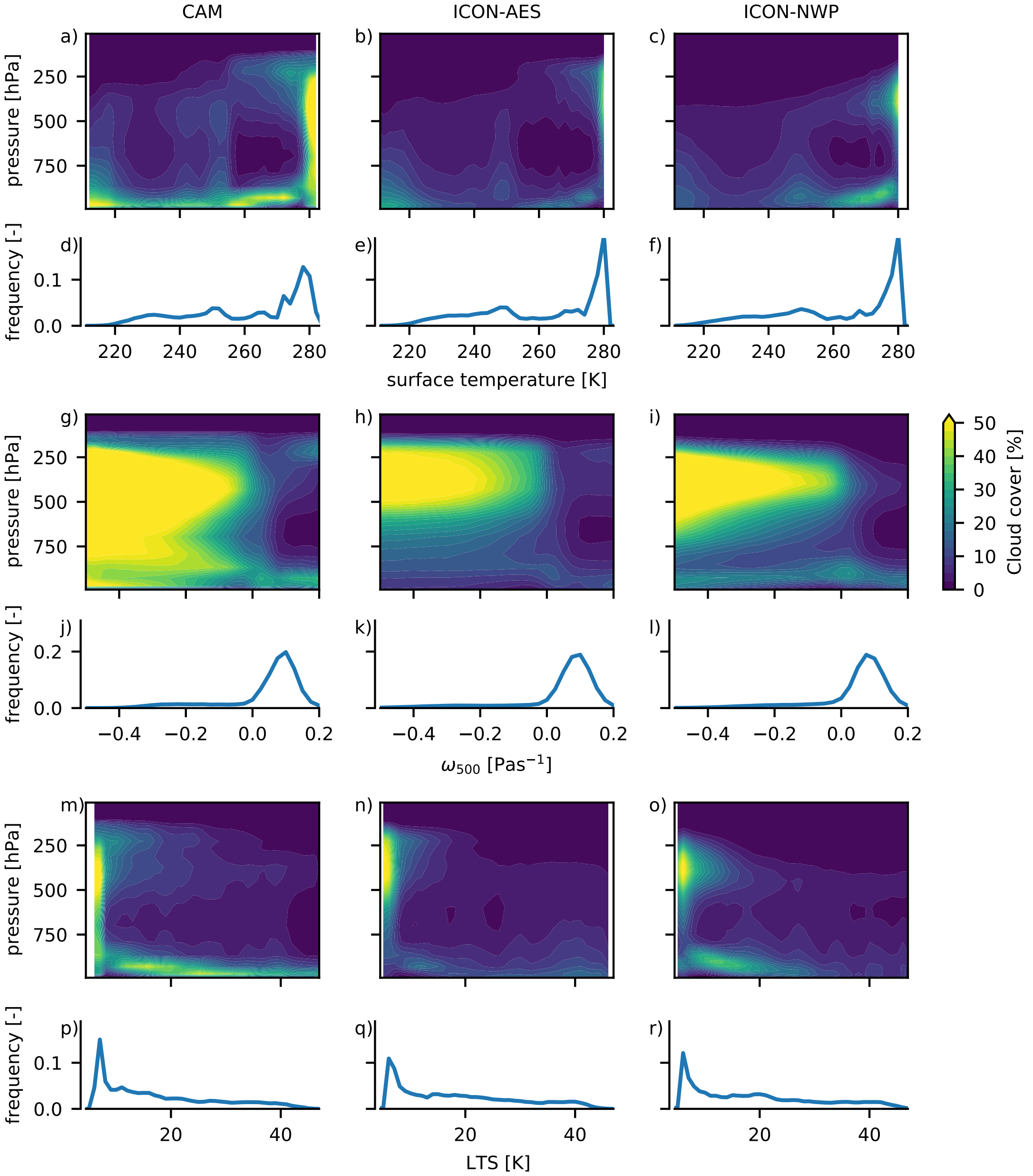

Figure 6.2.: Cloud cover binned by the cloud controlling factors (CCFs) surface temperature, pressure velocity at 500 hPa ω_{500}, and lower tropospheric stability (LTS) for CAM, ICON-AES, and ICON-NWP and the corresponding distributions of the CCFs. 5-year periods of monthly-mean data are used in between -30° to 30° latitude.

Fig. 6.2a to c, shows that CAM exhibits substantial low-level cloud cover at all T_s. In ICON-AES substantial low-level cloud cover is limited to 270 K $< T_s <$ 280 K and in ICON-NWP to $T_s >$ 260 K. In contrast to the strong differences in low-level cloud cover, the frequency distributions of T_s similarly exhibit a broad spectrum with low frequency ranging from 220 K to 270 K and a distinct peak around 280 K for all GCMs, as shown in Fig. 6.2d to f.

Fig. 6.2g to i shows that CAM and ICON-NWP exhibit low-level clouds at all ω_{500}, whereas in ICON-AES low-level cloudiness is generally weak. For all GCMs the frequency distribution of ω_{500} shows a distinct peak at 0.1 Pas^{-1}, i.e., for subsiding motion in the mid-troposphere, which traps clouds in the boundary layer (Fig. 6.2j to l).

LTS is defined as the difference of potential temperature at 700 hPa and the surface and thus quantifies the strength of the boundary-layer inversion, which is an important factor governing the presence of shallow clouds (Wood and Bretherton, 2006). All GCMs, exhibit strongest low-level cloud cover for 10 K $<$ LTS $<$ 20 K (Fig. 6.2m to o). Yet, CAM exhibits low-level clouds for any LTS. For all GCMs, the frequency distribution of LTS exhibits a pronounced peak at very low values and a widespread range of high LTS (Fig. 6.2p to r).

Overall, the frequency distributions of CCFs exhibit similar shapes and magnitudes in the three GCMs. Yet, low-level cloud abundance strongly varies. Hence, the strong SWCRE differences either arise from shorter time scales of the resolved atmospheric circulation or from parameterized sub-grid scales processes.

Synoptic conditions

We study the shorter time scales of the resolved atmospheric circulation by analyzing the synoptic conditions in the subtropical region. We first describe the characteristic synoptic conditions qualitatively and afterwards quantify their contribution to the SWCRE.

Qualitatively, subtropical cloud cover in the waterbelt climate simulated in the three GCMs is caused by a combination of large-scale subsidence, leading to shallow cloud formation, and large-scale ascent caused by baroclinic waves. This is evident from the characteristic snapshots of cloud cover and pressure velocity at 850 hPa ω_{850} shown in Fig. 6.3. We find two characteristic features:

1. a pattern of 6 to 7 branches with intense mid-level cloud cover in each hemisphere extending from the equator into the extratropics (Fig. 6.3d to f). The pattern exhibits similarities to the cloud decks observed in warm conveyor belts of extratropical cyclones in present-day climate (Madonna et al., 2014). ω_{850} also shows this pattern, which indicates that these clouds form due to large-scale ascent (Fig. 6.3j to l). We interpret this as the manifestation of baroclinic waves caused by the strong temperature difference between the warm tropical ocean and the cold extratropical sea ice.

2. homogeneous low-level cloud cover extending throughout the entire tropics and subtropics (Fig. 6.3a to c). In ICON-AES, this feature is less pronounced compared to CAM and ICON-NWP. Fig.

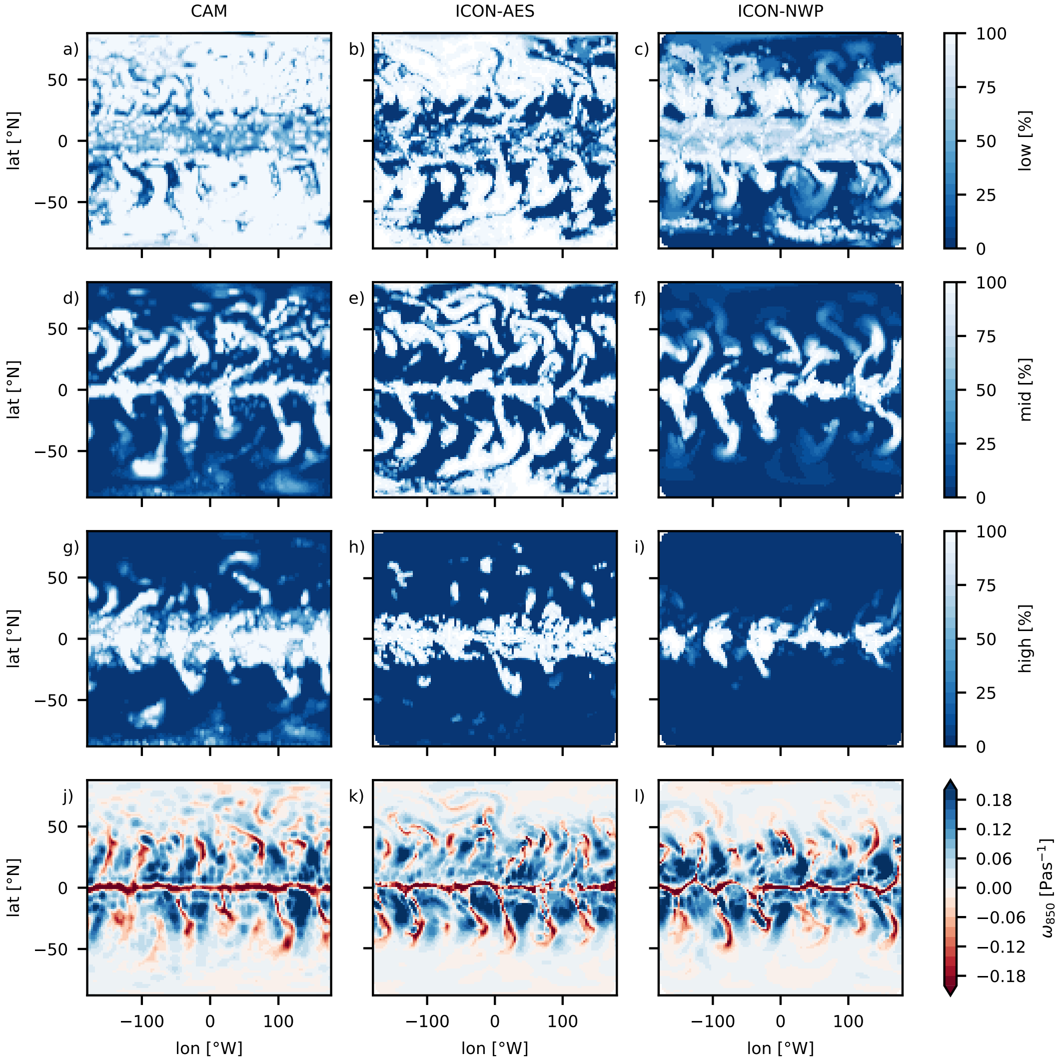

Figure 6.3.: Characteristic snapshots of cloud cover (a to i) and pressure velocity at 850 hPa ω_{850} (j to l) at a single timestep during June in CAM, ICON-AES, and ICON-NWP. Clouds below 800 hPa are defined to be low-level clouds (700 hPa in CAM) (a to c). Clouds between 800 hPa (700 hPa in CAM) and 400 hPa are defined to be mid-level clouds (d to f). Clouds above 400 hPa are defined to be high-level clouds (g to i).

6.3j to k shows that these homogeneous cloud decks coincide with large-scale subsidence. Large-scale subsidence is caused by the descending branch of the Hadley cell and creates the marine boundary-layer inversion, in which shallow low-level clouds form (Wood and Bretherton, 2006).

Quantitatively, we find that the three GCMs exhibit similar frequencies of subsidence and ascent, consistent with our CCF analysis. This is shown in Fig. 6.4a, for which we quantify the contribution of ascent and subsidence to the time-mean domain-mean SWCRE. To do so, we analyze a subdomain spanning 2.5° to 22.5° latitude South over a 30-day period based on 6-hourly data. We first exclude all data points without insolation and then filter the data by positive and negative ω_{850}. In the remainder of this manuscript SWCRE refers to the time-mean domain-mean SWCRE.

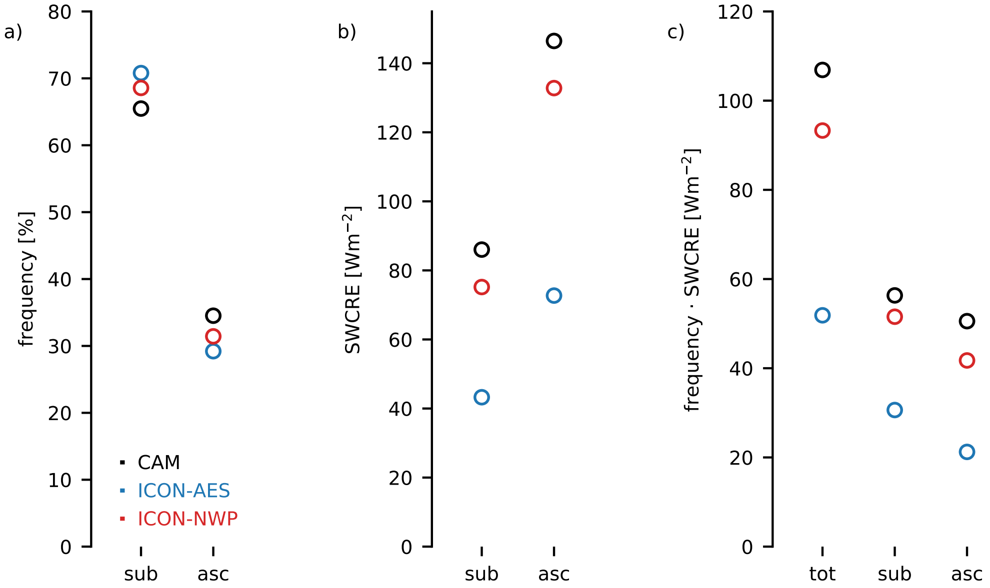

Figure 6.4.: Frequency of ascent and subsidence a), domain-mean time-mean SWCRE for areas of ascent and subsidence b), and total domain-mean time-mean SWCRE as well as contributions to total domain-mean time-mean SWCRE from areas of ascent and subsidence c). Ascent and subsidence are determined by negative and positive pressure velocity at 850 hPa. 6-hourly data in the subtropical region (22.5° to 2.5° latitude South) during one month (June) from CAM, ICON-AES, and ICON-NWP is used.

Fig. 6.4a shows that for all three GCMs the frequency of subsidence at 850 hPa is about 70 %. If calculating SWCRE in areas of ascent and subsidence separately, SWCRE is considerably larger for ascent compared subsidence (Fig. 6.4b). Fig. 6.4c provides the contributions of areas of subsidence and ascent to the total SWCRE. These contributions are the product of the SWCRE calculated separately for subsidence and ascent (Fig. 6.4b) and the corresponding frequencies (Fig. 6.4a). Areas of subsidence and ascent contribute with approximately equal shares to subtropical SWCRE with slightly stronger contributions from areas of subsidence.

In summary, we find that in the three GCMs clouds exist under similar synoptic conditions and CCFs. This reinforces that the SWCRE is sensitive to processes on scales not resolved in coarse-scale GCMs. Therefore, we study the sensitivity of the SWCRE to these unresolved processes, i.e., the treatment of convection and aerosol-cloud interactions, in the following sections.

6.2. Impact of convection parameterizations

We first investigate whether the high SWCRE found in the global coarse-scale ICON-NWP simulation in section 6.1 persists in simulations that resolve finer scales of atmospheric motion. To this end, we apply the ICON-NWP and ICON-LEM simulation hierarchy using the moderate default INP concentrations as described in section 4.5.2. The hierarchy covers horizontal resolutions Δ_h from 160 km to 300 m and gradually downscales the large-scale circulation simulated at $\Delta_h = 160$ km to smaller Δ_h. On the one hand, smaller Δ_h reduces the importance and the requirement of uncertain assumptions associated with convection parameterizations. On the other hand, our simulations at small Δ_h are located within the convective gray zone from $\mathcal{O}$(10 km) to $\mathcal{O}$(10-100m). On these scales, neither assumptions made in convection parameterizations are fully justified, nor is convection fully resolved (Sakradzija et al., 2016). Therefore, we do not consider single simulations to be more realistic than others but instead assess whether different approaches to simulate convection lead to low subtropical SWCRE.

6.2.1. ICON-NWP simulations with Δ_h from 160 km to 2.5 km

We start by comparing the global coarse-scale ICON-NWP simulation (NWP160) to the global fine-scale ICON-NWP simulation with $\Delta_h = 10$ km (NWP10). In both NWP160 and NWP10, Δ_h is considerably larger than length scales associated with convective plumes. Hence, applying the full convection scheme for shallow, mid-level, and deep convection is reasonable but entails the uncertainties associated with convection parameterizations (e.g. Sherwood et al. (2014)). At $\Delta_h = 10$ km we only simulate a 5-day period due to the computational cost. We select a representative period as described in appendix B.1.1 to relate the short period to long-term climate.

We analyze the 5-day period in NWP160 and NWP10 within the tropics and subtropics (-30° to 30° latitude). Fig. 6.5a shows that SWCRE is lower in NWP10 compared to NWP160. The difference between NWP160 and NWP10 is significantly larger than the internal variability of NWP160; the latter is given by the gray whiskers. The lower SWCRE in NWP10 compared to NWP160 results from less cloud liquid over the ice edge for a similar thermal structure of the atmosphere (Fig. 6.6a and b) and similar cloud cover (not shown).

We apply ICON-NWP in limited-area mode (LAM) to further decrease Δ_h. For simulations conducted in LAM we do not estimate internal variability, because prescribing the lateral boundary conditions enforces similar synoptic situations. However, we find that all differences discussed in the context of Fig. 6.5 are statistically significant as described in appendix B.2.2.

At $\Delta_h = 2.5$ km the bulk of convective plumes associated with deep and mid-level convection is explicitly resolved (Weisman et al., 1997). Hence, in NWP2.5 we parameterize shallow convection only. We select the representative LAM-subdomain as described in appendix B.1.2. The LAM-subdomain contains both shallow low-level clouds and mid-level clouds associated with large-scale ascent. We specifically analyse the region between 10° and 20° latitude to focus on clouds close to the ice edge and to exclude near-equatorial deep convective clouds.

Fig. 6.5b compares NWP2.5 with subsets of the simulations NWP160 and NWP10, which we here also analyze over the LAM-subdomain in between 10° and 20° latitude for the corresponding period. The reduction of SWCRE with decreasing Δ_h from 160 km to 10 km is also evident on the LAM-subdomain. Further decreasing Δ_h from 10 km to 2.5 km increases SWCRE again. In NWP2.5, SWCRE is as strong as in NWP160. The specific cross-sections in Fig. 6.7a and b show that the atmospheric thermal structure

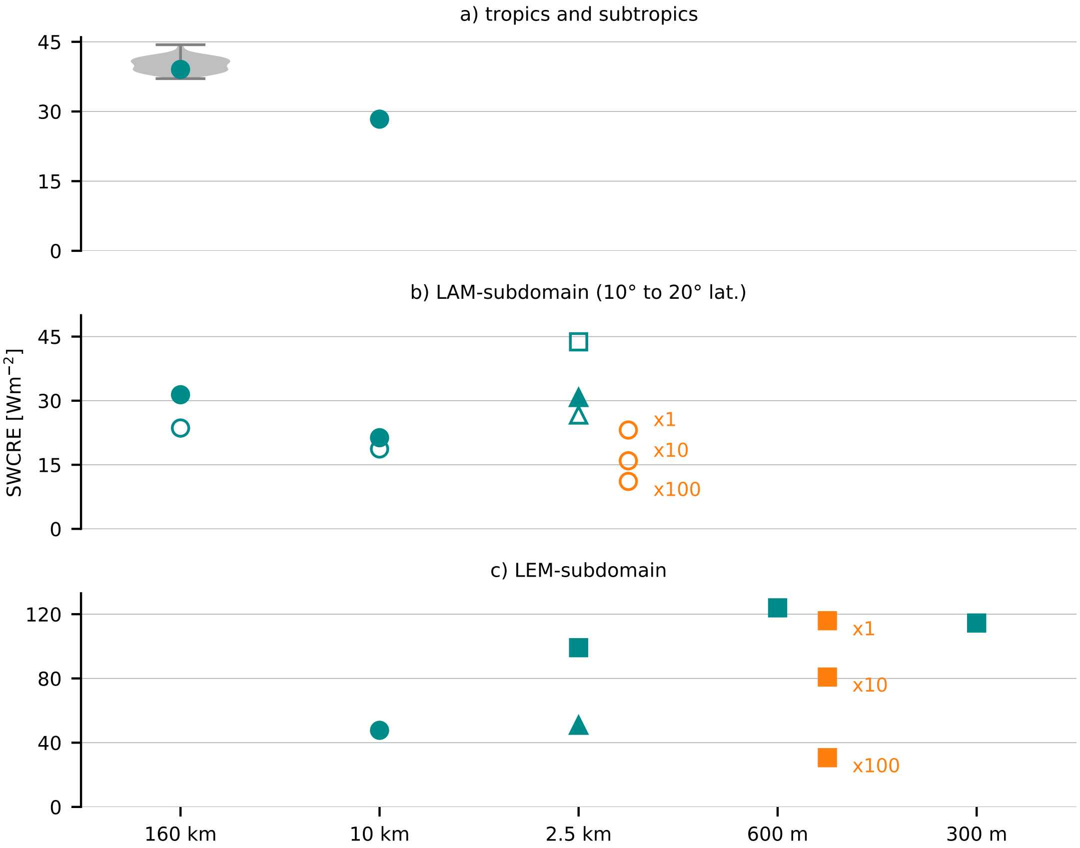

Figure 6.5.: Domain-mean time-mean shortwave cloud-radiative effect SWCRE determined from a 5-day period for the tropics and subtropics (-30° to 30° latitude) a), a 4.5-day period on the LAM-subdomain (analyzed between 10° and 20° latitude) b), and 6-hour period on the LEM-subdomain c). Circles indicate simulations with parameterizations for shallow, mid-level, and deep convection. Triangles indicate simulations with parameterizations for shallow convection and squares indicate simulations without any convection parameterization. Gray shading and whiskers in a) quantify the internal variability of NWP160. See appendix B.2.1 for details. Unfilled markers in b) indicate data analyzed for a 1.5-day period. Orange markers in b) and c) indicate simulations conducted with the heterogeneous ice nucleation parameterization by Phillips et al. (2008), in which mineral dust aerosol is increased by factors of 1, 10, and 100 as discussed in section 6.3. Note the different scales of the vertical axes.

is similar in NWP2.5 and NWP10. Yet, NWP2.5 exhibits considerably more cloud liquid than NWP10, which is presumably caused by the stronger updrafts (not shown).

$\Delta_h = 2.5$ km challenges the statistical assumptions made in the shallow convection parameterization, because the grid cells may be too small to contain robust samples of convective plumes (Sakradzija et al., 2016). Hence, we conduct an additional simulation with $\Delta_h = 2.5$ km, in which we also turn off the shallow convection parameterization (NWP2.5cex, **c**onvection **ex**plicit). This omits the limitations of the statistical assumptions in the convection parameterization. However, $\Delta_h = 2.5$ km is too large to resolve the shallow boundary layer convection and sufficiently resolve detrainment via small-scale turbulence (Lebo and Morrison, 2015). Nevertheless, simulations at $\Delta_h = 2.5$ km without convection parameterizations have been used to study the sensitivity of cloud-radiative effects to the treatment of convection (see e.g. Stevens et al. (2020); Hohenegger et al. (2020); Senf et al. (2020)).

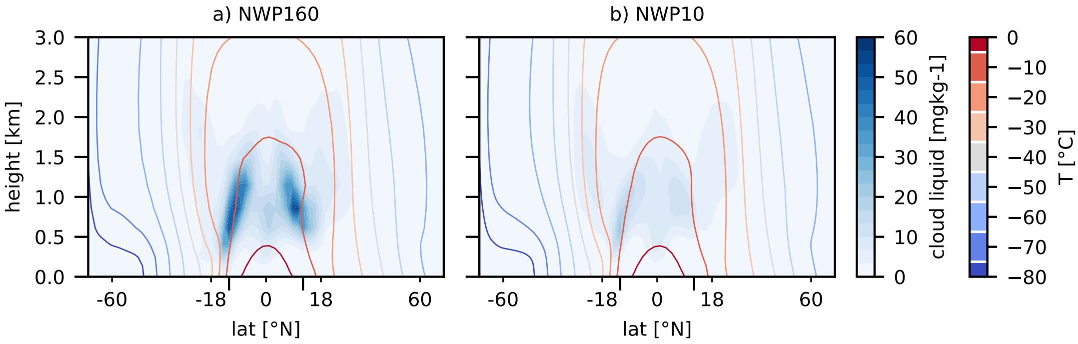

Figure 6.6.: Zonal-mean time-mean specific cloud liquid mass indicated by shading and isothermes of air temperature T indicated by contours determined from a 5-day period of simulations at a) $\Delta_h = 160$ km (NWP160) and b) $\Delta_h = 10$ km (NWP10). Longer ticks indicate the position of the ice-edge.

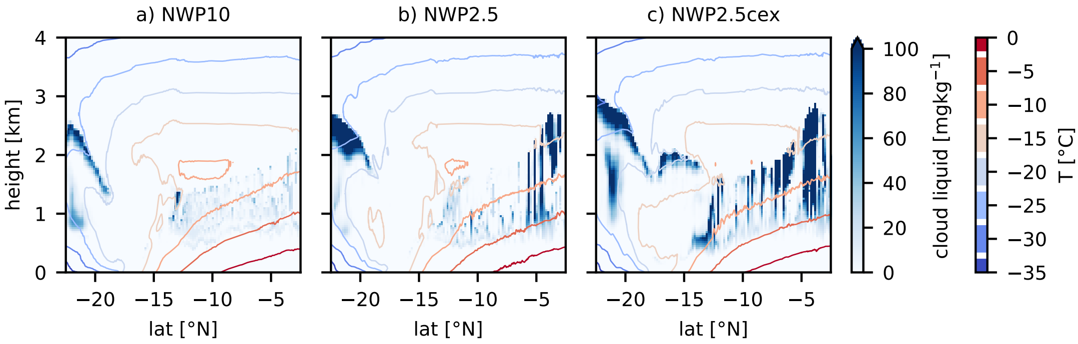

Figure 6.7.: Meridional cross sections at a single time step at 123° longitude showing specific cloud liquid mass indicated by shading along with isothermes of air temperature T indicated by contours. The ICON-NWP simulations were conducted a) at $\Delta_h = 10$ km (NWP10), b) at $\Delta_h = 2.5$ km with parameterized convection (NWP2.5), and c) at $\Delta_h = 2.5$ km with explicitly resolved convection (NWP2.5cex).

Turning off the shallow convection parameterization at $\Delta_h = 2.5$ km strongly increases SWCRE. This is evident when comparing NWP2.5cex with the first 1.5 days from NWP160, NWP10, and NWP2.5 on the LAM-subdomain (unfilled cyan markers in Fig. 6.5b). The strong increase of SWCRE is likely caused by underestimated detrainment rates in NWP2.5cex.

Consistently, Fig. 6.7 shows that in NWP2.5cex cloud liquid is more abundant and more widespread compared to NWP10 and NWP2.5, i.e., NWP2.5cex exhibits cloud liquid, where NWP10 and NWP2.5 do not exhibit any cloud. In Fig. 6.7 this is the case at -17 ° latitude at around 2 km altitude. Here, cloud longwave radiative warming alters the thermal structure of the boundary layer compared to NWP2.5 as further discussed in section 6.2.2.

Overall, the high SWCRE found in NWP160 persists if reducing Δ_h in ICON-NWP. NWP10 exhibits lower SWCRE than NWP160 (Fig. 6.5a) but the difference is much smaller than between ICON-NWP and ICON-AES, where the difference in subtropical SWCRE is 50 % (Fig. 6.1). In the following, we assess whether the high SWCRE persists if we further decrease Δ_h in ICON-LEM simulations.

6.2.2. ICON-LEM simulations with Δ_h of 600 m and 300 m

Shallow boundary-layer clouds are stronger impacted by hectometer-scale convective processes than clouds associated with the large-scale ascent caused by cyclonic events. Therefore, we focus our ICON-LEM simulations on a shallow cloud deck over the ice edge.

We conduct ICON-LEM simulations in LAM with $\Delta_h = 600$ m (LEM0.6) and simultaneous online one-way grid nesting with $\Delta_h = 300$ m (LEM0.3). We select a suitable subdomain for LEM0.6 as described in section B.1.3. A large fraction of this subdomain is covered by low-level clouds (Fig. 6.8a and b). Mid-level clouds caused by large-scale ascent are only present in the southwest corner of the subdomain (Fig. 6.8c and d). High-level cloud cover is negligible (not shown).

We assume that convection is explicitly resolved in LEM0.6 and LEM0.3. On the one hand, large-eddy simulations with $\Delta_h = 300$ are far from resolving length scales $\mathcal{O}(10\text{ m})$ required for an accurate explicit simulation of shallow clouds (Stevens et al., 2002). On the other hand, the largest convective eddies within the boundary layer exhibit length scales on the order of the boundary-layer height, which is about 1.8 km in our simulations. Hence, the large scales of the boundary layer circulation can be represented in LEM0.6 and LEM0.3.

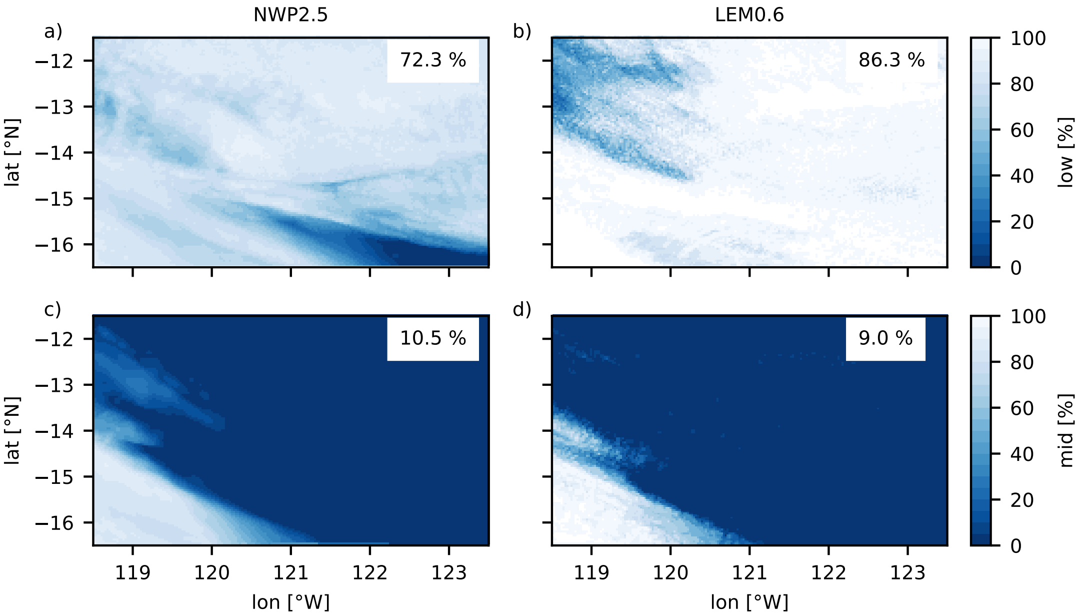

Figure 6.8.: Low-level (top) and mid-level (bottom) cloud cover averaged over 6-hour periods over the LEM-subdomain in simulations NWP2.5 (a and c) and LEM0.6 (b and d).

Fig. 6.5c compares SWCRE from LEM0.6 and LEM0.3 on the LEM-subdomain LEM with simulations NWP10, NWP2.5, and NWP2.5cex, which we here analyze over the same subdomain and the corresponding period. SWCRE in LEM0.6 and LEM0.3 is higher than in NWP2.5cex and exceeds SWCRE in NWP2.5 and NWP10 by more than 100 %.

The differences between NWP2.5, NWP2.5cex, LEM0.6, and LEM0.3 are analyzed in Fig. 6.9 by means of time-mean domain-mean vertical profiles. The profiles of specific humidity q_v indicate that the shallow boundary layer clouds are supplied with moisture from the surface (Fig. 6.9a). The near-surface increase of relative humidity (Fig. 6.9b) at constant q_v indicates adiabatic cooling. Beyond 400 m altitude cloud liquid and ice forms consuming q_v. The top of the boundary layer at around 1.8 km height is marked by the strong decrease of q_v and the increase of equivalent potential temperature θ_e (Fig. 6.9c). The dry, warm air aloft is caused by large-scale subsidence. Although the q_v profiles exhibit a similar structure, the profiles of cloud liquid and ice differ substantially in magnitude and shape (Fig. 6.9d and e).

LEM0.6 and LEM0.3 exhibit high amounts of cloud liquid while NWP2.5 and NWP2.5cex exhibit high amounts of cloud ice. This is consistent with more intense updrafts in ICON-LEM (Fig. 6.9f). We calculate updraft intensity as the domain-mean time-mean over all grid points with upward velocity. Higher updraft intensity leads to higher relative humidity in between 0.5 to 1.5 km altitude (Fig. 6.9b), which facilitates the formation of cloud liquid. However, the higher updraft intensity in LEM0.3 compared to LEM0.6 does not lead to higher amounts of cloud liquid, indicating stronger detrainment in LEM0.3.

The shapes of the vertical profiles point towards different dominant cloud types. In ICON-LEM, the approximately linear increase of cloud liquid with altitude and the constant relative humidity between 0.5 to 1.5 km altitude indicate liquid water production at low lateral dry air entrainment rates. This suggests stratocumulus clouds as the dominant cloud type (Rauterkus and Ansorge, 2020). In contrast, the relatively constant profiles of cloud liquid in NWP2.5 and NWP2.5cex indicate considerable lateral entrainment. This suggests dominance of shallow cumulus clouds (de Rooy et al., 2013).

NWP2.5 exhibits particularly low cloud liquid and a pronounced peak of cloud ice below 1 km altitude (Fig. 6.9). This may be caused by an amplifying feedback of reduced longwave surface warming leading to reduced surface temperatures and reduced surface moisture supply. In less idealized model setups with interactive sea ice, this longwave warming feedback might impact the expansion of sea ice, as suggested by Poulsen and Jacob (2004).

NWP2.5cex exhibits a pronounced peak of cloud liquid and ice above the boundary layer at 2 km altitude (Fig. 6.9d). As discussed in section 6.2.1, detrainment rates are likely underestimated in NWP2.5cex, which may allow convective shafts to penetrate into the free troposphere (Lebo and Morrison, 2015). The associated excessive cloud liquid formation warms the boundary layer as shown in Fig. 6.7. This weakens the boundary-layer inversion as is evident from the θ_e profile in Fig. 6.9c, which additionally facilitates cloud formation above the boundary layer.

Overall, our hierarchy across horizontal resolutions indicates that the treatment of convection considerably impacts subtropical Cryogenian SWCRE, especially within the gray zone of convection. The strong impact of convection treatment was also reported in studies of present-day climate (Stevens et al., 2020; Senf et al., 2020). Even though all our simulations have limitations concerning the representa-

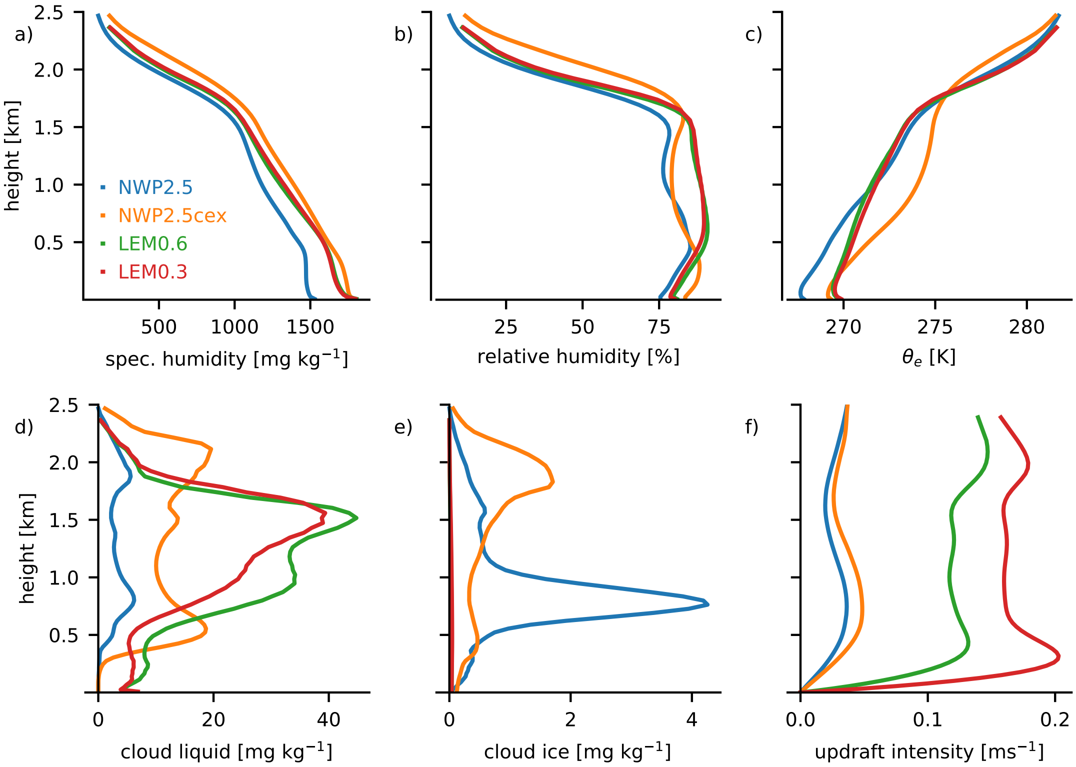

Figure 6.9.: Domain-mean time-mean vertical profiles of specific humidity a), relative humidity b), equivalent potential temperature θ_e c), specific cloud liquid d), specific cloud ice e), and updraft intensity f) determined from a 6-hour period on the LEM-subdomain for ICON-NWP simulations at $\Delta_h = 2.5$ km with shallow convection parameterized (NWP2.5) and explicitly resolved (NWP2.5cex) and ICON-LEM simulations at $\Delta_h = 600$ m and $\Delta_h = 300$ m (LEM0.6 and LEM0.3).

tion of convection, we find that the dynamical environment of shallow low-level clouds allows a high subtropical SWCRE irrespective of the specific treatment of convection.

We point out that both the INP concentration and the CCN concentration are expected to impact SWCRE. The high SWCRE in our hierarchy of simulations is found using the default INP and CCN configurations of ICON, which represent moderate INP concentrations and fairly high CN and thus CCN concentrations. In marine environments, CCN concentrations may be considerably lower than what is assumed here (Segal and Khain, 2006). According to Twomey (1977), low CCN concentrations lead to fewer and larger cloud droplets and thus weaker SWCRE. However, we here focus on the impact of varying the INP concentration, which we study in section 6.3.

6.3. Sensitivity of cloud reflectivity to the abundance of ice nucleating particles

In this section we investigate the sensitivity of cloud reflectivity to the abundance of INPs. We here choose to focus on a scenario considering high abundance of mineral dust aerosol and study its impact on ice formation and the WBF process.

Cryogenian mineral dust ice nucleating particles

During the Cryogenian, soil erodibility likely was high due to the absence of land plants (Morris et al., 2018; Liu et al., 2020). Liu et al. (2020) conducted GCM simulations of temperate Cryogenian climate with interactive dust aerosol and assuming high soil erodibility. They found a global-mean atmospheric dust loading up to 40 times higher than in present-day climate. Model estimates by Abbot and Halevy (2010) assuming a Snowball climate even suggest that atmospheric dust loading was 100 times higher than in present-day climate. Given that mineral dust aerosols are the dominant ice-nucleating species in present-day climate (Kanji et al., 2017), we neglect all ice-nucleating species except mineral dust. To do so, we apply the heterogeneous ice nucleation parameterization by Phillips et al. (2008), referred to as the dust-only parameterization, instead of the default parameterization by Hande et al. (2015). This allows us to explicitly set the number concentration of specific aerosol species for heterogeneous ice formation. To isolate the impact of modifying the INP concentration, we leave the treatment of CCN unchanged.

The dust-only heterogeneous ice nucleation parameterization includes immersion and depositional freezing. It considers a constant, homogeneous aerosol number concentration n_a. The INP concentration is determined by n_a, air temperature, and supersaturation with respect to ice. We set $n_a = 0$ for all aerosol species except mineral dust and assume a reference dust aerosol concentration $n_a = 700\ \mathrm{L}^{-1}$. This assumption results in a maximum INP concentration at -20 °C on the order of 1 L^{-1}, which is roughly the median of values expected on present-day Earth (Kanji et al., 2017). At -20 °C the dust-only parameterization yields a higher maximum INP concentration than the default parameterization by Hande et al. (2015), for which the maximum concentration is 0.1 L^{-1} at the same temperature. However, the variation of the INP concentration with air temperature and supersaturation differs between the two parameterizations and the dust-only parameterization does not necessarily result in an overall higher atmospheric abundance of INPs. For our purposes it is important to note that the transition from the default heterogeneous ice nucleation parameterization to the dust-only parameterization only weakly affects SWCRE at $\Delta_h = 2.5$ km and 600 m. This is shown by the cyan and orange marker labelled by x1 in Fig. 6.5b and c.

Given the high estimates of the global-mean atmospheric dust loading under Cryogenian conditions we increase n_a by factors of 10 and 100. If the atmospheric state is the same, increasing n_a by a factor of 100 leads to an INP concentration of 100 L^{-1} at -20 °C. This is an extreme value under present-day climate conditions, but in our opinion justifiable given under Cryogenian conditions.

Simulations with increased concentrations of mineral dust ice nucleating particles

We investigate the impact of increasing the INP concentration on SWCRE using ICON-NWP at $\Delta_h = 2.5$ km with parameterized shallow convection over the LAM-subdomain (simulation set NWP2.5x) and ICON-LEM at $\Delta_h = 600$ m over the LEM-subdomain (simulation set LEM0.6x). This allows us to investigate the sensitivity of SWCRE to INP concentrations for different synoptic conditions and different treatments of convection. For each set of simulations we conduct a reference simulation with $n_a = 700$ (referred to as x1) and simulations with n_a increased by factors of 10 (x10) and 100 (x100).

We first investigate the impact of increasing the INP concentration using the set of LEM0.6x simulations and the corresponding time-mean domain-mean vertical profiles shown in Fig. 6.10. An increased INP concentration leads to an increased heterogeneous ice formation rate, which is dominated by immersion freezing in mixed-phase clouds (Kanji et al., 2017). More intense heterogeneous ice nucleation leads to a larger ice crystal number concentration, which enhances water vapor deposition onto ice crystals at altitudes above 400 m (Fig. 6.10c). In contrast, at altitudes below 400 m, ice crystals sublimate due to the relatively low relative humidity in the below-cloud layer (cf. Fig. 6.9b). The enhanced vapor deposition above 400 m indicates enhanced liquid-ice conversion via the WBF process, which strongly depletes liquid at the expense of ice. In our current model setup, ice crystals have a larger terminal fall speed and tend to precipitate more easily than rain drops. Hence, accumulated precipitation at the surface increases (Fig. 6.10f) and total cloud condensate decreases. Overall, cloud liquid strongly decreases with larger INP concentrations. Sublimation and vapor deposition impact the size of ice crystals. However, changes in the ice crystal size are not considered in the radiation scheme. Thus, the changes in cloud liquid determine the impact of the cloud microphysical processes on SWCRE.

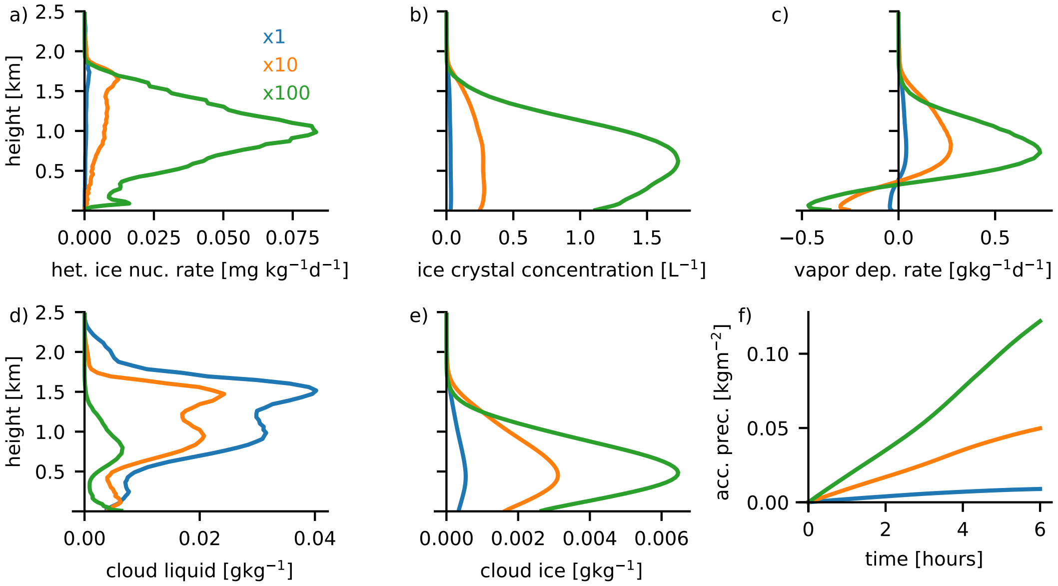

Figure 6.10.: Domain-mean time-mean profiles of heterogeneous ice nucleating rate a), ice crystal number concentration b), rate of vapor deposition onto ice crystals c), specific cloud liquid d), specific cloud ice e), and accumulated precipitation at the surface f) in ICON-LEM simulations with concentrations of ice nucleating particles increased by factors of 1, 10, and 100 (simulations LEM0.6x). Data is analyzed for a 6-hour period over the LEM-subdomain.

The strong decrease of cloud liquid with increasing INP concentration leads to a strong decrease in SWCRE in the LEM0.6x simulations as shown in Fig. 6.11 and the orange markers in Fig. 6.5c. SWCRE decreases by more than 90 Wm^{-2} when increasing n_a by a factor of 100. This is a relative

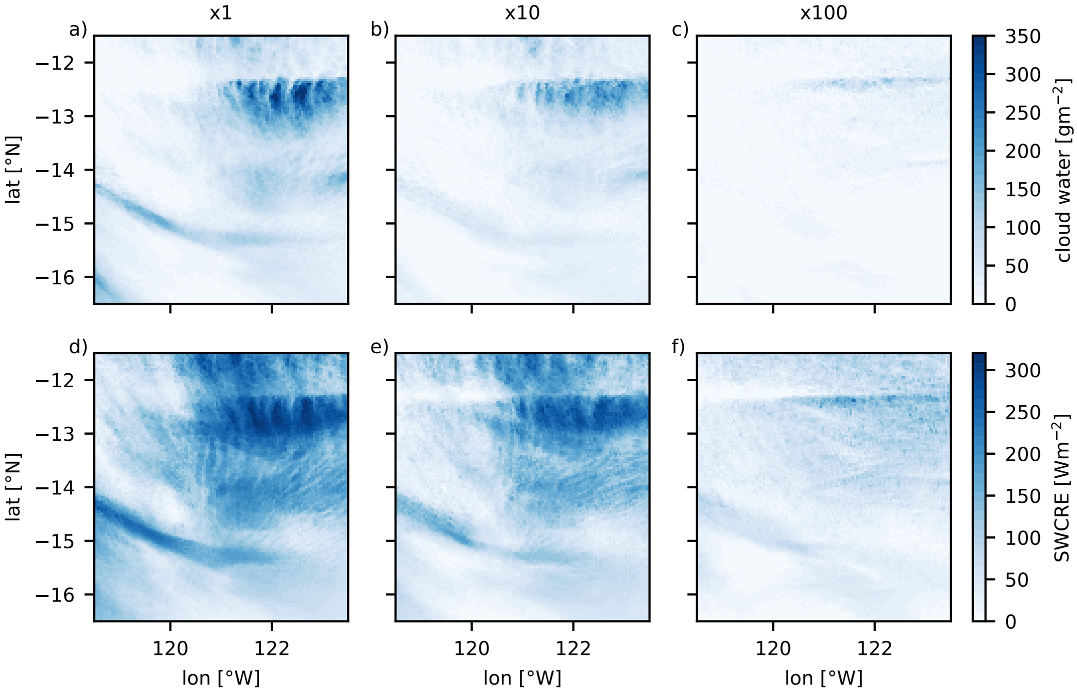

Figure 6.11.: Vertically integrated cloud liquid a) to c) and shortwave cloud-radiative effect (SWCRE) at top-of-the-atmosphere d) to f) averaged over 6-hour periods over the LEM-subdomain in ICON-LEM simulations with increased concentrations of ice nucleating particles. (left) LEM0.6x1, (middle) LEM0.6x10, and (right) LEM0.6x100.

SWCRE decrease by more than 75 %. This decrease exceeds the differences found in SWCRE due to the treatment of convection found in Fig. 6.5. We also find a decrease of SWCRE in ICON2.5x simulations on the LAM-subdomain (Fig. 6.5b). The absolute decrease of SWCRE in ICON2.5x is considerably smaller compared to LEM0.6x, because NWP2.5 exhibits less cloud liquid than LEM0.6. However, SWCRE decreases by 50 % if comparing NWP2.5x1 with NWP2.5x100, which is as large as the differences found due to the treatment of convection (Fig. 6.5b).

Overall, we find that SWCRE is strongly reduced in the presence of high INP concentrations. This holds for NWP2.5x and LEM0.6x, which represent different synoptic conditions and parameterize and resolve shallow convection, respectively. Our results are in agreement with simulations of mixed-phase stratocumulus and cumulus clouds under present-day climate conditions by Vergara-Temprado et al. (2018). These clouds are located in the cold sector of extratropical cyclones over the Southern Ocean. Based on simulations with 2 km horizontal grid spacing, Vergara-Temprado et al. (2018) estimated that SWCRE could range from 42 to 105 Wm^{-2} due to variations of the INP concentration. In present-day climate the abundance of mineral dust aerosol over the Southern Ocean is generally low due to the large distance to continental regions (Vergara-Temprado et al., 2018). Consistently, the impact of particularly varying mineral dust aerosol concentrations on stratiform mixed-phase clouds over the Southern Ocean is low under present-day climate conditions (McGraw et al., 2020). Yet, Sagoo and Storelvmo (2017) stated a significant impact of mineral dust aerosol on the SWCRE of mixed-phase clouds in simulations with climatic conditions representing the last glacial maximum 20,000 years before present.

The high sensitivity of SWCRE to INP concentrations in our simulations implies that high INP concentrations may hamper the existence of stable waterbelt states. This is evident if we estimate the impact of the high sensitivity of SWCRE to INP concentrations on the global scale as indicated by the dashed orange lines in Fig. 6.1. The estimate is based on two assumptions. First, we assume that SWCRE in the subtropical region is as high as in NWP160 if using the reference dust-only INP concentration. This assumption is supported by the equal SWCRE in NWP2.5x1 and NWP160 shown in Fig. 6.5b. We approximate subtropical SWCRE for the reference case to be 80 $\mathrm{Wm^{-2}}$ (dashed orange line x1 in Fig. 6.1). Second, we assume that the 50 % reduction of SWCRE with increasing n_a by 100 found in 2.5x simulations (x1 vs. x100 in Fig. 6.5b) is representative for the entire subtropical region. This assumption is based on our choice of representative subdomains and periods. Applying the 50 % reduction of SWCRE yields a subtropical SWCRE of 40 $\mathrm{Wm^{-2}}$ (x100 in Fig. 6.1). This is close to the SWCRE found in ICON-AES, for which climate does not stabilize in a waterbelt state as shown in chapter 5. Hence, high but still plausible INP concentrations may hamper the existence of waterbelt states. As a consequence, the existence of stable waterbelt states may be determined by the abundance of mineral dust aerosol.

However, the abundance and distribution of mineral dust aerosol during the initiation of the Cryogenian glaciations is highly uncertain, as it is determined by several factors. First, despite the absence of land vegetation, crust formation potentially lead to low soil erodibility (Liu et al., 2020). Second, the distribution of INPs likely exhibited high spatial variability. GCM simulations by Liu et al. (2020) indicated that Cryogenian maritime regions, where the impact of INPs on shallow mixed-phase cloud reflectivity is crucial, exhibited low dust aerosol concentrations. Third, on the way towards a Snowball climate, the extent of land glaciers, which strongly depends on topography (Rodehacke et al., 2013; Walsh et al., 2019), determined the continental area emitting dust. Fourth, dust may sediment into sea ice at high latitudes and subsequently be transported within the sea ice towards the equator (Hoffman, 2016). Accordingly, mineral dust might be exposed due to surface net evaporation in the subtropical region, just in the right spot to impact cloud reflectivity above the ice edge.

Given our limited knowledge concerning Cryogenian aerosol scenarios, varying aerosol concentrations by a factor of 100 in our view is justified. The corresponding differences in SWCRE are equal to or even exceed the differences arising from the treatment of convection. Hence, even if convection and turbulence were properly represented in the model simulations, limited knowledge concerning Cryogenian aerosol composition and abundance precludes a robust judgement of the plausibility of waterbelt scenarios.

6.4. Discussion and conclusions

As shown in chapter 5 the existence of stable Cryogenian waterbelt states requires that subtropical low-level mixed phase clouds are highly reflective. Here we investigate to what extent the cloud reflectivity depends on the treatment of convection and the assumed concentration of INPs. In particular, we seek if high-resolution models with explicit convection support highly reflective clouds, and how this is modulated by INPs.

We show that the radiative properties of Cryogenian mixed-phase clouds are governed by processes that are strongly parameterized in coarse-scale general circulation models (GCMs) such as convection and aerosol-cloud interactions. High-resolution simulations allow us to explicitly resolve convective-scale motions and improve the representation of aerosol-cloud interactions. We gradually reduce the dependency on parameterized sub-grid scale processes through a hierarchy of simulations ranging from horizontal grid spacings of 160 km to 300 m assuming moderate INP concentrations. Particularly our large-eddy simulations with explicitly resolved convection promote a high abundance of supercooled liquid and thus highly reflective clouds. Although we find that cloud reflectivity depends on the treatment of convection, the hierarchy of simulations overall supports highly reflective subtropical clouds.

We further study the impact of increasing the INP concentration from moderate to high plausible values under Cryogenian conditions. Increasing the INP concentration enhances the Wegener-Bergeron-Findeisen process and strongly reduces supercooled liquid. The associated reduction of cloud reflectivity is larger than the differences found due to the treatment of convection. The high sensitivity of cloud reflectivity to the INP concentration indicates that the existence of stable waterbelt states may be determined by the abundance of mineral dust aerosol. This extends the importance of mineral dust aerosol for Cryogenian climate beyond its direct radiative effect (Abbot and Halevy, 2010; Liu et al., 2020, 2021).

Cryogenian aerosol conditions and the associated impact on cloud reflectivity are highly uncertain. In general, cloud microphysical processes strongly impact cloud reflectivity. Thus, poorly constrained microphysical processes not addressed in this study, such as cloud droplet formation (Lee et al., 2013), secondary ice formation (Field et al., 2017), and the nucleation efficiency of INPs (Hoose and Möhler, 2012) add to the cloud uncertainty. Therefore, we cannot constrain Cryogenian cloud reflectivity to either high or low values, and both the presence of the absence of waterbelt states in the real climate system remain possible. Given the high sensitivity of cloud reflectivity to the treatment of convection and the abundance of INPs, constraining Cryogenian cloud reflectivity requires simulations at relatively high resolutions as well as extending our knowledge regarding the treatment of cloud microphysical processes and Cryogenian aerosol conditions.

Thus, so far, the Jormungand-waterbelt scenario remains an uncertain explanation for the Cryogenian glaciations. The uncertainty not only exists in coarse-scale GCMs due to uncertain tuning parameters, but persists in hectometer-scale large-eddy simulations with reduced model assumptions. Here, the uncertainty associated with Cryogenian aerosol conditions hampers a judgement whether Earth's climate may have settled in a waterbelt state. Thus, with the current state of knowledge we consider the more robust classical Snowball Earth scenario a more likely explanation for the Cryogenian glaciations.

7. Summary, Conclusions and Outlook

Parts of this chapter are based on Braun et al. (2022a) and Braun et al. (2022b).

In this chapter, we first summarize the answers to our research questions as well as the novelty and implications of our results in section 7.1. We further provide an outlook in section 7.2.

7.1. Summary and Conclusions

Waterbelt climate states with an ice-free tropical ocean were considered as alternative scenarios to the well-established Snowball Earth scenario for the Cryogenian glaciations (720 to 635 Ma) that drastically impacted the conditions for the evolution of life (Hoffman et al., 2017; Hyde et al., 2000; Abbot et al., 2011; Rose, 2015). Scenarios involving a waterbelt climate are appealing because they allow one to easily explain the survival of demosponges throughout the Marinoan glaciation (640 to 635 Ma) (Love et al., 2009). Among the proposed waterbelt scenarios, the so-called Jormungand hypothesis is particularly attractive as it proposes an entire life cycle of the glaciations and rests on well-established atmospheric dynamics and physics (Abbot et al., 2011).

Since the postulation of the Jormungand hypothesis by Abbot et al. (2011), several modeling studies that used comprehensive, fully-coupled ocean-atmosphere GCMs have addressed the existence of waterbelt states based on the Jormungand mechanism (Voigt and Abbot, 2012; Rose, 2015; Pollard et al., 2017). However, so far no coherent chain of arguments emerged from the efforts to answer the overarching question whether the Jormungand hypothesis is a viable alternative to the Snowball Earth hypothesis. Previous work recognized clouds as a potentially important feature of Cryogenian climate but so far no study explicitly addressed the role of clouds in the context of the Jormungand hypothesis.

In this thesis, we investigate the role of clouds for the robustness of the Jormungand hypothesis in idealized aquaplanet setups in GCMs. The idealized setup allows us to focus on the central mechanism of the Jormungand hypothesis, i.e., the weakening of the ice-albedo feedback due to the presence of dark subtropical sea ice. We implement the aquaplanet setup in ICON-AES by coupling a thermodynamic sea-ice scheme and a thermodynamic mixed-layer ocean. The specific impact of the sea-ice scheme was studied in Hörner et al. (2022)[1]. We conduct simulations with the global GCMs ICON-AES and CAM and calculate corresponding bifurcation diagrams of the Earth system. We demonstrate the impact of clouds on the Jormungand hypothesis in GCMs, by implementing a cloud-radiation modification in CAM and altering cloud microphysical processes in ICON-AES. We interpret the GCM results using a one-dimensional energy balance model, for which we estimate the key parameters from our GCM simulations.

Furthermore, we study controls on Cryogenian subtropical clouds in a hierarchy of simulations that covers horizontal grid spacings from 160 km to 300 m using ICON in numerical weather prediction mode and large-eddy mode. To our knowledge our large-eddy simulations that are driven by a freely evolving atmospheric state under Cryogenian waterbelt conditions are the first simulations of their kind conducted under such extreme climate conditions. Additionally, we conduct simulations, in which we vary the abundance of mineral dust aerosol acting as ice nucleation particles.

We addressed our research questions and the corresponding sub-questions in chapters 5 and 6. We here provide the key results that answer our research questions. The key results answering research question 1 and the corresponding sub-questions are as follows.

1. **Is the Jormungand-waterbelt scenario a robust feature of Earth's climate?**
   No. Our GCM simulations show that geologically relevant Jormungand-waterbelt states do not naturally emerge from GCM simulations. This is the case because the central mechanism of the Jormungand hypothesis, i.e., the weakening of the ice-albedo feedback due to dark subtropical sea ice, is less reliable than previously thought. The subtropical weakening of the ice-albedo feedback critically depends on the reflectivity of subtropical clouds, which is uncertain in GCMs.

   a) **Are geologically relevant Jormungand-waterbelt states a robust feature of idealized aquaplanet simulations?**
   No. A geologically relevant Jormungand-waterbelt state does not exist in ICON-AES simulations with the default configuration of the Wegener-Bergeron-Findeisen process. A stable waterbelt state does exist in this configuration of ICON-AES. However, this waterbelt state does not satisfy the criteria for geological relevance, i.e., the waterbelt state exists over a very limited range of atmospheric CO_2 concentrations and is not accessible from the temperate state.

   b) **Under which conditions do geologically relevant Jormungand-waterbelt states exist in idealized aquaplanet simulations?**
   For values of snow and bare sea-ice albedo as suggested by Abbot et al. (2011), i.e., for relatively dark bare sea-ice, we find geologically relevant Jormungand-waterbelt states in idealized aquaplanet simulations if subtropical cloud reflectivity is high. Evidence that

---

[1] The article Hörner et al. (2022) resulted from the Master thesis of Johannes Hörner, which I co-supervised during my PhD.

high subtropical cloud reflectivity is a prerequisite for the existence of geologically relevant Jormungand-waterbelt states consistently arises from i) the comparison of CAM and ICON-AES in their default configurations, from ii) explicitly reducing subtropical cloud reflectivity in CAM pCOOKIE simulations, and from iii) implicitly increasing subtropical cloud reflectivity in ICON-AES WBF simulations with decreased efficiency of the Wegener-Bergeron-Findeisen process. In the waterbelt climate subtropical cloud reflectivity is determined by the abundance of supercooled liquid in low-level mixed-phase clouds.

c) How do these conditions link to the weakening of the ice-albedo feedback in the subtropical region, which constitutes the core of the Jormungand hypothesis?
The key factor that determines the magnitude of the subtropical ice-albedo feedback is the ratio of the planetary albedo over ice-free ocean to the planetary albedo over bare sea ice. The planetary albedo over ice-free ocean is determined by subtropical cloud reflectivity. The ice-albedo feedback is sufficiently weak to allow for the existence of a geologically relevant waterbelt state if the ice-free ocean albedo is not substantially smaller than the bare sea-ice albedo. Hence, unless assuming very low values of bare sea-ice albedo, the existence of geologically relevant Jormungand-waterbelt states requires cloud reflectivity to be sufficiently high. We demonstrate this effect using a one-dimensional energy balance model, which yields results that are consistent with our GCM simulations.

d) Can we expect these conditions to be achieved during the Cryogenian?
Yes, these conditions can be achieved but our results suggest that it is rather unlikely that these conditions indeed prevailed during the Cryogenian periods. CAM and ICON-AES simulations with plausible values for subtropical cloud reflectivity and bare sea-ice albedo support the existence of geologically relevant Jormungand-waterbelt states. However, geologically relevant waterbelt states only exist if subtropical cloud reflectivity is at the upper end of its plausible range and if simultaneously bare sea-ice albedo is at the lower end of its plausible range. Hence, the existence of geologically relevant Jormungand-waterbelt states is confined to a narrow space of the critical parameters, i.e., subtropical cloud reflectivity and bare sea-ice albedo. Moreover, subtropical cloud reflectivity strongly differs between CAM and ICON-AES, indicating the well-known uncertainties associated with representing low-level mixed-phase clouds in present-day climate (Zelinka et al., 2020).

In chapter 6, we addressed research question 2 and the corresponding sub-questions. The key results answering these research questions are as follows.

2. **Can we rule out the Jormungand hypothesis in idealized aquaplanet simulations due to the critical role of subtropical cloud reflectivity?**
No. We would be able to rule out the Jormungand hypothesis on a cloud-based argument if we

could show that Cryogenian cloud reflectivity was low. We identify the high abundance of mineral dust acting as ice nucleating particles as a potential cause for weakly reflective subtropical clouds. However, the uncertainty associated with specific Cryogenian aerosol scenarios and cloud microphysical processes is too high as to qualify the high abundance of ice nucleating particles to stringently constrain cloud reflectivity to low values.

a) **How does Cryogenian subtropical cloud reflectivity compare among three GCMs with different treatment of cloud microphysical processes?**

The annual-mean subtropical cloud reflectivity as quantified by the shortwave cloud radiative effect at top-of-the-atmosphere ranges from about 40 $\mathrm{Wm^{-2}}$ to 80 $\mathrm{Wm^{-2}}$, i.e., subtropical cloud reflectivity differs by about 100 % between the applied GCMs. ICON-AES exhibits particularly low subtropical cloud reflectivity compared to CAM and ICON-NWP. The latter two GCMs exhibit a similarly strong subtropical cloud reflectivity.

b) **Can differences in Cryogenian low-level mixed-phase cloud abundance between GCMs be explained by the large-scale atmospheric state and the synoptic conditions?**

No. The cloud controlling factors surface temperature, pressure velocity at 500 hPa, and lower tropospheric stability exhibit similar frequency distributions in the applied GCMs. Despite the similar frequency distributions, the GCMs exhibit substantially different low-level cloud cover. Our analysis shows that the synoptic conditions exhibit similar qualitative and quantitative characteristics in the applied GCMs. Low-level clouds similarly form in areas of large-scale subsidence located below the descending branch of the Hadley circulation and areas of large-scale ascent, associated with baroclinic waves. The frequency of the occurrence of subsiding and ascending motion is similar in the applied GCMs.

c) **How does explicitly resolving moist convection impact Cryogenian subtropical cloud reflectivity?**

In ICON large-eddy (ICON-LEM) simulations, in which the largest, convective-scale eddies within the atmospheric boundary layer are resolved, subtropical cloud reflectivity is substantially higher compared to ICON simulations in numerical weather prediction mode (ICON-NWP) that apply parameterizations for moist convection. In ICON-LEM simulations subtropical cloud reflectivity is about 100 % stronger compared to the ICON-NWP simulations.

d) **How do high concentrations of ice nucleating particles impact Cryogenian subtropical cloud reflectivity?**

In both ICON-LEM and ICON-NWP simulations, subtropical cloud reflectivity strongly decreases when we increase the abundance of mineral dust aerosol particles that potentially become activated to ice nucleating particles by a factor of 100. This corresponds to an increase from moderate to extreme concentrations of ice nucleating particles in present-day climate. Given the potentially much higher abundance of mineral dust aerosol during the Cryogenian compared to present-day conditions the extreme value in our view is plausible but uncertain. The corresponding decrease in subtropical cloud reflectivity is about 75 % in ICON-LEM and about 50 % in ICON-NWP. The decrease is associated with an enhanced Wegener-Bergeron-Findeisen process leading to the depletion of supercooled cloud liquid in mixed-phase clouds.

Summarising, the main key and novel findings of this thesis are:

I) We explicitly demonstrate and explain the impact of subtropical cloud reflectivity on the existence of a geologically relevant Jormungand-waterbelt state.

II) We show that the uncertainty associated with the crucial impact of subtropical cloud reflectivity limits our capabilities to assess the plausibility of the Jormungand hypothesis in idealized aquaplanet simulations.

A potential impact of clouds on the Jormungand-waterbelt scenario was already discussed by Abbot et al. (2011) when first formulating the Jormungand hypothesis. However, Abbot et al. (2011) expected weak subtropical cloudiness to be a prerequisite for the Jormungand mechanism to take effect. In this work we clarify the cloud impact, which contradicts the expectation formulated in Abbot et al. (2011). Our joint analysis of GCM simulations and the one-dimensional EBM demonstrates that highly reflective subtropical clouds are required to maintain a stable Jormungand-waterbelt climate. Clouds stabilize the Jormungand-waterbelt climate by masking the shortwave radiative signal of ice-edge movement at top-of-the-atmosphere and thus weaken the ice-albedo feedback. More reflective clouds lead to a stronger masking effect, which increases the weakening of the ice-albedo feedback, instead of reducing the weakening of the ice-albedo feedback as was suggested by Abbot et al. (2011).

We further show that the magnitude of Cryogenian subtropical cloud reflectivity simulated in GCMs is highly uncertain because it arises from low-level mixed-phase clouds that are hard to represent in GCMs (McCoy et al., 2016; Korolev et al., 2017). We explicitly demonstrate that the uncertainty associated with parameterizations of cloud microphysical processes in GCMs prohibits to assess whether the Cryogenian Earth may have experienced a hard Snowball Earth or a waterbelt climate. Specifically, we show that a loosely constrained tuning parameter that represents the efficiency of the Wegener-Bergeron-Findeisen process determines the existence of a geologically relevant waterbelt state.

We furthermore show that the uncertainty of subtropical cloud reflectivity persists in more sophisticated atmospheric models that omit this tuning parameter. Our hierarchy of ICON-NWP and ICON-LEM simulations provides evidence that highly reflective Cryogenian low-level mixed-phase clouds trapped below the descending branch of the Hadley circulation are dynamically feasible. However, we also demonstrate that subtropical cloud reflectivity is strongly reduced at high concentrations of mineral dust aerosols acting as ice nucleating particles. This links the existence of geologically relevant waterbelt states to the abundance of mineral dust ice nucleating particles. The knowledge concerning the abundance and composition of Cryogenian aerosol is strongly limited. Given the lack of observations for Cryogenian climate and the difficulties to model aerosol and its impacts on climate even in present-day climate, we consider overcoming these limitations in the foreseeable future as virtually impossible. Therefore, we conclude that assessing the plausibility of the Jormungand hypothesis in idealized aquaplanet setups with a purely thermodynamic ocean and sea ice is not possible even if dynamical processes were simulated accurately and discuss further consequences in section 7.2.

The major implication of this thesis is that the Jormungand-waterbelt scenario is an unreliable explanation for the Cryogenian glaciations. The requirement of extreme albedo values and the sensitivity of waterbelt states to uncertain cloud processes in idealized aquaplanet simulations strongly questions the idea that the Cryogenian pan-glaciations and their geology can be explained without the hard Snowball Earth hypothesis. Thus, we conclude that with the current state of knowledge the dynamically more stable Snowball state is a more reliable scenario and Cryogenian life has likely faced harsh evolutionary conditions of a globally ice-covered ocean.

Furthermore, the enhanced understanding of the cloud impact on the Jormungand mechanism allows to provide a consistent new interpretation of the GCM simulations conducted in previous studies, as discussed in chapter 5. Based on the EBM we estimate a space of the critical parameters, i.e., cloud reflectivity and bare sea-ice albedo, within which the existence of Jormungand-waterbelt states can be expected. This provides a new basis that we believe will help to explain why previous and future GCM-based studies do or do not exhibit Jormungand-waterbelt states.

Moreover, the implications of our results are not limited to Earth but also apply to the climate of extrasolar planets and their habitability. As discussed in chapter 5, our results indicate that abundant cloudiness narrows the range of habitable climates within the habitable zone, i.e., climate states with liquid water available at the surface. Furthermore, the cloud masking effect identified in this work likely impacts a planet's climate via CO_2 clouds near the outer edge of the habitable zone. These implications are particularly interesting in the context of upcoming observational studies based on the recently launched James Webb Space Telescope that will provide unprecedented insight into the atmospheres and clouds of extrasolar planets (Kaltenegger, 2017; Powell et al., 2019).

Finally, our work supports the idea that clouds contribute to keeping Earth's long-term climate conditions within habitable ranges as hypothesized by Rossow et al. (1982) and recently suggested by Goldblatt et al. (2021) in the context of the Faint Young Sun Problem. Regarding the Cryogenian glaciations, clouds may also have helped to maintain Earth's climate habitable, irrespective of the uncertainty associated with clouds in atmospheric models. Clouds either prevented the Earth's oceans from entirely freezing over as shown in this work or helped Earth to escape the Snowball climate (Abbot et al., 2012; Abbot, 2014). Hence, our results reinforce that clouds and particularly mixed-phase clouds are a crucial but uncertain feature of the Earth system (Boucher et al., 2013; McCoy et al., 2016; Zelinka et al., 2020) and will continue to challenge the understanding of our past and the projection of our future.

7.2. Outlook

We here present potential directions of future work to further pursue the overarching goal of assessing the viability of a Jormungand-waterbelt scenario as a potential explanation for the Cryogenian glaciations and transfer our results to the context of exoplanet atmospheres.

Our results indicate, that the explicit treatment of moist convection in high-resolution atmospheric models is beneficial to investigate Cryogenian clouds. At the same time, the current uncertainty associated with Cryogenian aerosol conditions prohibits to assess the plausibility of waterbelt scenarios. Advanced estimates of the Cryogenian aerosol conditions require comprehensive Earth system models. Tools that may provide the basis for a convergence of Earth system modeling and high-resolution simulations are convection-permitting regional climate models (Giorgi, 2019), which could incorporate interactive treatment of aerosol (Drugé et al., 2021). Such advanced model setups appear technically feasible in the near future. However, given the substantial uncertainties associated with aerosol and aerosol-cloud interactions even in present-day climate (Boucher et al., 2013), we doubt that satisfactory constraints on cloud reflectivity will emerge from this approach. Therefore, we suggest to first assess whether clouds are indeed an essential factor for Cryogenian climate if comparing the impact of clouds to that of other components of the Earth system in more comprehensive model setups than the idealized aquaplanet setup applied in this work. If this comparison confirms the essential role of clouds, we suggest to further deepen our understanding of Cryogenian clouds in a second step. As an independent step, we suggest to transfer the conclusions drawn from our results to extrasolar planetary climate applications. We describe our suggestions in more detail in the following.

Are clouds indeed an essential factor for Cryogenian climate?

In our opinion, the most important next step towards a more complete picture of a potential Cryogenian waterbelt scenario is to investigate how other components of the Earth system, such as continents, ocean heat transport, and sea-ice dynamics impact the viability of the Jormungand hypothesis. This will allow to compare the impact of highly reflective subtropical clouds to the impacts of other Earth system components and thus will reveal whether clouds are indeed an essential factor for Cryogenian climate. With this aim, we suggest to conduct a hierarchy of simulations, in which the complexity of Earth system models gradually increases from an idealized aquaplanet setup as applied in this work in chapter 5 towards a fully-coupled atmosphere-ocean GCM with sea-ice dynamics and realistic Cryogenian continents. A suitable tool that provides the capabilities to run a hierarchy of models across different levels of complexity is the ICON Earth System Model version 1.0, recently released by the Max-Planck-Institute for Meteorology (Jungclaus et al., 2021). In the following, we specifically discuss potential implications of incorporating continents and ocean heat transport in GCMs.

We consider the impact of continents to be closely linked to the stabilizing cloud-based mechanism proposed in this work. Continents may impact the Jormungand hypothesis via two pathways. The first pathway is the direct impact of continents on surface albedo. Low-latitude continents - as they are expected to have prevailed during the Cryogenian - increase the low-latitude planetary albedo compared to an aquaplanet setup. According to the mechanism suggested in this work, the low-latitude albedo increase due to continents would act to stabilize a waterbelt climate similar to highly reflective low-latitude clouds. This effect may be amplified by snow fall on continents that can be expected to further increase low-latitude albedo. However, the latter effect may strongly be dependent on the onset of low-latitude snow deposition. In this context, orography may have an important impact (Rodehacke et al., 2013; Walsh et al., 2019). The second pathway consists of the impact of continents on atmosphere dynamics. Continents can trigger stationary waves, which may induce changes in the Hadley cell dynamics (Schneider, 2006), and amplify the seasonal cycle of the Hadley cell. This may impact the precipitation-evaporation pattern and thus the sea-ice albedo as well as clouds, which constitute the essential elements of the Jormungand hypothesis.

Studying the impact of ocean heat transport on waterbelt states will allow one to assess two ideas. First, one can test whether the Jormungand mechanism is indeed more important than ocean heat transport regarding the ice-edge latitude of the bifurcation point between waterbelt and Snowball climate as discussed based on the results of Voigt and Abbot (2012) in section 5.4. Second, one can test whether the Jormungand mechanism and ocean heat transport act jointly to create a waterbelt state spanning a wide range of ice-edge latitudes as hypothesized by Rose (2015). To isolate the impact of ocean heat transport we suggest to start investigating the impact of ocean heat transport in the absence of continents and sea-ice dynamics and with parameterizing ocean heat transport in a mixed-layer ocean model. Parameterizations of ocean heat transport could, e.g., be based on the linear diffusion parameterization applied in Pollard et al. (2017) or the Ekman heat transport parameterization by Codron (2012). Parameterizing ocean heat transport in a mixed-layer ocean model instead of applying a fully dynamic ocean provides a first order estimate of the impact of ocean heat transport at much lower computational cost than a fully dynamic ocean model and avoids potential instabilities in the ocean dynamics ocurring in the absence of continents.

The model hierarchy could be complemented by the simulation results from Voigt and Abbot (2012), Shields et al. (2013), Rose (2015), and Pollard et al. (2017) if available. Quantifying subtropical cloud reflectivity in these simulations might also provide qualitative insight into the stabilizing and destabilizing factors for the Jormungand-waterbelt state. Moreover, analyzing these simulations with regard to subtropical cloud reflectivity may grow further confidence in the robustness of the here suggested stabilizing role of clouds on the Jormungand-waterbelt state

Deepening our understanding of Cryogenian clouds

If the more comprehensive modeling approaches of Cryogenian climate described above confirm that clouds are an essential factor for Cryogenian climate our understanding of Cryogenian clouds can be advanced as suggested in the following.

Our analysis of subtropical clouds is focused on their shortwave radiative signal at top-of-the-atmosphere (TOA). As reviewed in section 2.3, Poulsen et al. (2001) and Poulsen and Jacob (2004) suggested a mechanism how clouds may stabilize the ice edge via longwave surface warming. Our ICON-NWP and ICON-LEM simulations conducted as part of the model hierarchy across horizontal resolutions provide suitable model output to also investigate the surface warming effect of clouds. Analyzing our simulations with a focus on longwave radiation may provide a comparison of the magnitudes of the shortwave-TOA and the longwave-surface effects. This would allow to assess, which effect to focus on in future studies.

Any future attempt to quantify the magnitude of Cryogenian cloud-radiative effect will rely on the hypothesized aerosol scenario. Consistent Cryogenian aerosol scenarios may be developed on the basis of realistically configured GCMs applying a comprehensive interactive treatment of aerosol as, e.g., done by Liu et al. (2020) for mineral dust aerosol. Still, these scenarios will strongly rely on the specific boundary conditions and parameterizations and thus remain purely hypothetical. Given the high sensitivity of clouds to the assumed aerosol scenario (as discussed in chapter 6), we expect that studies of Cryogenian clouds will foster our understanding of cloud-related processes but will not be able to provide stringent constraints on Cryogenian cloud forcing.

Studies following this line of research should address the impact of cloud condensation nuclei on Cryogenian clouds located over a low-latitude ice edge, as this effect was not considered in this work. Furthermore, the ICON-NWP and ICON-LEM simulations conducted as part of this work apply horizontal grid spacings of kilometers and hectometers and are located in the gray zone of convection. Thus, comparing the results of this thesis to simulations that allow to fully resolve the dynamics of shallow mixed-phase clouds might further grow confidence in our results. Such simulations could be provided by applying a large-eddy model, e.g., ICON-LEM with grid spacings on the order of decameters (Stevens et al., 2002). Further growing confidence in our results might also be achieved by extending simulations at relatively small grid spacings, e.g. at the kilometer scale, to larger spatial and temporal domains. Such simulations are already conducted at the global scale (see e.g. Hohenegger et al. (2020)). The option for nested high-resolution grids in ICON provides a suitable tool for simulating a waterbelt climate, for which the zone of interest is confined to a narrow belt around the equator. Finally, future studies can be expected to benefit from growing computational resources and advances in model development. For example, biases in cloud reflectivity arising from low-level mixed-phase clouds in present-day climate could recently be reduced through the development of a one-moment microphysical scheme, which is suitable for the application in global cloud-system-resolving models (Noda et al., 2021).

Knowledge-transfer to extrasolar planetary climate

As discussed in section 5.4, the stabilizing impact of highly reflective clouds on Jormungand-waterbelt states implies that the cloud response to transitions between climate states may be crucial for the habitability of extrasolar planets. The parameterizations applied in the GCMs used in this work were developed for Earth's present-day climate conditions, which likely impacts the cloud response if transitioning to the much colder waterbelt climate. This impact can be reduced by applying GCMs with small grid spacings that resolve smaller length-scales of the atmospheric circulation and thus reduce the importance of the applied parameterizations or by applying more flexible parameterizations. The latter approach is pursued in the ongoing development of the GCM ROCKE-3D, which is a branch-off from the CMIP6 model GISS ModelE2 (Way et al., 2017). ROCKE-3D is designed to be adjusted to a wide range of climatic conditions and thus can represent the conditions expected on extrasolar planets as well as on Cryogenian Earth. The convection scheme applied in ROCKE-3D avoids the reliance on a specific humidity profile and moist adiabatic lapse rate that may determine convection in less flexible convection schemes (Way et al., 2017). Thus, we consider ROCKE-3D to be a suitable tool for studying the cloud response to a transition from a temperate to a waterbelt climate under various planetary conditions in a qualitative manner. Future versions of ROCKE-3D will include a two-moment cloud microphysical scheme and an improved representation of entrainment. This will increase the flexibility of ROCKE-3D in simulating the cloud response to climatic transitions and allow one to, e.g., link the cloud response to specific aerosol scenarios. Moreover, future versions of ROCKE-3D will include parameterizations for atmospheric condensation of CO_2, which is an essential element for modeling atmospheric processes at the outer limit of the habitable zone (OHZ) (Way et al., 2017). As discussed in section 5.4, the masking effect of H_2O clouds identified in this work may similarly arise from CO_2 clouds on planets near the OHZ. The future version of ROCKE-3D will provide the capabilities to assess how the masking effect of clouds plays out in a dynamic and interactive three-dimensional atmosphere on a planet near the OHZ and how this affects the planet's habitability.

A. Appendix for chapter 5

This chapter is based on Braun et al. (2022a).

©The Authors.

We here note that our results presented in this chapter are solely based on CAM and ICON-AES. We therefore refer here to the latter as ICON, similarly as in chapter 5.

A.1. Overview of conducted simulations

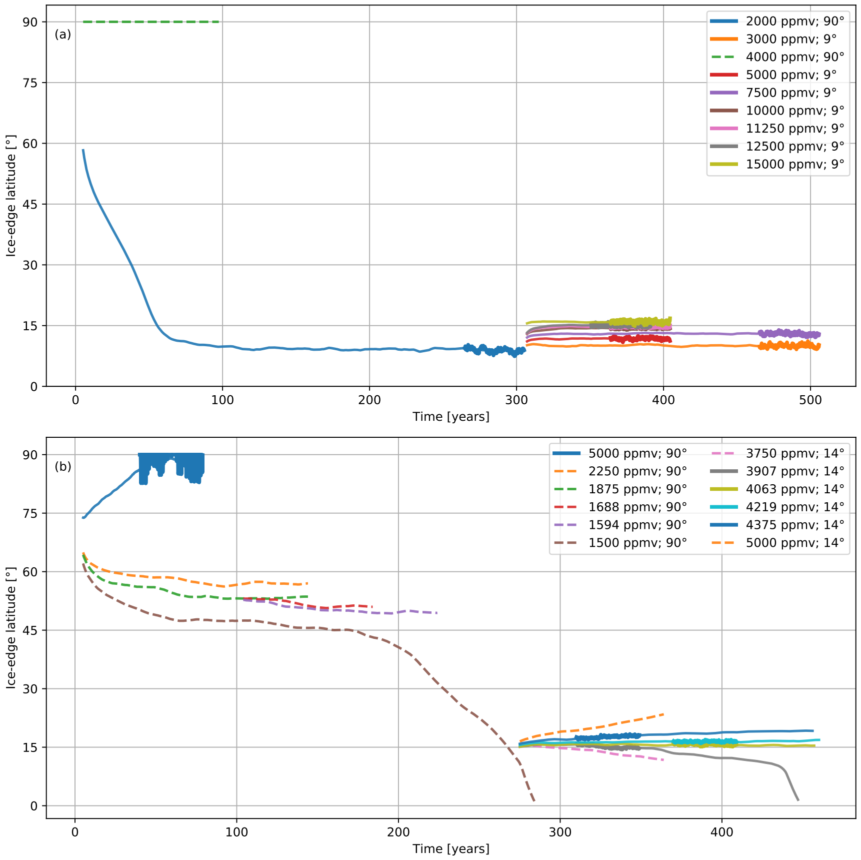

Figure A.1.: Temporal evolution of the global-mean ice edge latitude in the default setups of CAM (a) and ICON (b). Global-mean ice edge latitude is calculated as the sine of global-mean ice-free surface fraction. Labels indicate the constant atmospheric CO_2 concentration and the global-mean ice-edge latitude of the initialisation. Thin lines represent the 10-year rolling mean. Solid lines indicate simulations considered to exhibit (semi-)stable waterbelt states. Thick solid lines represent monthly-mean for 40-year periods that are analyzed as (semi-)stable waterbelt states.

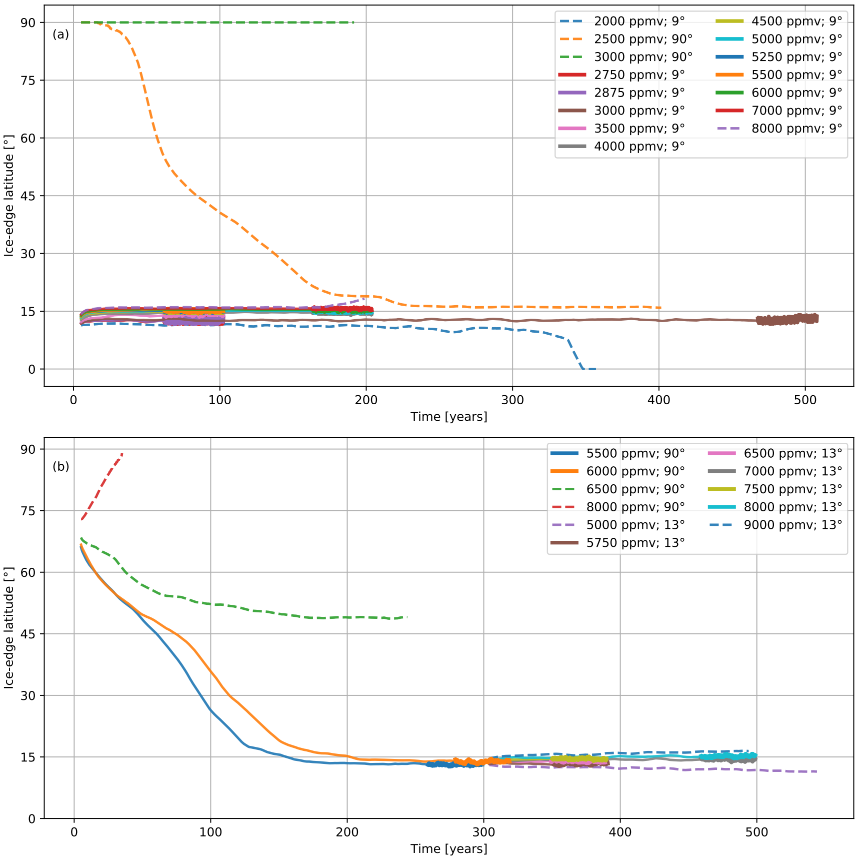

Figure A.2.: Temporal evolution of global-mean ice edge latitude for modified GCM simulations. (a) CAM pCOOKIE. (b) ICON WBF. See caption of A.1 for further details.

A.2. Jormungand mechanism in CAM and ICON: clear-sky planetary albedo over snow-covered sea ice, bare sea ice, and ice-free ocean

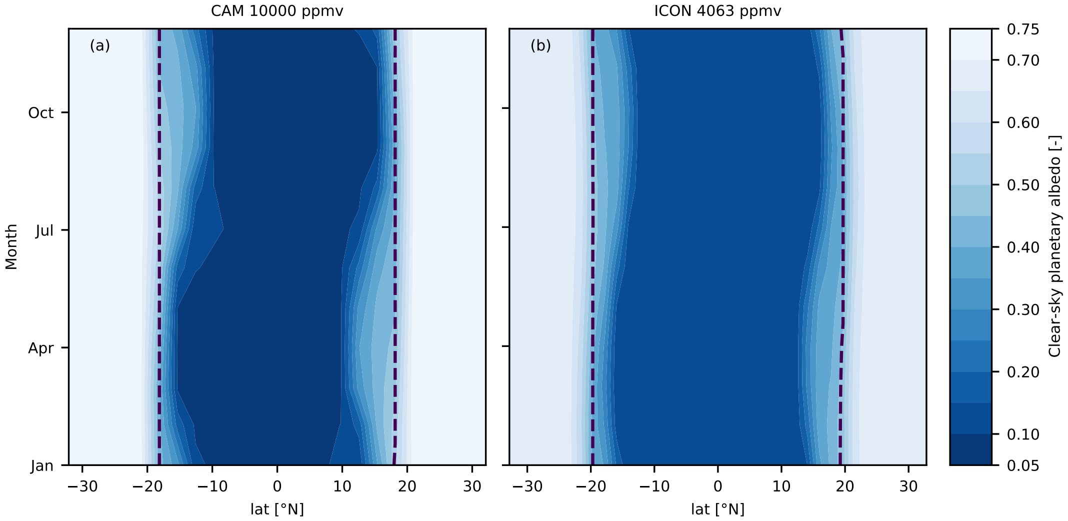

Figure A.3.: Low clear-sky planetary albedo due to exposure of bare sea ice in the subtropical region in CAM and ICON. Climatological zonal-mean clear-sky planetary albedo determined from (a) CAM simulation at 10000 ppmv CO_2 and (b) ICON simulation at 4063 ppmv CO_2. Dashed contours indicate the water-equivalent snow thickness of 0.01 m, which marks the minimum thickness of a snow-layer to be considered in the determination of the surface albedo in ICON. For each simulation 40-year periods are analyzed. Further details are given in text S1.

Due to the negative surface mass balance (precipitation-evaporation) in the subtropics, ICON and CAM show a sharp decrease of clear-sky planetary albedo around 20° latitude (Fig. A.3). This is the latitude where in ICON the water equivalent snow thickness is close to 0.01 m, which marks the critical thickness for determining surface albedo. Below a water equivalent snow thickness of 0.01 m surface albedo is considered to be the albedo of bare sea ice. In CAM, however, water equivalent snow thickness at the albedo transition latitude is higher. This may be caused by the different parameterizations of snow-ice albedo in CAM and ICON: CAM does not exhibit a sharp transition between the albedos of bare and snow-covered sea ice at a given water equivalent snow thickness. At low water equivalent snow thicknesses CAM yields lower surface albedos than ICON at the same equivalent snow thickness. In general the clear-sky planetary albedo over ice is higher in CAM compared to ICON, while the planetary albedo over ice-free ocean in CAM is lower. A likely explanation is that albedos prescribed in ICON are broadband average albedos derived from CAM using the assumption that 40% of solar insolation reaching the surface is in the visible spectrum and the rest is in the infrared spectrum. The impact of the overall lower clear-sky ice albedo and higher clear-sky ocean albedo in ICON compared to CAM is expected to have a low impact on the stability of the waterbelt state. If having an impact, this would favor a stable waterbelt state in ICON because of a weaker ice-albedo feedback due to the lower difference between clear-sky planetary albedo over ice-covered and ice-free ocean. Furthermore, by using these broadband average albedo parameters derived from CAM the waterbelt state has been found in ECHAM5 (Abbot et al., 2011).

A.3. Seasonal comparison of the large-scale atmospheric states in CAM and ICON

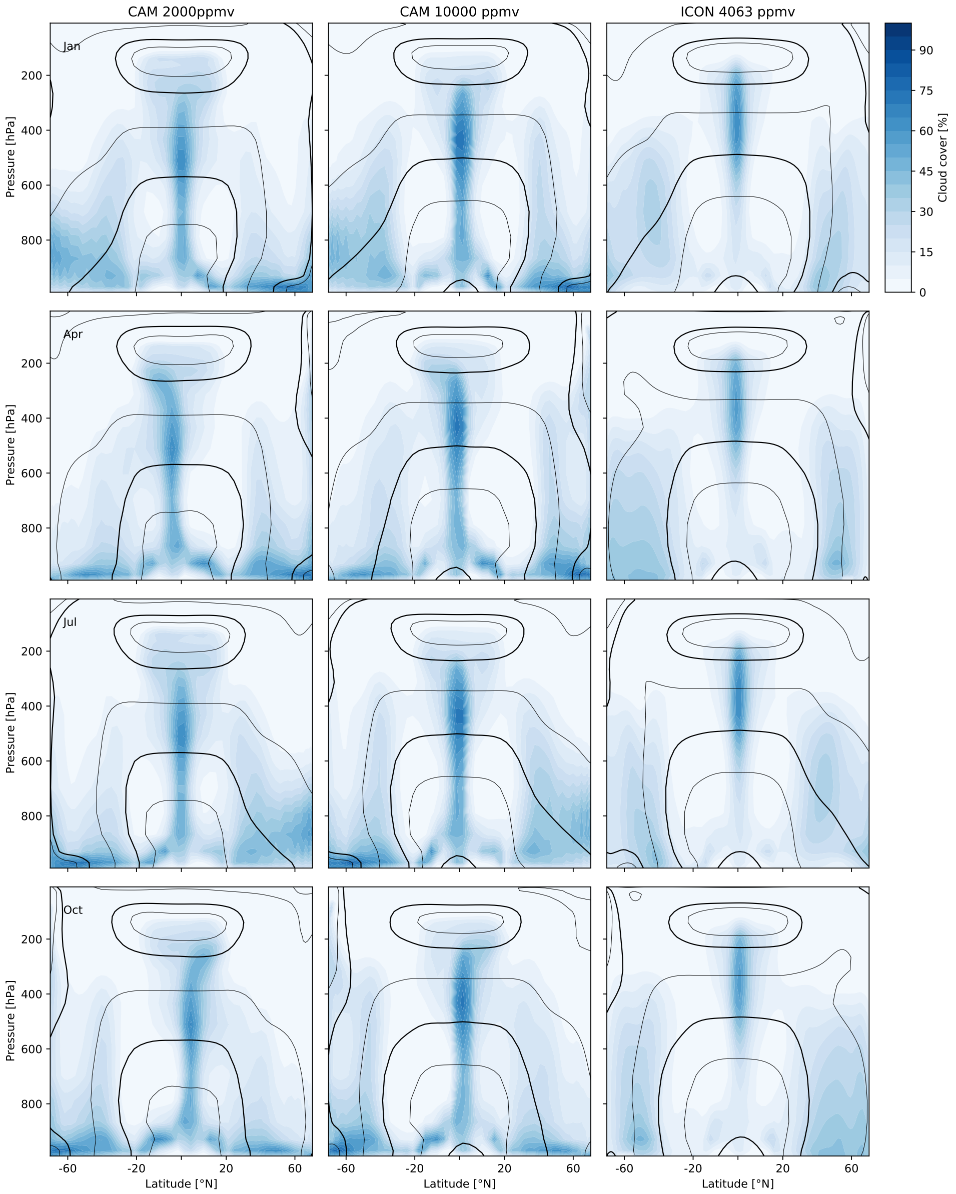

Figure A.4.: CAM and ICON exhibit similar large-scale thermal structure across the seasonal cycle and the simulated CO_2-range. Monthly climatological zonal-mean cloud cover and air temperature indicated by isotherms determined from CAM at 2000 ppmv CO_2 and 10000 ppmv CO_2, and ICON at 4063 ppmv CO_2. Each period of analysis spans 40 years after stabilizing in a stable waterbelt state.

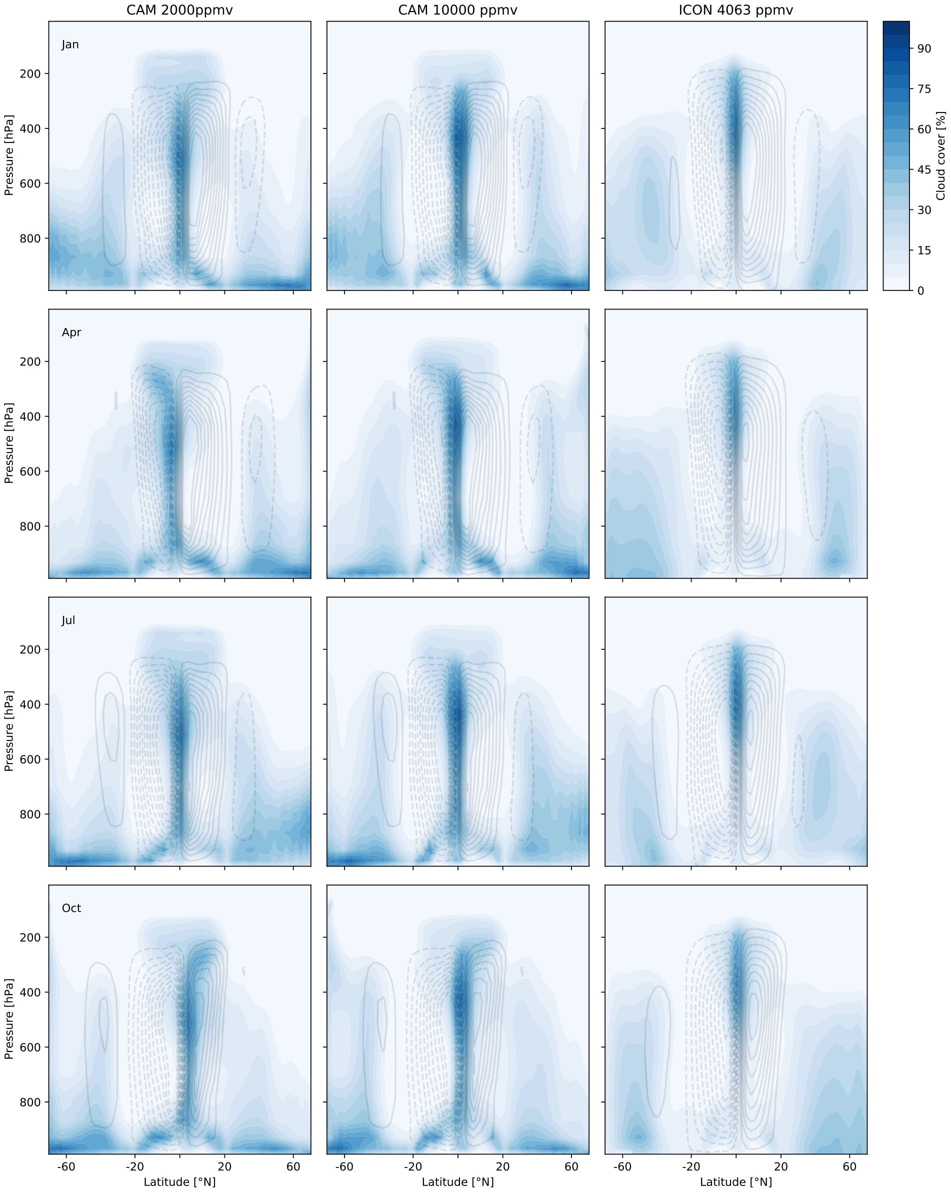

Figure A.5.: CAM and ICON exhibit similar large-scale circulation in CAM and ICON across the seasonal cycle and the simulated CO_2-range. Monthly climatological zonal-mean cloud cover and mass stream function indicated by contours. Contour intervals are $5 \cdot 10^{10}$ kgs^{-1}. Positive contours are solid and negative contours are dashed. The zero contour is not shown. The mass stream function is calculated by $\psi(p,\phi) = 2\Pi r_E cos(\phi)/g \int_p^{p_s} v dp$ with pressure p, surface pressure p_s, latitude ϕ, radius of Earth $r_E = 6371$ km, gravitational constant $g = 9.81$ ms^{-2}, and zonal-mean meridional wind v. Same simulations and time periods as in A.4 are used.

A.4. CAM partial COOKIE (pCOOKIE) simulations

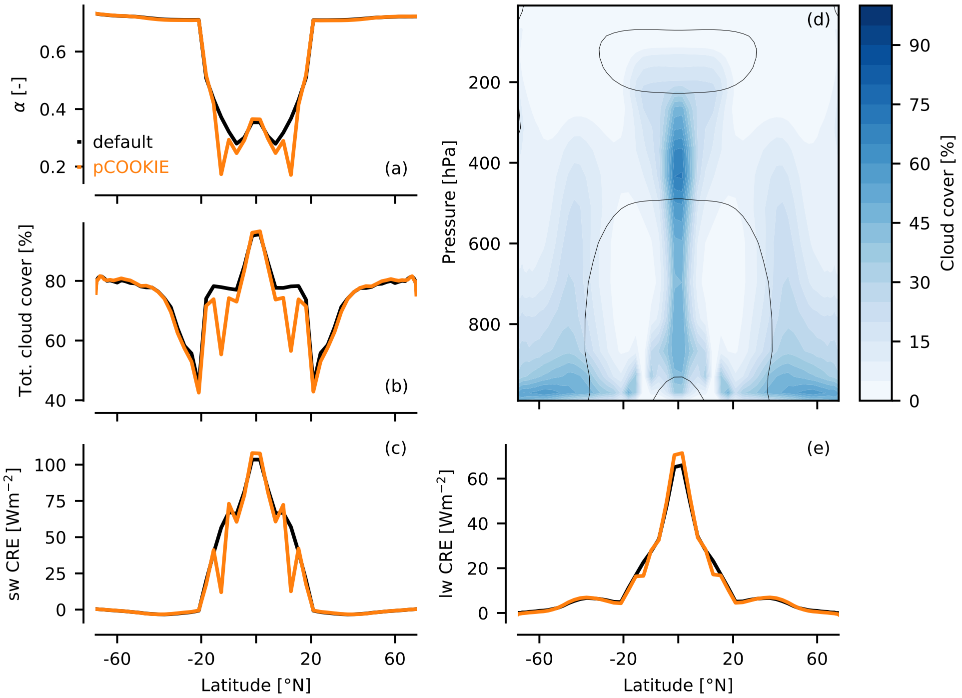

Figure A.6.: Impact of pCOOKIE modification in CAM on clouds and cloud-radiative effects. (a) Planetary albedo α, (b) total cloud cover, (c) shortwave CRE, and (e) longwave CRE for CAM standard and pCOOKIE. Shown are 40-year-means over all simulations after stabilizing in a stable waterbelt state. (d) 40-year-mean of zonal-mean cloud cover from a single simulation with CAM pCOOKIE after stabilizing in a waterbelt state at 5000 ppmv CO_2 along with 273 K, 235 K, and 192 K isotherms.

A.5. ICON simulations with modified Wegener-Bergeron-Findeisen process

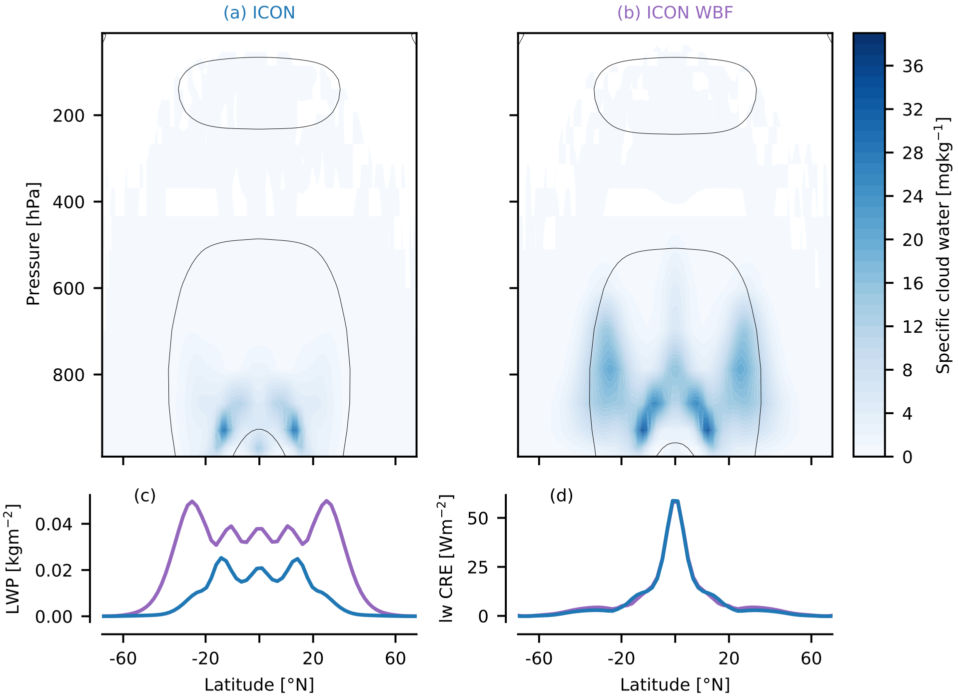

Figure A.7.: Impact of WBF modification in ICON on cloud liquid and longwave cloud-radiative effect. (a) and (b): Annual-mean zonal-mean specific cloud liquid from single simulations after stabilizing in a waterbelt state at 4063 ppmv CO_2 (ICON) and 6000 ppmv CO_2 (ICON WBF) along with 273 K, 235 K, and 192 K isotherms. (c) Annual-mean zonal-mean liquid water path LWP, and (d) longwave CRE averaged over all simulations with a (semi-)stable waterbelt state. The period of analysis spans 40 years after stabilizing in a (semi-)stable waterbelt state.

A.6. Estimation of parameters for the one-dimensional energy balance model from the GCM simulations

We here estimate the EBM parameters B, α_o, and C corresponding to our GCM simulations with CAM, ICON, CAM pCOOKIE, and ICON WBF (only B). All other EBM parameters are chosen as in Abbot et al. (2011).

Longwave feedback parameters

We derive estimates for the longwave feedback B for each GCM configuration by a linear regression of monthly-mean $\overline{L}$ on monthly-mean $\overline{T}$ using a least square fit. We estimate B for the temperature range spanned by all simulations indicated in Extended Data Figures 1 and 5. We exclude simulations spanning a small $\overline{T}$-range, i.e., with a standard deviation smaller than 1 K, to avoid miscorrelations. We assume the range spanned by the 95% confidence intervals of all regressions for one GCM configuration to be the 95% confidence interval of the GCM configuration. $r^2 > 0.72$ and $p < 1e^{-3}$ for each single simulation. Sample sizes are larger than 1200 for all regressions. We assume the fits to be centered within the 95% confidence interval. We find $B = 1.5 \pm 0.1$ $Wm^{-2}K^{-1}$ for CAM, $B = 1.45 \pm 0.2$ $Wm^{-2}K^{-1}$ for ICON, and $B = 1.54 \pm 0.16$ $Wm^{-2}K^{-1}$ for CAM pCOOKIE. Based on these estimates we use a value of $B = 1.5$ $Wm^{-2}K^{-1}$ for the CAM, ICON, and CAM pCOOKIE cases calculated with the EBM.

We additionally estimate the longwave feedback parameter B_w for the waterbelt surface temperature range. B_w is estimated similarly as B, but only taking into account data points within the range of global-mean surface temperatures, for which we find stable waterbelt states, i.e., -45 °C to -30 °C. The results are shown in Tab. A.1. For ICON WBF B_w is considerably larger than B. This reflects a considerable nonlinearity of $\overline{L}(\overline{T})$ for ICON WBF. Therefore, the EBM cannot be expected to explain the behaviour found in ICON WBF simulations, since the EBM assumes $\overline{L}$ to be a linear function of $\overline{T}$.

	B	B_w	B_w/B
CAM	1.5 ± 0.1	1.52 ± 0.09	1.01 ± 0.01
ICON	1.45 ± 0.2	1.52 ± 0.06	1.06 ± 0.11
CAM tropics	1.54 ± 0.16	1.64 ± 0.07	1.07 ± 0.07
ICON WBF	1.34 ± 0.15	1.49 ± 0.02	1.12 ± 0.11

Table A.1.: Estimated longwave feedback parameter B in units of $Wm^{-2}K^{-1}$ using the temperature range spanned by all conducted simulations (column 1) and longwave feedback parameter B_w using the temperature range spanned by simulated stable waterbelt states (column 2). Ratios B_w/B are used as an indicator of the (non-)linearity of the longwave feedback (column 3). See methods for further details.

Planetary albedo parameters

We estimate α_o for each GCM configuration from the 40-year time series of zonal-mean α that we obtain from simulations of (transient) waterbelt states (Fig. 5.1 d). A grid cell is considered ice free if sea-ice cover is lower than 50%. We calculate α_o for each simulation from the area-weighted mean over ice-free ocean.

α_o for each GCM configuration is calculated as the mean over all simulations. This yields $\alpha_o = 0.32$ for CAM, 0.24 for ICON, and 0.28 for CAM pCOOKIE.

Meridional heat transport parameters

We use $C/B = 1.5$ as proposed by Abbot et al. (2011), for the EBM parameters corresponding to the CAM standard configuration and estimate C/B for the other GCM configurations relative to CAM. The strength of meridional heat transport determines the equator to pole temperature contrast (Donohoe and Battisti, 2012), which we approximate by the equator to pole temperature difference ΔT^*.

First, we determine $\Delta T^*_{conf,GCM}$ for each GCM configuration from the 40-year annual-mean zonal-mean normalized surface temperature averaged over all (transient) waterbelt states shown in Fig. 5.1. We normalize the temperature profiles by global-mean temperature to remove differences in the mean climate state. Second, we similarly determine $\Delta T^*_{CAM,EBM}$ by applying the EBM with CAM parameters. The latitudinal temperature profile $T(\phi)$ in the EBM can be obtained as follows. For given A and ice edge latitude ϕ_s, $\overline{T}$ can be calculated from Eq. 6 in Abbot et al. (2011). Inserting $\overline{T}$ in Eq. 1 in Abbot et al. (2011), yields $T(\phi)$. Finally, we adjust C for each GCM configuration using the above EBM parameters, so that

$$\frac{\Delta T^*_{conf,EBM}}{\Delta T^*_{CAM,EBM}} \overset{!}{=} \frac{\Delta T^*_{conf,GCM}}{\Delta T^*_{CAM,GCM}}. \tag{A.1}$$

We estimate $C/B = 1.8$ for ICON and $C/B = 1.6$ CAM pCOOKIE. For given B, C increases with decreasing α_o because stronger meridional heat transport is required for lower α_o to maintain a similar equator to pole temperature difference.

A.7. Climate sensitivity parameter for energy balance model

The climate sensitivity parameter λ indicates how much global-mean surface temperature $\overline{T}$ changes with a variation of the global-mean radiative forcing $\overline{F}$.

Stable equilibrium states exhibit positive finite λ with lower values indicating lower sensitivity of the climate in terms of $\overline{T}$ to changes in $\overline{F}$. Unstable equilibrium states exhibit negative λ. If approaching a bifurcation point (black solid line in Fig. 3 (b)) from a stable equilibrium state λ approaches infinity.

λ can be formulated so as to account for multiple feedback mechanisms, with each feedback having its own sensitivity parameter f_i.

$$\lambda = \frac{d\overline{T}}{d\overline{F}} = \frac{\partial \overline{T}}{\partial \overline{F}} + \frac{d\overline{T}}{d\overline{F}} \sum_i f_i \tag{A.2}$$

In the EBM (Eq. 2.1) the ice-albedo feedback is the only feedback besides the Planck feedback. The sensitivity parameter corresponding to the ice-albedo feedback is

$$f_\alpha = \frac{\partial \overline{T}}{\partial \overline{\alpha}} \frac{d\overline{\alpha}}{d\overline{T}}. \tag{A.3}$$

Using the global-mean of Eq. 2.1, f_α is given by

$$f_\alpha = -\frac{\overline{I}}{B} \frac{d\overline{\alpha}}{d\overline{T}}. \tag{A.4}$$

After rearrangement, we find

$$\lambda = \frac{1}{B} \frac{1}{1 - f_\alpha}. \tag{A.5}$$

A.8. Relation of meridional heat transport and planetary albedo over ice-free ocean

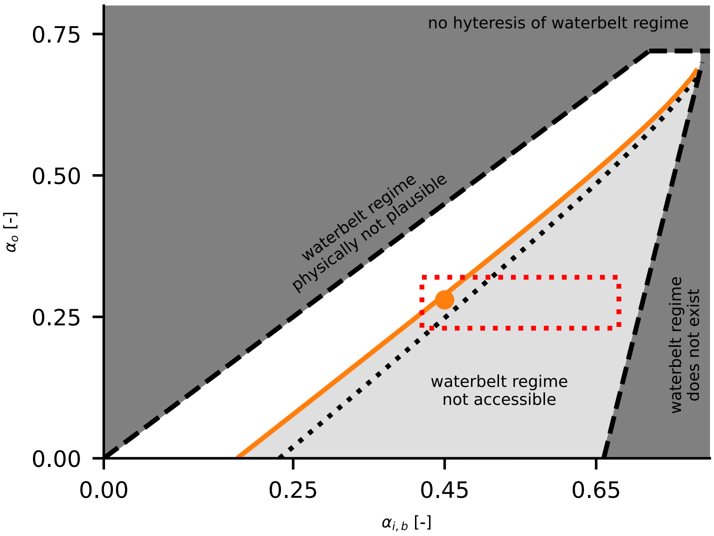

Figure A.8.: The geologically relevant domain of waterbelt states is impacted by the intensity of meridional heat transport. Domains spanned by planetary albedo over ice-free ocean α_o and bare sea ice albedo $\alpha_{i,b}$ for stable and accessible waterbelt states (white) and stable but unaccessible waterbelt states (light gray). The orange circle marks albedo values for CAM pCOOKIE. The orange line marks the lower boundary of the stable and accessible domain and is calculated with the meridional heat transport parameter $C = 1.6B$ corresponding to CAM pCOOKIE. The black dotted line marks the lower boundary of the stable and accessible domain if calculated with $C = 1.5B$ corresponding to CAM (similar as in Fig. 3c). Weaker meridional heat transport stabilizes the waterbelt climate because it is characterized by strong meridional temperature gradients. The red dotted box indicates the range of plausible values for α_o and $\alpha_{i,b}$.

B. Appendix for chapter 6

This chapter is based on Braun et al. (2022b).

B.1. Selection of representative periods and subdomains

We choose representative periods and subdomains to relate the short periods and subdomains of ICON-NWP and ICON-LEM simulations with the long-term climatic state. We first describe the selection of the representative periods and subdomains in sections B.1.1, B.1.2, and B.1.3 and provide an overview of the subdomains in section B.1.4.

B.1.1. Selection of a representative 5-day period for NWP10

The annual cycle of global-mean low-level cloud cover in NWP160 peaks at solstice (not shown). Furthermore, our simulation setup is symmetric across the equator.

Therefore, we choose a 5-day period for the subdomain spanning 2.5° to 22.5° latitude South during June. We focus on the winter hemisphere, because the ice-edge is here closer to the equator than during summer.

We analyze 5-day periods starting on each day between June, 1st and June, 25th of 5 consecutive years from NWP160. This yields 125 periods. For each period we calculate the time-mean domain-mean of total, low-, mid-, and high-level cloud cover, column cloud ice and liquid, column water vapor, surface temperature, and SWCRE. We select a representative period, for which the time-mean domain-mean values are located within the inner quartiles of the distribution of the 125 periods (Fig. B.1).

B.1.2. Selection of the representative LAM-subdomain for NWP2.5

Analogously to choosing the 5-day period for NWP10, we choose a representative subdomain for the simulation NWP2.5 by analyzing 68 potential subdomains from NWP10. Each subdomain reaches from 2.5° to 22.5° latitude South and spans 25° in longitudinal direction. The subdomains overlap by 5° longitude. Subdomains crossing 360° longitude are not considered. We choose a subdomain that is located at 100° to 125° longitude (Fig. B.2).

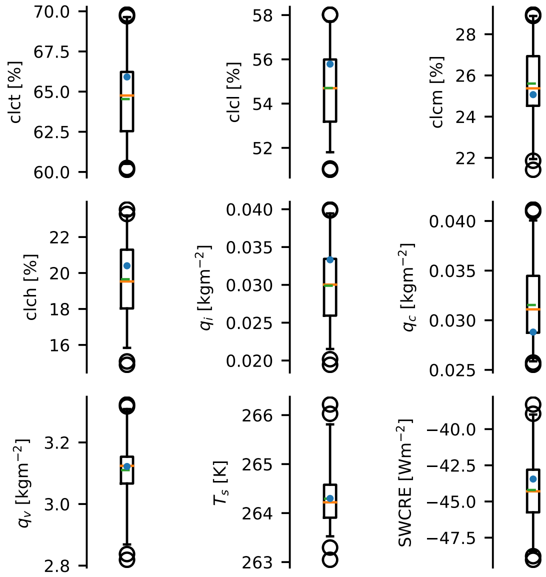

Figure B.1.: Distribution of domain-mean time-mean values of 125 5-day periods determined from simulation NWP160. The chosen representative period is marked by the blue dot. This period starts at June, 11 in year 5 of the simulation NWP160. The considered variables are: total cloud cover clct, low-, mid-, and high-level cloud cover (clcl, clcm, clch), column cloud ice q_i and liquid q_c, column water vapor q_v, surface temperature T_s, and shortwave cloud-radiative effect SWCRE. The box extends from the lower to upper quartile, and th orange line depicts the median. The green dashed line indicates the mean. The whiskers indicate the 1 and 99 percentiles. Circles indicate flier points beyond the whiskers.

B.1.3. Selection of a 1-day period and the LEM-6°-subdomain for LEM0.6

We choose a suitable subdomain and period for LEM0.6 by analyzing 80 spatial and temporal subsets of NWP2.5. We analyze 1-day periods starting each day, which yields 4 periods. For each period we analyze subdomains that span 6° longitude within the range 100° to 125° longitude and overlap by 5° longitude. This yields 20 subdomains per period. The subdomains extend from 11° to 17° latitude.

Analogously to section B.1.1 we calculate time and area means for each subset. Since we study shallow low-level clouds, we exclude subsets that exhibit mid- and high-level cloud cover exceeding 10 %. By further selecting subsets, for which surface temperature and column water vapor lie within the inner quartiles of the distributions, leaves us with two subsets. We choose the subset with stronger low-level cloud cover and stronger SWCRE (Fig. B.3).

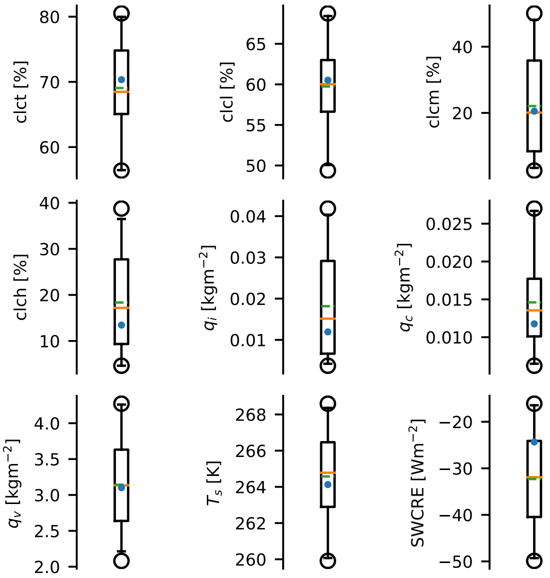

Figure B.2.: Distribution of domain-mean time-mean values over 68 subdomains determined from simulation NWP10 for a 4.5-day period. The chosen representative period is marked by the blue dot. For further description see Fig. B.1.

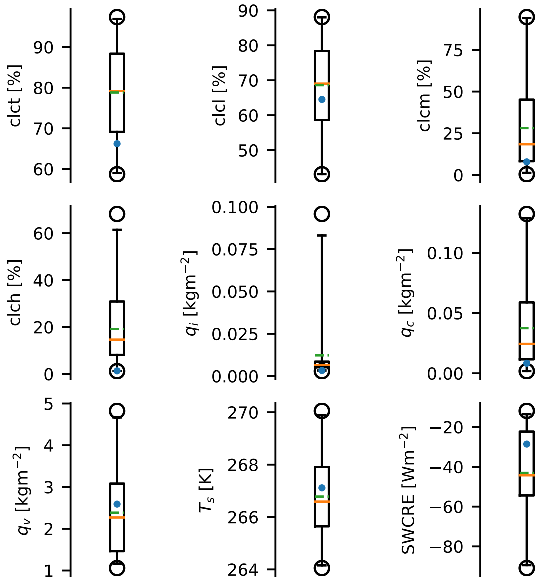

Figure B.3.: Distribution of domain-mean time-mean of 80 ensemble members determined from simulation NWP2.5 for 1-day periods. The chosen period is marked by the blue dot. For further description see Fig. B.1.

B.1.4. Overview of subdomains

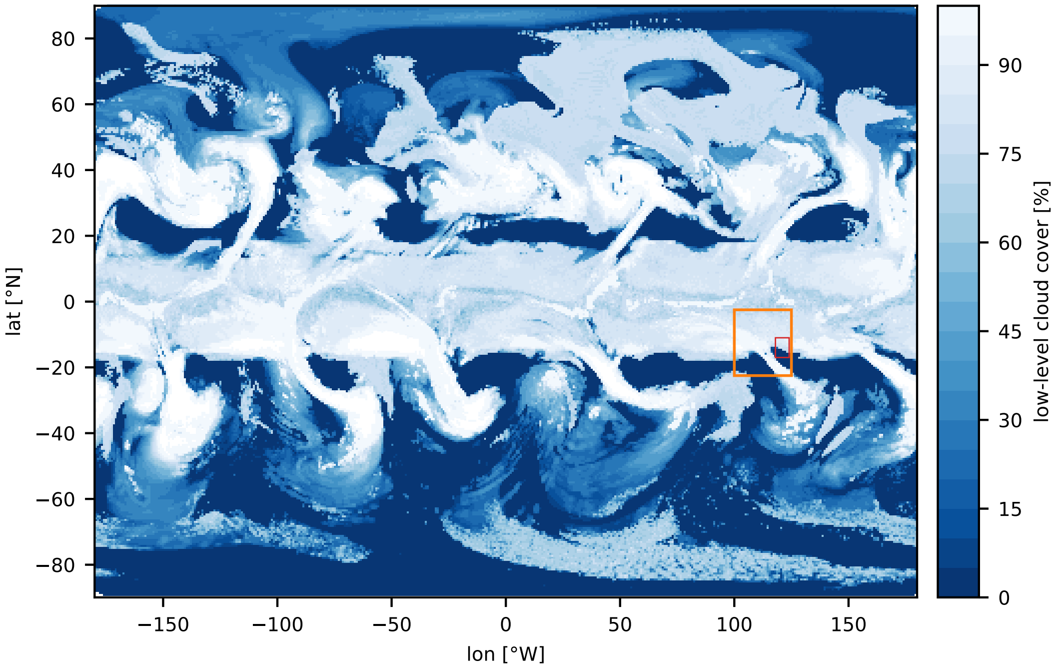

Figure B.4.: Snapshot of low-level cloud cover from the global ICON-NWP simulation at $\Delta_h = 10$ km. The orange rectangle indicates the LAM-subdomain. The red rectangle indicates the LEM-6°-subdomain.

B.2. Significance of differences in time-mean domain-mean SWCRE

To test whether the differences in time-mean domain-mean SWCRE are significant, we provide an estimate for internal variability in section B.2.1 and test the statistical significance of SWCRE differences in section B.2.2.

B.2.1. Estimation of internal variability of time-mean domain-mean SWCRE in NWP160

Since NWP160 and NWP10 are both global simulations that can diverge after the initialisation, we show that the difference in SWCRE between NWP160 and NWP10 is larger than the internal variability of NWP160. We do so by providing an estimate for the internal variability of SWCRE in NWP160. To quantify the internal variability, we analyze 125 5-day periods from the 5 years of NWP160 using the month of June of each year. Each period is characterized by the time and area mean SWCRE over the subtropical region (-30° to 30° latitude). Consecutive 5-day periods of the same year overlap by 4 days. This leads to 25 periods per year. The corresponding distribution of the periods in terms of SWCRE is given by the gray shading and whiskers in Fig. 6.5a and indicates that the difference in SWCRE between NWP160 and NWP10 is significantly larger than the internal variability of NWP160.

B.2.2. Statistical significance of differences in time-mean domain-mean SWCRE

We check whether the differences in time-mean domain-mean SWCRE shown in each panel of Fig. 6.5 are statistically significant. We do so by creating frequency distributions of the time-mean SWCRE corresponding to the SWCRE shown in Fig. 6.5. Spatially the SWCRE corresponding to each simulation is analyzed on the horizontal grids used for the respective simulation. The resulting distribution indicates the spatial variability of the time-mean SWCRE. We compare all frequency distributions in each panel pairwise by performing two-sided t-tests with non-equal variance for the two frequency distributions (Welch, 1947).

We find 3 differences in SWCRE, for which the p-value of the Welch's test exceeds 1 %. This indicates that these difference are not statistically significant. In fact, the corresponding differences of the time-mean domain-mean SWCRE are small as shown in Fig. 6.5b. The differences are:

1. 160 km vs 2.5 km, if using 4.5 days
2. 160 km vs 10 km, if using 1.5 days
3. 160 km vs 2.5 km, if using 1.5 days

For all other SWCRE differences the p-value is far below 1 %. Hence, we consider all other SWCRE differences shown in Fig. 6.5 as statistically significant.

C. List of Figures

D. List of Tables

E. Bibliography

Abbot, D. S., 2014: Resolved Snowball Earth Clouds. *Journal of Climate*, **27 (12)**, 4391–4402.

Abbot, D. S., I. Eisenman, and R. T. Pierrehumbert, 2010: The Importance of Ice Vertical Resolution for Snowball Climate and Deglaciation. *Journal of Climate*, **23 (22)**, 6100–6109.

Abbot, D. S. and I. Halevy, 2010: Dust aerosol important for Snowball Earth deglaciation. *Journal of Climate*, **23 (15)**, 4121–4132.

Abbot, D. S. and R. T. Pierrehumbert, 2010: Mudball: Surface dust and Snowball Earth deglaciation. *Journal of Geophysical Research: Atmospheres*, **115 (D3)**.

Abbot, D. S., A. Voigt, M. Branson, R. T. Pierrehumbert, D. Pollard, G. Le Hir, and D. D. B. Koll, 2012: Clouds and Snowball Earth deglaciation. *Geophysical Research Letters*, **39 (20)**.

Abbot, D. S., A. Voigt, and D. Koll, 2011: The Jormungand global climate state and implications for Neoproterozoic glaciations. *Journal of Geophysical Research: Atmospheres*, **116 (D18)**.

Abbot, D. S., A. Voigt, D. Li, G. L. Hir, R. T. Pierrehumbert, M. Branson, D. Pollard, and D. D. B. Koll, 2013: Robust elements of Snowball Earth atmospheric circulation and oases for life. *Journal of Geophysical Research: Atmospheres*, **118 (12)**, 6017–6027.

Allen, P. A. and P. F. Hoffman, 2005: Extreme winds and waves in the aftermath of a Neoproterozoic glaciation. *Nature*, **433 (7022)**, 123–127.

Angevine, W. M., H. Jiang, and T. Mauritsen, 2010: Performance of an eddy diffusivity–mass flux scheme for shallow cumulus boundary layers. *Monthly Weather Review*, **138 (7)**, 2895–2912.

Bagshaw, E. A., M. Tranter, A. G. Fountain, K. A. Welch, H. Basagic, and W. B. Lyons, 2007: Biogeochemical evolution of cryoconite holes on Canada glacier, Taylor Valley, Antarctica. *Journal of Geophysical Research: Biogeosciences*, **112 (G4)**.

Bao, H., I. J. Fairchild, P. M. Wynn, and C. Spötl, 2009: Stretching the envelope of past surface environments: Neoproterozoic glacial lakes from svalbard. *Science*, **323 (5910)**, 119–122.

Bechtold, P., M. Koehler, T. Jung, F. Doblas-Reyes, M. Leutbecher, M. J. Rodwell, F. Vitart, and G. Balsamo, 2008: Advances in simulating atmospheric variability with the ECMWF model: From synoptic to decadal time-scales. *Quarterly Journal of the Royal Meteorological Society*, **134 (634)**, 1337–1351.

Benn, D. I., G. Le Hir, H. Bao, Y. Donnadieu, C. Dumas, E. J. Fleming, M. J. Hambrey, E. A. McMillan, M. S. Petronis, G. Ramstein, et al., 2015: Orbitally forced ice sheet fluctuations during the marinoan snowball earth glaciation. *Nature Geoscience*, **8 (9)**, 704–707.

Berner, R. A., 2004: *The Phanerozoic carbon cycle: CO2 and O2*. Oxford University Press on Demand.

Bitz, C. M. and W. H. Lipscomb, 1999: An energy-conserving thermodynamic model of sea ice. *Journal of Geophysical Research: Oceans*, **104 (C7)**, 15 669–15 677.

Blamey, N. J., U. Brand, J. Parnell, N. Spear, C. Lécuyer, K. Benison, F. Meng, and P. Ni, 2016: Paradigm shift in determining Neoproterozoic atmospheric oxygen. *Geology*, **44 (8)**, 651–654.

Bonneville, S., F. Delpomdor, A. Préat, C. Chevalier, T. Araki, M. Kazemian, A. Steele, A. Schreiber, R. Wirth, and L. G. Benning, 2020: Molecular identification of fungi microfossils in a Neoproterozoic shale rock. *Science advances*, **6 (4)**.

Bosak, T., D. J. Lahr, S. B. Pruss, F. A. Macdonald, A. J. Gooday, L. Dalton, and E. D. Matys, 2012: Possible early foraminiferans in post-Sturtian (716- 635 Ma) cap carbonates. *Geology*, **40 (1)**, 67–70.

Boucher, O., D. Randall, P. Artaxo, C. Bretherton, G. Feingold, P. Forster, V.-M. Kerminen, Y. Kondo, H. Liao, U. Lohmann, et al., 2013: Clouds and aerosols. *Climate change 2013: the physical science basis. Contribution of Working Group I to the Fifth Assessment Report of the Intergovernmental Panel on Climate Change*, Cambridge University Press, 571–657.

Brandt, R. E., S. G. Warren, A. P. Worby, and T. C. Grenfell, 2005: Surface Albedo of the Antarctic Sea Ice Zone. *Journal of Climate*, **18 (17)**, 3606–3622.

Braun, C., J. Hörner, A. Voigt, and J. G. Pinto, 2022a: Ice-free tropical waterbelt during Snowball Earth events questioned by uncertain clouds. *Nature Geoscience*, **15**, 489–493, https://doi.org/10.1038/s41561-022-00950-1.

Braun, C., A. Voigt, C. Hoose, A. M. L. Ekman, and J. G. Pinto, 2022b: Controls on subtropical cloud reflectivity during a waterbelt scenario for the Cryogenian glaciations. *Journal of Climate*, https://doi.org/10.1175/JCLI-D-22-0241.1.

Briegleb, B., E. Hunke, C. Bitz, et al., 2002: The sea ice simulation of the Community Climate Model, Version two. Tech. rep., NCAR Tech. Note NCAR/TN2455+ STR.

Brocks, J. J., A. J. Jarrett, E. Sirantoine, C. Hallmann, Y. Hoshino, and T. Liyanage, 2017: The rise of algae in Cryogenian oceans and the emergence of animals. *Nature*, **548 (7669)**, 578–581.

Budyko, M. I., 1969: The effect of solar radiation variations on the climate of the Earth. *Tellus*, **21 (5)**, 611–619.

Calver, C., J. Crowley, M. Wingate, D. Evans, T. Raub, and M. Schmitz, 2013: Globally synchronous Marinoan deglaciation indicated by U-Pb geochronology of the Cottons Breccia, Tasmania, Australia. *Geology*, **41 (10)**, 1127–1130.

Campbell, A. J., E. D. Waddington, and S. G. Warren, 2011: Refugium for surface life on Snowball Earth in a nearly-enclosed sea? A first simple model for sea-glacier invasion. *Geophysical Research Letters*, **38 (19)**.

———, 2014: Refugium for surface life on Snowball Earth in a nearly enclosed sea? A numerical solution for sea-glacier invasion through a narrow strait. *Journal of Geophysical Research: Oceans*, **119 (4)**, 2679–2690.

Carns, R. C., B. Light, and S. G. Warren, 2016: The spectral albedo of sea ice and salt crusts on the tropical ocean of Snowball Earth: II. Optical modeling. *Journal of Geophysical Research: Oceans*, **121 (7)**, 5217–5230.

Chandler, M. A. and L. E. Sohl, 2000: Climate forcings and the initiation of low-latitude ice sheets during the Neoproterozoic Varanger glacial interval. *Journal of Geophysical Research: Atmospheres*, **105 (D16)**, 20 737–20 756.

Christner, B. C., B. H. Kvitko, and J. N. Reeve, 2003: Molecular identification of bacteria and eukarya inhabiting an Antarctic cryoconite hole. *Extremophiles*, **7 (3)**, 177–183.

Cloud, P., L. Wright, E. Williams, P. Diehl, and M. Walter, 1974: Giant stromatolites and associated vertical tubes from the Upper Proterozoic Noonday Dolomite, Death Valley region, eastern California. *Geological Society of America Bulletin*, **85 (12)**, 1869–1882.

Coakley, J. A., R. D. Cess, and F. B. Yurevich, 1983: The Effect of Tropospheric Aerosols on the Earth's Radiation Budget: A Parameterization for Climate Models. *Journal of Atmospheric Sciences*, **40 (1)**, 116 – 138.

Codron, F., 2012: Ekman heat transport for slab oceans. *Climate Dynamics*, **38 (1)**, 379–389.

Collins, W. D., 2001: Parameterization of generalized cloud overlap for radiative calculations in general circulation models. *Journal of the atmospheric sciences*, **58 (21)**, 3224–3242.

Collins, W. D., P. J. Rasch, B. A. Boville, J. J. Hack, J. R. McCaa, D. L. Williamson, J. T. Kiehl, B. Briegleb, C. Bitz, S.-J. Lin, et al., 2004: Description of the NCAR community atmosphere model (CAM 3.0). *NCAR Tech. Note NCAR/TN-464+ STR*, **226**.

Corsetti, F. A., A. N. Olcott, and C. Bakermans, 2006: The biotic response to Neoproterozoic snowball Earth. *Palaeogeography, Palaeoclimatology, Palaeoecology*, **232 (2-4)**, 114–130.

Dadic, R., P. C. Mullen, M. Schneebeli, R. E. Brandt, and S. G. Warren, 2013: Effects of bubbles, cracks, and volcanic tephra on the spectral albedo of bare ice near the Transantarctic Mountains: Implications for sea glaciers on Snowball Earth. *Journal of Geophysical Research: Earth Surface*, **118 (3)**, 1658–1676.

Darwin, C., 2004: *On the origin of species, 1859*. Routledge.

de Rooy, W. C., P. Bechtold, K. Fröhlich, C. Hohenegger, H. Jonker, D. Mironov, A. Pier Siebesma, J. Teixeira, and J.-I. Yano, 2013: Entrainment and detrainment in cumulus convection: an overview. *Quarterly Journal of the Royal Meteorological Society*, **139 (670)**, 1–19.

Dipankar, A., B. Stevens, R. Heinze, C. Moseley, G. Zängl, M. Giorgetta, and S. Brdar, 2015: Large eddy simulation using the general circulation model ICON. *Journal of Advances in Modeling Earth Systems*, **7 (3)**, 963–986.

Dohrmann, M. and G. Wörheide, 2017: Dating early animal evolution using phylogenomic data. *Scientific reports*, **7 (1)**, 1–6.

Donnadieu, Y., Y. Goddéris, G. Ramstein, A. Nédélec, and J. Meert, 2004a: A 'snowball Earth'climate triggered by continental break-up through changes in runoff. *Nature*, **428 (6980)**, 303–306.

Donnadieu, Y., G. Ramstein, F. Fluteau, D. Roche, and A. Ganopolski, 2004b: The impact of atmospheric and oceanic heat transports on the sea-ice-albedo instability during the Neoproterozoic. *Climate Dynamics*, **22 (2-3)**, 293–306.

Donohoe, A. and D. S. Battisti, 2012: What determines meridional heat transport in climate models? *Journal of climate*, **25 (11)**, 3832–3850.

Drugé, T., P. Nabat, M. Mallet, and S. Somot, 2021: Future evolution of aerosols and implications for climate change in the Euro-Mediterranean region using the CNRM-ALADIN63 regional climate model. *Atmospheric Chemistry and Physics*, **21 (10)**, 7639–7669.

Ern, M., P. Preusse, and C. Warner, 2006: Some experimental constraints for spectral parameters used in the Warner and McIntyre gravity wave parameterization scheme. *Atmospheric chemistry and physics*, **6 (12)**, 4361–4381.

Erwin, D. H., M. Laflamme, S. M. Tweedt, E. A. Sperling, D. Pisani, and K. J. Peterson, 2011: The Cambrian conundrum: early divergence and later ecological success in the early history of animals. *science*, **334 (6059)**, 1091–1097.

Evans, D. A., 2000: tratigraphic, geochronological, and paleomagnetic constraints upon the Neoproterozoic climatic paradox. *American Journal of Science*, **300 (5)**, 347–433.

Eyles, N. and N. Januszczak, 2004: 'Zipper-rift': a tectonic model for Neoproterozoic glaciations during the breakup of Rodinia after 750 Ma. *Earth-Science Reviews*, **65 (1-2)**, 1–73.

Fabre, S. and G. Berger, 2012: How tillite weathering during the snowball Earth aftermath induced cap carbonate deposition. *Geology*, **40 (11)**, 1027–1030.

Fairchild, I. J. and M. J. Kennedy, 2007: Neoproterozoic glaciation in the Earth System. *Journal of the Geological Society*, **164 (5)**, 895–921.

Fell, P. E., P.-A. Knight, and W. Rieders, 1989: Low-salinity tolerance of and salinity-induced dormancy in the estuarine sponge Microciona prolifera (Ellis et Solander) under long-term laboratory culture. *Journal of experimental marine biology and ecology*, **133 (3)**, 195–211.

Feulner, G., C. Hallmann, and H. Kienert, 2015: Snowball cooling after algal rise. *Nature Geoscience*, **8 (9)**, 659–662.

Field, P. R., R. P. Lawson, P. R. Brown, G. Lloyd, C. Westbrook, D. Moisseev, A. Miltenberger, A. Nenes, A. Blyth, T. Choularton, et al., 2017: Secondary ice production: Current state of the science and recommendations for the future. *Meteorological Monographs*, **58**, 7–1.

Fiorella, R. P. and C. J. Poulsen, 2013: Dehumidification over tropical continents reduces climate sensitivity and inhibits snowball Earth initiation. *Journal of Climate*, **26 (23)**, 9677–9695.

Font, E., A. Nédélec, R. Trindade, and C. Moreau, 2010: Fast or slow melting of the Marinoan snowball Earth? The cap dolostone record. *Palaeogeography, Palaeoclimatology, Palaeoecology*, **295 (1-2)**, 215–225.

Fountain, A. G., T. H. Nylen, M. Tranter, and E. Bagshaw, 2008: Temporal variations in physical and chemical features of cryoconite holes on Canada Glacier, McMurdo Dry Valleys, Antarctica. *Journal of Geophysical Research: Biogeosciences*, **113 (G1)**.

Fujino, K., E. L. Lewis, and R. G. Perkin, 1974: The freezing point of seawater at pressures up to 100 bars. *Journal of Geophysical Research (1896-1977)*, **79 (12)**, 1792–1797.

Gassmann, A. and H.-J. Herzog, 2008: Towards a consistent numerical compressible non-hydrostatic model using generalized hamiltonian tools. *Quarterly Journal of the Royal Meteorological Society*, **134 (635)**, 1597–1613.

Gerdel, R. and F. Drouet, 1960: The cryoconite of the Thule area, Greenland. *Transactions of the American Microscopical Society*, **79 (3)**, 256–272.

Gibson, T. M., P. M. Shih, V. M. Cumming, W. W. Fischer, P. W. Crockford, M. S. Hodgskiss, S. Wörndle, R. A. Creaser, R. H. Rainbird, T. M. Skulski, et al., 2018: Precise age of Bangiomorpha pubescens dates the origin of eukaryotic photosynthesis. *Geology*, **46 (2)**, 135–138.

Giorgetta, M. A., R. Brokopf, T. Crueger, M. Esch, S. Fiedler, J. Helmert, C. Hohenegger, L. Kornblueh, M. Köhler, E. Manzini, et al., 2018: ICON-A, the Atmosphere Component of the ICON Earth System Model: I. Model Description. *Journal of Advances in Modeling Earth Systems*, **10 (7)**, 1613–1637.

Giorgetta, M. A., E. Roeckner, T. Mauritsen, J. Bader, T. Crueger, M. Esch, S. Rast, L. Kornblueh, H. Schmidt, S. Kinne, et al., 2013: The atmospheric general circulation model ECHAM6-model description.

Giorgi, F., 2019: Thirty years of regional climate modeling: Where are we and where are we going next? *Journal of Geophysical Research: Atmospheres*, **124 (11)**, 5696–5723.

Glaze, L. S., S. Self, A. Schmidt, and S. J. Hunter, 2017: Assessing eruption column height in ancient flood basalt eruptions. *Earth and Planetary Science Letters*, **457**, 263–270.

Goddéris, Y., G. Le Hir, and Y. Donnadieu, 2011: Modelling the Snowball Earth. *Geological Society, London, Memoirs*, **36 (1)**, 151–161.

Goldblatt, C., V. L. McDonald, and K. E. McCusker, 2021: Earth's long-term climate stabilized by clouds. *Nature Geoscience*, **14 (3)**, 143–150.

Goodman, J. C. and R. T. Pierrehumbert, 2003: Glacial flow of floating marine ice in "Snowball Earth". *Journal of Geophysical Research: Oceans*, **108 (C10)**.

Goodman, J. C. and D. C. Strom, 2013: Feedbacks in a coupled ice-atmosphere-dust model of the glacial Neoproterozoic "Mudball Earth". *Journal of Geophysical Research: Atmospheres*, **118 (20)**, 11–546.

Gough, D., 1981: Solar interior structure and luminosity variations. *Physics of Solar Variations*, Springer, 21–34.

Hallett, J. and S. Mossop, 1974: Production of secondary ice particles during the riming process. *Nature*, **249 (5452)**, 26–28.

Hambrey, M. and W. Harland, 1985: The late Proterozoic glacial era. *Palaeogeography, Palaeoclimatology, Palaeoecology*, **51 (1-4)**, 255–272.

Hande, L., C. Engler, C. Hoose, and I. Tegen, 2015: Seasonal variability of Saharan desert dust and ice nucleating particles over Europe. *Atmospheric Chemistry and Physics*, **15 (8)**, 4389–4397.

Hansen, J., A. Lacis, D. Rind, G. Russell, P. Stone, I. Fung, R. Ruedy, and J. Lerner, 1984: Climate sensitivity: Analysis of feedback mechanisms. *feedback*, **1**, 1–3.

Harder, S. L., S. G. Warren, R. J. Charlson, and D. S. Covert, 1996: Filtering of air through snow as a mechanism for aerosol deposition to the Antarctic ice sheet. *Journal of Geophysical Research: Atmospheres*, **101 (D13)**, 18 729–18 743.

Harland, W. B., 1964: Evidence of Late Precambrian glaciation and its significance. *Problems in palaeoclimatology*, **705**, 119–149.

Harrison, S. P., P. Bartlein, K. Izumi, G. Li, J. Annan, J. Hargreaves, P. Braconnot, and M. Kageyama, 2015: Evaluation of CMIP5 palaeo-simulations to improve climate projections. *Nature Climate Change*, **5 (8)**, 735–743.

Hawkins, B. A., R. Field, H. V. Cornell, D. J. Currie, J.-F. Guégan, D. M. Kaufman, J. T. Kerr, G. G. Mittelbach, T. Oberdorff, E. M. O'Brien, et al., 2003: Energy, water, and broad-scale geographic patterns of species richness. *Ecology*, **84 (12)**, 3105–3117.

Heinze, R., A. Dipankar, C. C. Henken, C. Moseley, O. Sourdeval, S. Trömel, X. Xie, P. Adamidis, F. Ament, H. Baars, et al., 2017: Large-eddy simulations over Germany using ICON: A comprehensive evaluation. *Quarterly Journal of the Royal Meteorological Society*, **143 (702)**, 69–100.

Higgins, J. A. and D. P. Schrag, 2003: Aftermath of a snowball Earth. *Geochemistry, Geophysics, Geosystems*, **4 (3)**.

Hines, C. O., 1997: Doppler-spread parameterization of gravity-wave momentum deposition in the middle atmosphere. part 1: Basic formulation. *Journal of Atmospheric and Solar-Terrestrial Physics*, **59 (4)**, 371–386.

Hoffman, P. F., 2011a: A history of Neoproterozoic glacial geology, 1871–1997. *Geological Society, London, Memoirs*, **36 (1)**, 17–37.

———, 2011b: Strange bedfellows: glacial diamictite and cap carbonate from the Marinoan (635 Ma) glaciation in Namibia. *Sedimentology*, **58 (1)**, 57–119.

———, 2016: Cryoconite pans on Snowball Earth: supraglacial oases for Cryogenian eukaryotes? *Geobiology*, **14 (6)**, 531–542.

Hoffman, P. F., D. S. Abbot, Y. Ashkenazy, D. I. Benn, J. J. Brocks, P. A. Cohen, G. M. Cox, J. R. Creveling, Y. Donnadieu, D. H. Erwin, I. J. Fairchild, D. Ferreira, J. C. Goodman, G. P. Halverson, M. F. Jansen, G. Le Hir, G. D. Love, F. A. Macdonald, A. C. Maloof, C. A. Partin, G. Ramstein, B. E. J. Rose, C. V. Rose, P. M. Sadler, E. Tziperman, A. Voigt, and S. G. Warren, 2017: Snowball Earth climate dynamics and Cryogenian geology-geobiology. *Science Advances*, **3 (11)**.

Hoffman, P. F., A. J. Kaufman, G. P. Halverson, and D. P. Schrag, 1998: A Neoproterozoic snowball earth. *Science*, **281 (5381)**, 1342–1346.

Hoffman, P. F. and F. A. Macdonald, 2010: Sheet-crack cements and early regression in Marinoan (635 Ma) cap dolostones: regional benchmarks of vanishing ice-sheets? *Earth and Planetary Science Letters*, **300 (3-4)**, 374–384.

Hoffman, P. F. and D. P. Schrag, 2002: The snowball Earth hypothesis: testing the limits of global change. *Terra Nova*, **14 (3)**, 129–155.

Hoffmann, K.-H., D. Condon, S. Bowring, and J. Crowley, 2004: U-Pb zircon date from the Neoproterozoic Ghaub Formation, Namibia: constraints on Marinoan glaciation. *Geology*, **32 (9)**, 817–820.

Hogan, R. J. and A. J. Illingworth, 2000: Deriving cloud overlap statistics from radar. *Quarterly Journal of the Royal Meteorological Society*, **126 (569)**, 2903–2909.

Hohenegger, C., L. Kornblueh, D. Klocke, T. Becker, G. Cioni, J. F. Engels, U. Schulzweida, and B. Stevens, 2020: Climate Statistics in Global Simulations of the Atmosphere, from 80 to 2.5 km Grid Spacing. *Journal of the Meteorological Society of Japan. Ser. II.*

Holtslag, A. and B. Boville, 1993: Local versus nonlocal boundary-layer diffusion in a global climate model. *Journal of climate*, **6 (10)**, 1825–1842.

Hoose, C. and O. Möhler, 2012: Heterogeneous ice nucleation on atmospheric aerosols: a review of results from laboratory experiments. *Atmospheric Chemistry and Physics*, **12 (20)**, 9817–9854.

Hörner, J., A. Voigt, and C. Braun, 2022: Snowball Earth initiation and the thermodynamics of sea ice. *Journal of Advances in Modeling Earth Systems*. https://doi.org/10.1029/2021MS002734.

Hourdin, F., T. Mauritsen, A. Gettelman, J.-C. Golaz, V. Balaji, Q. Duan, D. Folini, D. Ji, D. Klocke, Y. Qian, et al., 2017: The art and science of climate model tuning. *Bulletin of the American Meteorological Society*, **98 (3)**, 589–602.

Hyde, W. T., T. J. Crowley, S. K. Baum, and W. R. Peltier, 2000: Neoproterozoic 'snowball Earth' simulations with a coupled climate/ice-sheet model. *Nature*, **405 (6785)**, 425–429.

Jacobson, M. Z., 2005: *Fundamentals of atmospheric modeling*. 2d ed., Cambridge Univ. Press, Cambridge [u.a.], literaturverz. S. 752 - 783.

James, N. P., G. M. Narbonne, and T. K. Kyser, 2001: Late Neoproterozoic cap carbonates: Mackenzie Mountains, northwestern Canada: precipitation and global glacial meltdown. *Canadian Journal of Earth Sciences*, **38 (8)**, 1229–1262.

Jiang, G., M. J. Kennedy, N. Christie-Blick, H. Wu, and S. Zhang, 2006: Stratigraphy, sedimentary structures, and textures of the late Neoproterozoic Doushantuo cap carbonate in South China. *Journal of Sedimentary Research*, **76 (7)**, 978–995.

Joseph, J. H., W. J. Wiscombe, and J. A. Weinman, 1976: The delta-eddington approximation for radiative flux transfer. *Journal of Atmospheric Sciences*, **33 (12)**, 2452 – 2459.

Jungclaus, J. H., S. Lorenz, H. Schmidt, O. Gutjahr, H. Haak, C. Mehlmann, U. Mikolajewicz, D. Notz, D. Putrasahan, J. S. von Storch, et al., 2021: The ICON Earth System Model Version 1.0. *Journal of Advances in Modeling Earth Systems*.

Kageyama, M., S. Albani, P. Braconnot, S. P. Harrison, P. O. Hopcroft, R. F. Ivanovic, F. Lambert, O. Marti, W. R. Peltier, J.-Y. Peterschmitt, et al., 2017: The PMIP4 contribution to CMIP6–Part 4: Scientific objectives and experimental design of the PMIP4-CMIP6 Last Glacial Maximum experiments and PMIP4 sensitivity experiments. *Geoscientific Model Development*, **10 (11)**, 4035–4055.

Kaltenegger, L., 2017: How to characterize habitable worlds and signs of life. *Annual Review of Astronomy and Astrophysics*, **55 (1)**, 433–485.

Kanji, Z. A., L. A. Ladino, H. Wex, Y. Boose, M. Burkert-Kohn, D. J. Cziczo, and M. Krämer, 2017: Overview of ice nucleating particles. *Meteorological Monographs*, **58**, 1.1–1.33.

Kärcher, B., J. Hendricks, and U. Lohmann, 2006: Physically based parameterization of cirrus cloud formation for use in global atmospheric models. *Journal of Geophysical Research: Atmospheres*, **111 (D1)**.

Kennedy, M. J., 1996: Stratigraphy, sedimentology, and isotopic geochemistry of Australian Neoproterozoic postglacial cap dolostones; deglaciation, delta 13 C excursions, and carbonate precipitation. *Journal of sedimentary Research*, **66 (6)**, 1050–1064.

Kilner, B., C. Niocaill, and M. Brasier, 2005: Low-latitude glaciation in the Neoproterozoic of Oman. *Geology*, **33 (5)**, 413–416.

Kirschvink, J. L., 1992: Late Proterozoic low-latitude global glaciation: the snowball Earth. *The Proterozoic Biosphere: A Multidisciplinary Study*, 51–52.

Klein, S. A., A. Hall, J. R. Norris, and R. Pincus, 2017: *Low-cloud feedbacks from cloud-controlling factors: A review*. Springer, 135–157 pp.

Klein, S. A. and D. L. Hartmann, 1993: The seasonal cycle of low stratiform clouds. *Journal of Climate*, **6 (8)**, 1587–1606.

Klemp, J., J. Dudhia, and A. Hassiotis, 2008: An upper gravity-wave absorbing layer for NWP applications. *Monthly Weather Review*, **136 (10)**, 3987–4004.

Knight, P.-A. and P. E. Fell, 1987: Low salinity induces reversible tissue regression in the estuarine sponge Microciona prolifera (Ellis & Solander). *Journal of Experimental Marine Biology and Ecology*, **107 (3)**, 253–261.

Knoll, A. H., 1992: The early evolution of eukaryotes: a geological perspective. *Science*, **256 (5057)**, 622–627.

Koeberl, C. and B. A. Ivanov, 2019: Asteroid impact effects on Snowball Earth. *Meteoritics & Planetary Science*, **54 (10)**, 2273–2285.

Körner, C., G. Farquhar, and Z. Roksandic, 1988: A global survey of carbon isotope discrimination in plants from high altitude. *Oecologia*, **74 (4)**, 623–632.

Korolev, A., G. McFarquhar, P. R. Field, C. Franklin, P. Lawson, Z. Wang, E. Williams, S. J. Abel, D. Axisa, S. Borrmann, et al., 2017: Mixed-phase clouds: Progress and challenges. *Meteorological Monographs*, **58**, 5.1–5.50.

Kristjánsson, J., J. Edwards, and D. Mitchell, 2000: Impact of a new scheme for optical properties of ice crystals on climates of two GCMs. *Journal of Geophysical Research: Atmospheres*, **105 (D8)**, 10 063–10 079.

Kulling, O., 1934: Scientific Results of the Swedish-Norwegian Arctic Expedition in the Summer of 1931. Part XI. *Geografiska Annaler*, **16**, 161–254.

Lan, Z., M. H. Huyskens, G. Le Hir, R. N. Mitchell, Q.-Z. Yin, G. Zhang, and X.-H. Li, 2022: Massive Volcanism May Have Foreshortened the Marinoan Snowball Earth. *Geophysical Research Letters*, **49 (6)**, e2021GL097 156, e2021GL097156 2021GL097156.

Le Hir, G., Y. Donnadieu, G. Krinner, and G. Ramstein, 2010: Toward the snowball Earth deglaciation…. *Climate dynamics*, **35 (2-3)**, 285–297.

Leamon, J. and P. E. Fell, 1990: Upper salinity tolerance of and salinity-induced tissue regression in the estuarine sponge Microciona prolifera. *Transactions of the American microscopical Society*, 265–272.

Lebo, Z. and H. Morrison, 2015: Effects of horizontal and vertical grid spacing on mixing in simulated squall lines and implications for convective strength and structure. *Monthly Weather Review*, **143 (11)**, 4355–4375.

Lee, L., K. Pringle, C. Reddington, G. Mann, P. Stier, D. Spracklen, J. Pierce, and K. Carslaw, 2013: The magnitude and causes of uncertainty in global model simulations of cloud condensation nuclei. *Atmospheric Chemistry and Physics*, **13 (17)**, 8879–8914.

Lenton, T. and A. Watson, 2013: *Revolutions that made the Earth*. OUP Oxford.

Li, D. and R. T. Pierrehumbert, 2011: Sea glacier flow and dust transport on Snowball Earth. *Geophysical Research Letters*, **38 (17)**.

Li, Z.-X., D. A. Evans, and G. P. Halverson, 2013: Neoproterozoic glaciations in a revised global palaeogeography from the breakup of Rodinia to the assembly of Gondwanaland. *Sedimentary Geology*, **294**, 219–232.

Liang, X.-Z., W.-C. Wang, and J. S. Boyle, 1997: *Atmospheric ozone climatology for use in general circulation models*. Lawrence Livermore National Laboratory.

Light, B., R. C. Carns, and S. G. Warren, 2016: The spectral albedo of sea ice and salt crusts on the tropical ocean of Snowball Earth: 1. Laboratory measurements. *Journal of Geophysical Research: Oceans*, **121 (7)**, 4966–4979.

Lilly, D. K., 1962: On the numerical simulation of buoyant convection. *Tellus*, **14 (2)**, 148–172.

Liu, P., Y. Liu, Y. Peng, J.-F. Lamarque, M. Wang, and Y. Hu, 2020: Large influence of dust on the Precambrian climate. *Nature Communications*, **11 (1)**, 1–8.

Liu, Y., P. Liu, D. Li, Y. Peng, and Y. Hu, 2021: Influence of Dust on the Initiation of Neoproterozoic Snowball Earth Events. *Journal of Climate*, **34 (16)**, 6673 – 6689.

Liu, Y., W. R. Peltier, J. Yang, and G. Vettoretti, 2013: The initiation of Neoproterozoic "snowball" climates in CCSM3: the influence of paleocontinental configuration. *Climate of the Past*, **9 (6)**, 2555–2577.

Liu, Y., W. R. Peltier, J. Yang, G. Vettoretti, and Y. Wang, 2017: Strong effects of tropical ice-sheet coverage and thickness on the hard snowball Earth bifurcation point. *Climate Dynamics*, **48 (11)**, 3459–3474.

Lohmann, U. and E. Roeckner, 1996: Design and performance of a new cloud microphysics scheme developed for the ECHAM general circulation model. *Climate Dynamics*, **12 (8)**, 557–572.

Louis, J.-F., 1979: A parametric model of vertical eddy fluxes in the atmosphere. *Boundary-Layer Meteorology*, **17 (2)**, 187–202.

Love, G. D., E. Grosjean, C. Stalvies, D. A. Fike, J. P. Grotzinger, A. S. Bradley, A. E. Kelly, M. Bhatia, W. Meredith, C. E. Snape, et al., 2009: Fossil steroids record the appearance of Demospongiae during the Cryogenian period. *Nature*, **457 (7230)**, 718–721.

Love, G. D. and R. E. Summons, 2015: The molecular record of Cryogenian sponges–a response to Antcliffe (2013). *Palaeontology*, **58 (6)**, 1131–1136.

Lovelock, J., 2016: *Gaia: A new look at life on earth*. Oxford University Press.

Lyons, T. W., C. W. Diamond, N. J. Planavsky, C. T. Reinhard, and C. Li, 2021: Oxygenation, Life, and the Planetary System during Earth's Middle History: An Overview. *Astrobiology*, **21 (8)**, 906–923, pMID: 34314605.

Macdonald, F. A., M. D. Schmitz, J. L. Crowley, C. F. Roots, D. S. Jones, A. C. Maloof, J. V. Strauss, P. A. Cohen, D. T. Johnston, and D. P. Schrag, 2010: Calibrating the cryogenian. *science*, **327 (5970)**, 1241–1243.

Macdonald, F. A. and R. Wordsworth, 2017: Initiation of Snowball Earth with volcanic sulfur aerosol emissions. *Geophysical Research Letters*, **44 (4)**, 1938–1946.

Madonna, E., H. Wernli, H. Joos, and O. Martius, 2014: Warm conveyor belts in the ERA-Interim dataset (1979–2010). Part I: Climatology and potential vorticity evolution. *Journal of Climate*, **27 (1)**, 3–26.

Maloof, A. C., C. V. Rose, R. Beach, B. M. Samuels, C. C. Calmet, D. H. Erwin, G. R. Poirier, N. Yao, and F. J. Simons, 2010: Possible animal-body fossils in pre-Marinoan limestones from South Australia. *Nature Geoscience*, **3 (9)**, 653–659.

Marshall, H. G., J. C. Walker, and W. R. Kuhn, 1988: Long-term climate change and the geochemical cycle of carbon. *Journal of Geophysical Research: Atmospheres*, **93 (D1)**, 791–801.

Mauritsen, T. and E. Roeckner, 2020: Tuning the MPI-ESM1. 2 Global Climate Model to Improve the Match With Instrumental Record Warming by Lowering Its Climate Sensitivity. *Journal of Advances in Modeling Earth Systems*, **12 (5)**, e2019MS002 037.

Mauritsen, T. and G. Svensson, 2007: Observations of stably stratified shear-driven atmospheric turbulence at low and high Richardson numbers. *Journal of the atmospheric sciences*, **64 (2)**, 645–655.

Mauritsen, T., G. Svensson, S. S. Zilitinkevich, I. Esau, L. Enger, and B. Grisogono, 2007: A total turbulent energy closure model for neutrally and stably stratified atmospheric boundary layers. *Journal of the Atmospheric Sciences*, **64 (11)**, 4113–4126.

McCoy, D. T., D. L. Hartmann, M. D. Zelinka, P. Ceppi, and D. P. Grosvenor, 2015: Mixed-phase cloud physics and Southern Ocean cloud feedback in climate models. *Journal of Geophysical Research: Atmospheres*, **120 (18)**, 9539–9554.

McCoy, D. T., I. Tan, D. L. Hartmann, M. D. Zelinka, and T. Storelvmo, 2016: On the relationships among cloud cover, mixed-phase partitioning, and planetary albedo in GCMs. *Journal of Advances in Modeling Earth Systems*, **8 (2)**, 650–668.

McGraw, Z., T. Storelvmo, R. O. David, and N. Sagoo, 2020: Global radiative impacts of mineral dust perturbations through stratiform clouds. *Journal of Geophysical Research: Atmospheres*, **125 (23)**.

Mengel, J., D. Short, and G. North, 1988: Seasonal snowline instability in an energy balance model. *Climate Dynamics*, **2 (3)**, 127–131.

Micheels, A. and M. Montenari, 2008: A snowball Earth versus a slushball Earth: Results from Neoproterozoic climate modeling sensitivity experiments. *Geosphere*, **4 (2)**, 401–410.

Mironov, D., B. Ritter, J.-P. Schulz, M. Buchhold, M. Lange, and E. MacHulskaya, 2012: Parameterisation of sea and lake ice in numerical weather prediction models of the German Weather Service. *Tellus A: Dynamic Meteorology and Oceanography*, **64 (1)**, 17 330.

Mlawer, E. J., S. J. Taubman, P. D. Brown, M. J. Iacono, and S. A. Clough, 1997: Radiative transfer for inhomogeneous atmospheres: RRTM, a validated correlated-k model for the longwave. *Journal of Geophysical Research: Atmospheres*, **102 (D14)**, 16 663–16 682.

Moczydłowska, M., 2008: The Ediacaran microbiota and the survival of Snowball Earth conditions. *Precambrian Research*, **167 (1-2)**, 1–15.

Molteni, F., 2003: Atmospheric simulations using a gcm with simplified physical parametrizations. i: Model climatology and variability in multi-decadal experiments. *Climate Dynamics*, **20 (2)**, 175–191.

Morris, J. L., M. N. Puttick, J. W. Clark, D. Edwards, P. Kenrick, S. Pressel, C. H. Wellman, Z. Yang, H. Schneider, and P. C. Donoghue, 2018: The timescale of early land plant evolution. *Proceedings of the National Academy of Sciences*, **115 (10)**, E2274–E2283.

Nelson, L. L., E. F. Smith, E. B. Hodgin, J. L. Crowley, M. D. Schmitz, and F. A. Macdonald, 2020: Geochronological constraints on Neoproterozoic rifting and onset of the Marinoan glaciation from the Kingston Peak Formation in Death Valley, California (USA). *Geology*, **48 (11)**, 1083–1087.

Noda, A. T., T. Seiki, W. Roh, M. Satoh, and T. Ohno, 2021: Improved representation of low-level mixed-phase clouds in a global cloud-system-resolving simulation. *Journal of Geophysical Research: Atmospheres*, **126 (17)**.

Nordeng, T. E., 1994: Extended versions of the convective parametrization scheme at ECMWF and their impact on the mean and transient activity of the model in the tropics. *Research Department Technical Memorandum*, **206**, 1–41.

Olcott, A. N., A. L. Sessions, F. A. Corsetti, A. J. Kaufman, and T. F. De Oliviera, 2005: Biomarker evidence for photosynthesis during Neoproterozoic glaciation. *Science*, **310 (5747)**, 471–474.

Orr, A., P. Bechtold, J. Scinocca, M. Ern, and M. Janiskova, 2010: Improved middle atmosphere climate and forecasts in the ECMWF model through a nonorographic gravity wave drag parameterization. *Journal of climate*, **23 (22)**, 5905–5926.

Peltier, W. R., Y. Liu, and J. W. Crowley, 2007: Snowball Earth prevention by dissolved organic carbon remineralization. *Nature*, **450 (7171)**, 813–818.

Peryt, T., A. Hoppe, T. Bechstädt, J. Köster, C. Pierre, and D. Richter, 1990: Late Proterozoic aragonitic cement crusts, Bambui Group, Minas Gerais, Brazil. *Sedimentology*, **37 (2)**, 279–286.

Phillips, V. T., P. J. DeMott, and C. Andronache, 2008: An empirical parameterization of heterogeneous ice nucleation for multiple chemical species of aerosol. *Journal of the Atmospheric Sciences*, **65 (9)**, 2757–2783.

Pierrehumbert, R., D. Abbot, A. Voigt, and D. Koll, 2011: Climate of the Neoproterozoic. *Annual Review of Earth and Planetary Sciences*, **39 (1)**, 417–460.

Pierrehumbert, R. T., 2002: The hydrologic cycle in deep-time climate problems. *Nature*, **419 (6903)**, 191–198.

———, 2004: High levels of atmospheric carbon dioxide necessary for the termination of global glaciation. *Nature*, **429 (6992)**, 646–649.

———, 2005: Climate dynamics of a hard snowball Earth. *Journal of Geophysical Research: Atmospheres*, **110 (D1)**.

Pincus, R., H. W. Barker, and J.-J. Morcrette, 2003: A fast, flexible, approximate technique for computing radiative transfer in inhomogeneous cloud fields. *Journal of Geophysical Research: Atmospheres*, **108 (D13)**.

Pincus, R. and B. Stevens, 2013: Paths to accuracy for radiation parameterizations in atmospheric models. *Journal of Advances in Modeling Earth Systems*, **5 (2)**, 225–233.

Pollard, D., J. F. Kasting, and M. E. Zugger, 2017: Snowball Earth: Asynchronous coupling of sea-glacier flow with a global climate model. *Journal of Geophysical Research: Atmospheres*, **122 (10)**, 5157–5171.

Porter, S. M., 2006: The Proterozoic fossil record of heterotrophic eukaryotes. *Neoproterozoic geobiology and paleobiology*, Springer, 1–21.

Poulsen, C. J. and R. L. Jacob, 2004: Factors that inhibit snowball Earth simulation. *Paleoceanography*, **19 (4)**.

Poulsen, C. J., R. T. Pierrehumbert, and R. L. Jacob, 2001: Impact of ocean dynamics on the simulation of the neoproterozoic "snowball Earth". *Geophysical Research Letters*, **28 (8)**, 1575–1578.

Powell, D., T. Louden, L. Kreidberg, X. Zhang, P. Gao, and V. Parmentier, 2019: Transit signatures of inhomogeneous clouds on hot Jupiters: Insights from microphysical cloud modeling. *The Astrophysical Journal*, **887 (2)**, 170.

Prill, F., D. Reinert, D. Rieger, and G. Zängl, 2020: Working with the ICON Model. Tech. rep., Deutscher Wetterdienst.

Ramanathan, V. and P. Downey, 1986: A nonisothermal emissivity and absorptivity formulation for water vapor. *Journal of Geophysical Research: Atmospheres*, **91 (D8)**, 8649–8666.

Rasch, P. and J. Kristjánsson, 1998: A comparison of the CCM3 model climate using diagnosed and predicted condensate parameterizations. *Journal of Climate*, **11 (7)**, 1587–1614.

Raschendorfer, M., 2001: The new turbulence parameterization of LM. COSMO Newsletter 1, Consortium for Small-Scale Modelling, p. 89-97.

Raub, T. D., 2008: *Prolonged deglaciation of "Snowball Earth"*. Yale University.

Rauterkus, R. and C. Ansorge, 2020: Cloud-top entrainment in mixed-phase stratocumulus and its process-level representation in large-eddy simulation. *Journal of the Atmospheric Sciences*, **77 (12)**, 4109 – 4127.

Rodehacke, C. B., A. Voigt, F. Ziemen, and D. S. Abbot, 2013: An open ocean region in Neoproterozoic glaciations would have to be narrow to allow equatorial ice sheets. *Geophysical Research Letters*, **40 (20)**, 5503–5507.

Roeckner, E., G. Bäuml, L. Bonaventura, R. Brokopf, M. Esch, M. Giorgetta, S. Hagemann, I. Kirchner, L. Kornblueh, E. Manzini, et al., 2003: The atmospheric general circulation model ECHAM 5. PART I: Model description.

Rooney, A. D., F. A. Macdonald, J. V. Strauss, F. Ö. Dudás, C. Hallmann, and D. Selby, 2014: Re-Os geochronology and coupled Os-Sr isotope constraints on the Sturtian snowball Earth. *Proceedings of the National Academy of Sciences*, **111 (1)**, 51–56.

Rose, B. E. J., 2015: Stable "Waterbelt" climates controlled by tropical ocean heat transport: A nonlinear coupled climate mechanism of relevance to Snowball Earth. *Journal of Geophysical Research: Atmospheres*, **120 (4)**, 1404–1423.

Rossow, W. B., A. Henderson-Sellers, and S. K. Weinreich, 1982: Cloud feedback: A stabilizing effect for the early Earth? *Science*, **217 (4566)**, 1245–1247.

Runnegar, B., 2000: Loophole for snowball Earth. *Nature*, **405 (6785)**, 403–404.

Sagoo, N. and T. Storelvmo, 2017: Testing the sensitivity of past climates to the indirect effects of dust. *Geophysical Research Letters*, **44 (11)**, 5807–5817.

Sakradzija, M., A. Seifert, and A. Dipankar, 2016: A stochastic scale-aware parameterization of shallow cumulus convection across the convective gray zone. *Journal of Advances in Modeling Earth Systems*, **8 (2)**, 786–812.

Schneider, T., 2006: The general circulation of the atmosphere. *Annual Review of Earth and Planetary Sciences*, **34 (1)**, 655–688.

Schwieterman, E. W., C. T. Reinhard, S. L. Olson, C. E. Harman, and T. W. Lyons, 2019: A limited habitable zone for complex life. *The Astrophysical Journal*, **878 (1)**, 19.

Segal, Y. and A. Khain, 2006: Dependence of droplet concentration on aerosol conditions in different cloud types: Application to droplet concentration parameterization of aerosol conditions. *Journal of Geophysical Research: Atmospheres*, **111 (D15)**.

Seifert, A. and K. D. Beheng, 2006: A two-moment cloud microphysics parameterization for mixed-phase clouds. Part 1: Model description. *Meteorology and Atmospheric Physics*, **92 (1-2)**, 45–66.

Seifert, A., C. Köhler, and K. Beheng, 2011: Aerosol-cloud-precipitation effects over Germany as simulated by a convective-scale numerical weather prediction model. *Atmospheric Chemistry and Physics*, **11 (20)**, 203–20.

Self, S., A. Schmidt, and T. Mather, 2014: Emplacement characteristics, time scales, and volcanic gas release rates of continental flood basalt eruptions on Earth. *Geological Society of America Special Papers*, **505**, 319–337.

Sellers, W. D., 1969: A global climatic model based on the energy balance of the earth-atmosphere system. *Journal of Applied Meteorology*, **8 (3)**, 392–400.

Semtner, A. J., 1976: A Model for the Thermodynamic Growth of Sea Ice in Numerical Investigations of Climate. *Journal of Physical Oceanography*, **6 (3)**, 379–389.

Senf, F., A. Voigt, N. Clerbaux, A. Hünerbein, and H. Deneke, 2020: Increasing Resolution and Resolving Convection Improve the Simulation of Cloud-Radiative Effects Over the North Atlantic. *Journal of Geophysical Research: Atmospheres*, **125 (19)**.

Sherwood, S. C., S. Bony, and J.-L. Dufresne, 2014: Spread in model climate sensitivity traced to atmospheric convective mixing. *Nature*, **505 (7481)**, 37–42.

Shields, A. L., V. S. Meadows, C. M. Bitz, R. T. Pierrehumbert, M. M. Joshi, and T. D. Robinson, 2013: The effect of host star spectral energy distribution and ice-albedo feedback on the climate of extrasolar planets. *Astrobiology*, **13 (8)**, 715–739.

Shields, G. A., 2005: Neoproterozoic cap carbonates: a critical appraisal of existing models and the plumeworld hypothesis. *Terra Nova*, **17 (4)**, 299–310.

Sledd, A. and T. L'Ecuyer, 2019: How Much Do Clouds Mask the Impacts of Arctic Sea Ice and Snow Cover Variations? Different Perspectives from Observations and Reanalyses. *Atmosphere*, **10 (1)**.

Slingo, J., 1987: The development and verification of a cloud prediction scheme for the ECMWF model. *Quarterly Journal of the Royal Meteorological Society*, **113 (477)**, 899–927.

Smagorinsky, J., 1963: General circulation experiments with the primitive equations: I. The basic experiment. *Monthly Weather Review*, **91 (3)**, 99–164.

Sommeria, G. and J. Deardorff, 1977: Subgrid-scale condensation in models of nonprecipitating clouds. *Journal of Atmospheric Sciences*, **34 (2)**, 344–355.

Sperling, E. A., J. M. Robinson, D. Pisani, and K. J. Peterson, 2010: Where's the glass? Biomarkers, molecular clocks, and microRNAs suggest a 200-Myr missing Precambrian fossil record of siliceous sponge spicules. *Geobiology*, **8 (1)**, 24–36.

Stevens, B., and co-authors, 2020: The Added Value of Large-Eddy and Storm-Resolving Models for Simulating Clouds and Precipitation. *Journal of the Meteorological Society of Japan. Ser. II.*

Stevens, B., S. Bony, and M. Webb, 2012: Clouds on-off klimate intercomparison experiment (COOKIE). Tech. rep.

Stevens, B. and G. Feingold, 2009: Untangling aerosol effects on clouds and precipitation in a buffered system. *Nature*, **461 (7264)**, 607–613.

Stevens, B., M. Giorgetta, M. Esch, T. Mauritsen, T. Crueger, S. Rast, M. Salzmann, H. Schmidt, J. Bader, K. Block, et al., 2013: Atmospheric component of the MPI-M Earth system model: ECHAM6. *Journal of Advances in Modeling Earth Systems*, **5 (2)**, 146–172.

Stevens, D. E., A. S. Ackerman, and C. S. Bretherton, 2002: Effects of domain size and numerical resolution on the simulation of shallow cumulus convection. *Journal of the Atmospheric Sciences*, **59 (23)**, 3285–3301.

Storelvmo, T. and I. Tan, 2015: The Wegener–Bergeron–Findeisen process—Its discovery and vital importance for weather and climate. *Meteorologische Zeitschrift*, **24**, 455–461.

Sundqvist, H., E. Berge, and J. E. Kristjánsson, 1989: Condensation and cloud parameterization studies with a mesoscale numerical weather prediction model. *Monthly Weather Review*, **117 (8)**, 1641–1657.

Thomas, D. and G. Dieckmann, 2002: Antarctic sea ice–a habitat for extremophiles. *Science*, **295 (5555)**, 641–644.

Tiedtke, M., 1989: A comprehensive mass flux scheme for cumulus parameterization in large-scale models. *Monthly Weather Review*, **117 (8)**, 1779–1800.

Trindade, R., E. Font, M. D'Agrella-Filho, A. Nogueira, and C. Riccomini, 2003: Low-latitude and multiple geomagnetic reversals in the Neoproterozoic Puga cap carbonate, Amazon craton. *Terra Nova*, **15 (6)**, 441–446.

Turbet, M., F. Forget, J. Leconte, B. Charnay, and G. Tobie, 2017: CO2 condensation is a serious limit to the deglaciation of Earth-like planets. *Earth and Planetary Science Letters*, **476**, 11–21.

Twomey, S., 1977: The influence of pollution on the shortwave albedo of clouds. *Journal of the Atmospheric Sciences*, **34 (7)**, 1149–1152.

Tziperman, E., D. S. Abbot, Y. Ashkenazy, H. Gildor, D. Pollard, C. G. Schoof, and D. P. Schrag, 2012: Continental constriction and oceanic ice-cover thickness in a Snowball-Earth scenario. *Journal of Geophysical Research: Oceans*, **117 (C5)**.

Vergara-Temprado, J., A. K. Miltenberger, K. Furtado, D. P. Grosvenor, B. J. Shipway, A. A. Hill, J. M. Wilkinson, P. R. Field, B. J. Murray, and K. S. Carslaw, 2018: Strong control of Southern Ocean cloud reflectivity by ice-nucleating particles. *Proceedings of the National Academy of Sciences*, **115 (11)**, 2687–2692.

Vincent, W., J. Gibson, R. Pienitz, V. Villeneuve, P. Broady, P. Hamilton, and C. Howard-Williams, 2000: Ice shelf microbial ecosystems in the high arctic and implications for life on snowball earth. *Naturwissenschaften*, **87 (3)**, 137–141.

Vincent, W. F., D. R. Mueller, and S. Bonilla, 2004: Ecosystems on ice: the microbial ecology of markham ice shelf in the high arctic. *Cryobiology*, **48 (2)**, 103–112.

Voigt, A., 2013: The dynamics of the Snowball Earth Hadley circulation for off-equatorial and seasonally varying insolation. *Earth System Dynamics*, **4 (2)**, 425–438.

Voigt, A., D. Abbot, R. Pierrehumbert, and J. Marotzke, 2011: Initiation of a Marinoan Snowball Earth in a state-of-the-art atmosphere-ocean general circulation model. *Climate of the Past*, **7**, 249–263.

Voigt, A. and D. S. Abbot, 2012: Sea-ice dynamics strongly promote Snowball Earth initiation and destabilize tropical sea-ice margins. *Climate of the Past*, **8**, 2079–2092.

Voigt, A., I. M. Held, and J. Marotzke, 2012: Hadley Cell Dynamics in a Virtually Dry Snowball Earth Atmosphere. *Journal of the Atmospheric Sciences*, **69 (1)**, 116–128.

Voigt, A. and J. Marotzke, 2010: The transition from the present-day climate to a modern Snowball Earth. *Climate Dynamics*, **35 (5)**, 887–905.

von Paris, P., F. Selsis, D. Kitzmann, and H. Rauer, 2013: The Dependence of the Ice-Albedo Feedback on Atmospheric Properties. *Astrobiology*, **13 (10)**, 899–909.

Waldbauer, J. R., L. S. Sherman, D. Y. Sumner, and R. E. Summons, 2009: Late Archean molecular fossils from the Transvaal Supergroup record the antiquity of microbial diversity and aerobiosis. *Precambrian Research*, **169 (1-4)**, 28–47.

Walker, J. C. G., P. B. Hays, and J. F. Kasting, 1981: A negative feedback mechanism for the long-term stabilization of Earth's surface temperature. *Journal of Geophysical Research: Oceans*, **86 (C10)**, 9776–9782.

Wallace, J. M. and P. V. Hobbs, 2006: *Atmospheric science : an introductory survey*. 2d ed., International geophysics series ; 92, Academic Press, Amsterdam, aa.

Walsh, A., T. Ball, and D. M. Schultz, 2019: Extreme sensitivity in Snowball Earth formation to mountains on PaleoProterozoic supercontinents. *Scientific reports*, **9 (1)**, 1–7.

Wan, H., M. A. Giorgetta, G. Zängl, M. Restelli, D. Majewski, L. Bonaventura, K. Fröhlich, D. Reinert, P. Ripodas, L. Kornblueh, et al., 2013: The ICON-1.2 hydrostatic atmospheric dynamical core on triangular grids–Part 1: Formulation and performance of the baseline version. *Geoscientific Model Development*, **6 (3)**, 735–763.

Warren, S. G., R. E. Brandt, T. C. Grenfell, and C. P. McKay, 2002: Snowball Earth: Ice thickness on the tropical ocean. *Journal of Geophysical Research: Oceans*, **107 (C10)**, 31.1–31.18.

Way, M. J., I. Aleinov, D. S. Amundsen, M. Chandler, T. Clune, A. D. Del Genio, Y. Fujii, M. Kelley, N. Y. Kiang, L. Sohl, et al., 2017: Resolving orbital and climate keys of earth and extraterrestrial environments with dynamics (rocke-3d) 1.0: a general circulation model for simulating the climates of rocky planets. *The Astrophysical Journal Supplement Series*, **231 (1)**, 12.

Weisman, M. L., W. C. Skamarock, and J. B. Klemp, 1997: The resolution dependence of explicitly modeled convective systems. *Monthly Weather Review*, **125 (4)**, 527–548.

Welch, B. L., 1947: The generalization of 'student's'problem when several different population variances are involved. *Biometrika*, **34 (1-2)**, 28–35.

Williams, G., 1975: Late Precambrian glacial climate and the Earth's obliquity. *Geological magazine*, **112 (5)**, 441–465.

Wilson, T. W., L. A. Ladino, P. A. Alpert, M. N. Breckels, I. M. Brooks, J. Browse, S. M. Burrows, K. S. Carslaw, J. A. Huffman, C. Judd, et al., 2015: A marine biogenic source of atmospheric ice-nucleating particles. *Nature*, **525 (7568)**, 234–238.

Winton, M., 2000: A reformulated three-layer sea ice model. *Journal of Atmospheric and Oceanic Technology*, **17 (4)**, 525–531.

Woelfle, M. D., C. S. Bretherton, and D. M. W. Frierson, 2015: Time scales of response to antisymmetric surface fluxes in an aquaplanet GCM. *Geophysical Research Letters*, **42 (7)**, 2555–2562.

Wolf, E. T., A. L. Shields, R. K. Kopparapu, J. Haqq-Misra, and O. B. Toon, 2017: Constraints on climate and habitability for earth-like exoplanets determined from a general circulation model. *The Astrophysical Journal*, **837 (2)**, 107.

Wood, R. and C. S. Bretherton, 2006: On the relationship between stratiform low cloud cover and lower-tropospheric stability. *Journal of Climate*, **19 (24)**, 6425–6432.

Wu, J., Y. Liu, and Z. Zhao, 2021: How Should Snowball Earth Deglaciation start. *Journal of Geophysical Research: Atmospheres*, **126 (2)**.

Xu, K.-M. and S. K. Krueger, 1991: Evaluation of cloudiness parameterizations using a cumulus ensemble model. *Monthly weather review*, **119 (2)**, 342–367.

Yang, J. and W. Peltier, 2012: The initiation of modern soft and hard Snowball Earth climates in CCSM4. *Climate of the Past Discussions*, **8 (1)**.

Yang, J., W. R. Peltier, and Y. Hu, 2012: The Initiation of Modern "Soft Snowball" and "Hard Snowball" Climates in CCSM3. Part I: The Influences of Solar Luminosity, CO2 Concentration, and the Sea Ice/Snow Albedo Parameterization. *Journal of Climate*, **25 (8)**, 2711–2736.

Zawierucha, K., M. Kolicka, N. Takeuchi, and Ł. Kaczmarek, 2015: What animals can live in cryoconite holes? A faunal review. *Journal of Zoology*, **295 (3)**, 159–169.

Zelinka, M. D., T. A. Myers, D. T. McCoy, S. Po-Chedley, P. M. Caldwell, P. Ceppi, S. A. Klein, and K. E. Taylor, 2020: Causes of Higher Climate Sensitivity in CMIP6 Models. *Geophysical Research Letters*, **47 (1)**.

Zender, C. S., H. Bian, and D. Newman, 2003: Mineral Dust Entrainment and Deposition (DEAD) model: Description and 1990s dust climatology. *Journal of Geophysical Research: Atmospheres*, **108 (D14)**.

Zhang, G. and N. A. McFarlane, 1995: Sensitivity of climate simulations to the parameterization of cumulus convection in the Canadian climate centre general circulation model. *Atmosphere-Ocean*, **33 (3)**, 407–446.

Zhang, M., W. Lin, C. S. Bretherton, J. J. Hack, and P. J. Rasch, 2003: A modified formulation of fractional stratiform condensation rate in the NCAR Community Atmospheric Model (CAM2). *Journal of Geophysical Research: Atmospheres*, **108 (D1)**, ACL–10.

Zumberge, J. A., G. D. Love, P. Cárdenas, E. A. Sperling, S. Gunasekera, M. Rohrssen, E. Grosjean, J. P. Grotzinger, and R. E. Summons, 2018: Demosponge steroid biomarker 26-methylstigmastane provides evidence for Neoproterozoic animals. *Nature ecology & evolution*, **2 (11)**, 1709–1714.

Zängl, G., D. Reinert, P. Rípodas, and M. Baldauf, 2015: The ICON (ICOsahedral Non-hydrostatic) modelling framework of DWD and MPI-M: Description of the non-hydrostatic dynamical core. *Quarterly Journal of the Royal Meteorological Society*, **141 (687)**, 563–579.

Acknowledgments / Danksagung

I decided to write parts of the acknowledgments in German, since for some of the points I feel that I will not be able to find appropriate expressions in English.

Meinen Dank möchte ich zunächst vor allem meinen Betreuern Aiko und Joaquim aussprechen. Eure Unterstützung in wissenschaftlicher aber vor allem auch in zwischenmenschlicher Hinsicht hat mich insbesondere in den schwierigen Zeiten durch diese Arbeit getragen. Danke für eure Geduld, euer Wohlwollen und den konstruktiven Umgang mit den Hürden, die wir im Laufe dieser Arbeit überwunden haben! Ihr habt mir damit ein Lernen weit über wissenschaftliche Qualifikationen und Inhalte hinaus ermöglicht.

On a scientific level, many people provided input and inspiration for this work. Thank you! I would like to particularly thank Annica, who also was a very welcoming host for me in Stockholm, and Corinna for introducing me to mixed-phase cloud microphysics. Furthermore, I would like to thank Johannes for joining us in understanding the Cryogenian climate. I enjoy(ed) working with you!

I thank the Deutsche Forschungsgemeinschaft (DFG) for funding this work under grant agreement VO 1765/5-1. Thanks at this point also to Aiko for acquiring the funding and offering this position to me! I would like to thank the German Climate Computing Center (DKRZ, Hamburg) for providing computing resources and technical support for this work through project 1092. Furthermore, I am grateful for all the work that the developers at MPI-M, DWD, DKRZ, and KIT invested to make the ICON model the flexible tool that it is today!

Regarding my transition from engineering to climate science I would like to particularly express my gratitude to Aiko and Bernhard who did not hesitate to just give it a try and dived into a master thesis with me. In this context I would also like to thank my ”new” fellow students at that time, Felix, Hanna, and Niklas, who made me feel very welcome at the institute. Thanks also to all my colleagues for contributing to the nice atmosphere at IMK-TRO! Particularly, I would like to thank all members of the former working group CONSTRAin. It was and is a pleasure to work and learn with you!

Danke an meine Freunde, Familie, Mitbewohner*innen und sonstige Begleiter*innen! Ihr habt mir immer wieder (geistig) erholsame und mit Freude gefüllte Pausen bereitet. Außerdem bedanke ich mich bei all den Menschen, die im Rahmen der SoLaWi KArotte, dem Klimakollektiv Karlsruhe, und Ende Gelände an einer lebenswerten Zukunft mitwirken. Unsere gemeinsamen Erlebnisse und Erfahrungen sind für mich persönlich in den letzten Jahren ein wertvoller Ausgleich zu meiner Arbeit gewesen. An dieser Stelle möchte ich mich auch ausdrücklich bei all denen bedanken, die mich darin bestärkt haben, dieses Projekt nun tatsächlich mit der Promotion abzuschließen. Insbesondere bei Katja und Markus, die in den besonders turbulenten Zeiten meiner Arbeit meinen Wunsch nach einer Revolution in sanfte Reformen gewandelt haben, und bei Tanja, die mir klar gemacht hat, dass es manchmal auch einfach notwendig ist, eine Auszeit zu nehmen.

Und zu guter letzt:
Danke an Katja, dass du mir beharrlich immer wieder klar machst, was ich kann, und mich dabei unterstützt, herauszufinden, wohin ich damit denn will! Danke an meine Eltern und meine Schwester, dass ihr bei all dem vielleicht manchmal etwas verwundert aber immer bedingungslos hinter mir steht! Ohne euren Rückhalt wäre diese Arbeit nicht entstanden.